

# Universal evaluation and design of imaging systems using information estimation

Henry Pinkard, Leyla Kabuli, Eric Markley, Tiffany Chien, Jiantao Jiao, and Laura Waller

Department of Electrical Engineering and Computer Sciences, University of California, Berkeley

Information theory, which describes the transmission of signals in the presence of noise, has enabled the development of reliable communication systems that underlie the modern world. Imaging systems can also be viewed as a form of communication, in which information about the object is “transmitted” through images. However, the application of information theory to imaging systems has been limited by the challenges of accounting for their physical constraints. Here, we introduce a framework that addresses these limitations by modeling the probabilistic relationship between objects and their measurements. Using this framework, we develop a method to estimate information using only a dataset of noisy measurements, without making any assumptions about the image formation process. We demonstrate that these estimates comprehensively quantify measurement quality across a diverse range of imaging systems and applications. Furthermore, we introduce Information-Driven Encoder Analysis Learning (IDEAL), a technique to optimize the design of imaging hardware for maximum information capture. This work provides novel insights into the fundamental performance limits of imaging systems and offers powerful new tools for their analysis and design.

## Introduction

Information theory [1] revolutionized communication systems, enabling digital data storage, cellular networks, satellite communication systems, and more. It did so by providing a mathematical framework that revealed the possibilities and limits of transmission of signals in the presence of noise. This laid the foundation for developing the practical tools and techniques for communication systems that underlie our modern world.

Information theory has long been recognized as a powerful tool for describing how imaging systems “transmit” information about the objects they image. In this framework, mutual information quantifies the ability to discriminate between objects based on noisy measurements.<sup>1</sup> This allows for the characterization of the fundamental performance limits of imaging systems in terms of the maximum mutual information they can capture (i.e. their channel capacity) [2, 3, 4, 5, 6, 7, 8]. However, despite the theoretical importance of this quantity, general-purpose design tools for imaging systems that parallel those available for communication systems have been surprisingly lacking [3]. The absence of such tools represents a

---

<sup>1</sup>A separate concept called Fisher information is sometimes used in imaging system design. Our use of the word “Information” throughout this manuscript refers to mutual information/entropy. We discuss connections between Fisher information and mutual information in **Section S5**

significant missed opportunity, as the ability to quantify information has substantial value in various contexts.

One such setting is when powerful algorithms are used to decode captured measurements. Deep neural networks [9], for example, excel at extracting subtle patterns from images. In the past, it was crucial for measurements to be encoded in a way that is human-interpretable or compatible with physics-based inverse problems, such as deconvolution. However, with the power of deep learning, the key factor for performance has shifted from *how* information is encoded to *how much* information is encoded, because neural networks can learn to decode information encoded in a variety of ways.

For example, computational imaging systems [10] employ nontraditional designs to capture measurements that combine various properties of light (e.g. angle, spectrum, polarization, coherence) in intricate ways. The resulting data may bear little resemblance to the original object or to conventional 2D intensity images [8, 11]. This complexity makes it difficult to define what constitutes a “good” measurement. The prevailing approach of assessing performance based on the final result (e.g. the reconstructed image) after the decoder step, means that performance is influenced by both the encoder and decoder quality. This makes it difficult to separate out the effects of each in order to design optimal encoders and make good use of the rapid progress in decoder technology.

Beyond computational imaging, quantifying information offers a more comprehensive understanding of traditional imaging systems. For instance, optical performance is typically characterized by resolution and field-of-view, which together determine the space-bandwidth product [12, 13, 14, 15]. The space-bandwidth product represents the number of resolvable spots within the field-of-view and the potential degrees-of-freedom of the system [16, 17, 18]. However, it does not take into account the critical role of measurement noise, which is usually quantified separately by the signal-to-noise ratio. Mutual information can encapsulate the effects of both space-bandwidth product and signal-to-noise ratio [19]. This enables assessment of their relative value and guides prioritization in system design and improvement.

Traditionally, information has been calculated as a function of the imaging system itself, similar to the channel capacity of a communication system [2, 3, 4, 5, 6, 7]. This approach overlooks a crucial difference: imaging systems have limited flexibility in encoding compared to communication systems. By not taking these limitations into account, the performance limits calculated in previous work provide overly optimistic estimates of imaging systems’ ability to capture information.

In communication, the sender has the freedom to choose how to map a message to an encoded signal before transmission. For instance, a computer can arbitrarily map English words to sequences of 0s and 1s before sending them over a network.

In contrast, imaging systems are subject to physical constraints that limit their encoding capabilities. For example, since there is limited or no flexibility to change the objects being imaged, optical imaging systems can only manipulate light that has interacted with them. Since conventional optics can only linearly transform electromagnetic radiation, they have limited ability to create highly distinguishable signals in the presence of noise.

To account for the constraints of imaging systems, it is necessary to model their object-dependent nature. Each bit of information enables perfect discrimination between two possible objects based on a noisy measurement. The ease of encoding this information varies

depending on the imaged objects, as some sets of objects inherently yield more distinct measurements. For example, capturing the bit of information needed to distinguish an image of a very bright object from an image of a very dim one is easier than distinguishing images of two objects similar in brightness.

In this work, we introduce a method for quantifying information that accounts for imaging system constraints through probabilistic modeling of objects, images, and measurements. Using this approach, we demonstrate that the difference between the theoretical unconstrained performance of an imaging system and its actual object-dependent performance can be an order-of-magnitude or more (**Fig. S4**). Consequently, modeling object-dependent performance provides a significantly more accurate and realistic quantification of information throughput.

In simple cases, objects can be modeled analytically, and information can be calculated directly. For complex, real-world imaging systems, we develop and demonstrate a practical method for data-driven information estimation. This method can be applied to a dataset of noisy measurements acquired from representative objects. A probabilistic model is fitted to these measurements, incorporating known or experimentally measured noise characteristics. Finally, the information content of the measurements is estimated through a straightforward computation using the fitted model. Since this approach abstracts away the specific physics of the encoding process, it can be readily applied to various types of imaging systems.

To demonstrate the value of our approach, we first analytically calculated mutual information for the classic problem of determining an imaging system’s resolution limit (**Sec. 1.1.1**). Here, information provides a more complete characterization of an imaging system’s capabilities than traditional optical resolution metrics alone. By incorporating both resolution and noise, it offers a probabilistic generalization that quantifies the fundamental limit of the ability to distinguish two points from one.

Next, we validated our information estimation framework’s practical utility and reliability through a series of experiments using simulated and real-world data. These experiments assessed the estimator’s accuracy, consistency, and robustness under various conditions and compared the tradeoffs between different probabilistic models in terms of accuracy, speed, and computational requirements.

Having demonstrated its effectiveness, we tested the ability of our information estimator to accurately quantify overall system performance in complex, practical settings. To this end, we conducted experiments on three imaging systems: label-free microscopy for single-cell phenotyping, lensless computational cameras, and single-shot computational 3D fluorescence microscopy using a 2D sensor. In each case, information estimates strongly predicted performance on downstream tasks, showing that information is a reliable, universally applicable metric for comprehensively quantifying performance across applications.

Building upon this idea, we introduce a framework called Information-Driven Encoder Assessment Learning (IDEAL), which leverages information as an efficient metric to iteratively optimize the design of the encoder. Like end-to-end design [20, 21, 22, 23, 24, 25, 26], which simultaneously optimizes the encoder and decoder for a specific task, IDEAL is particularly useful for designing complex encoders with unknown tradeoffs and design principles. However, unlike end-to-end design, it avoids the practical challenges of optimizing through decoders.

In summary, our work unlocks the use of information theory as a potent, practical tool for

analyzing, comparing, and enhancing imaging systems. It offers a comprehensive framework that goes beyond the specifics of individual imaging technologies, allowing for a deeper understanding of imaging system performance limits and offering practical design insights and methodologies for high-performance systems.

# 1 Results

## 1.1 Understanding encoded information

Quantifying information in imaging systems requires treating objects, images, and measurements probabilistically (**Fig. 1a**). A minimal model consists of three distributions: an **object**, which is mapped by an encoder (a deterministic function) to a noiseless **image**, which is then stochastically detected as a noisy **measurement** [2, 27, 28] (**Sec. S1**).<sup>2</sup>

Different encoders will map the object distribution to different noiseless image distributions, which may contain different amounts of object information. When the noiseless image is detected as a noisy measurement, additional information is lost due to random distortions caused by noise. Different encoders produce noiseless images that are more or less robust to this loss of information due to noise.

The mutual information between the object and the noisy measurement quantifies the amount of object information that survives both the encoding process and the subsequent corruption by noise (going forward, we will refer to this mutual information simply as “information”). By comparing the information content of measurements made using different encoders, we can evaluate their relative performance.

Mathematically, we represent an image with  $D$  pixels as a vector  $\mathbf{x} = (x_1, x_2, \dots, x_D)$ , where  $x_k$  is the energy (in photons) at the  $k$ th pixel. The probability distribution over images is then modeled as a joint distribution over these pixel values with probability density function  $p(\mathbf{x}) = p(x_1, x_2, \dots, x_D)$ . Similarly, the noisy measurement is represented as a vector  $\mathbf{y} = (y_1, y_2, \dots, y_D)$  with a probability density function  $p(\mathbf{y}) = p(y_1, y_2, \dots, y_D)$ .

It is not possible to directly visualize a  $D$ -dimensional probability distribution over images. Instead, we use two partial, complementary views (**Fig. 1b**). The **spatial coordinate** representation shows an individual image  $\mathbf{x} = (x_1, x_2, \dots, x_D)$  sampled from the distribution.

Alternatively, the **energy coordinate** representation (an extension of a concept in [19]) shows the probability mass over pixel values. In this representation, each image of  $D$  pixels is a  $D$ -dimensional vector, and the  $D$ -dimensional probability density function describes how likely each image is. Low-dimensional projections of the full distribution, such as the marginal distribution  $p(x_k)$  or the joint distribution  $p(x_k, x_j)$  of two pixels, provide insight into the full  $D$ -dimensional distribution’s behavior.

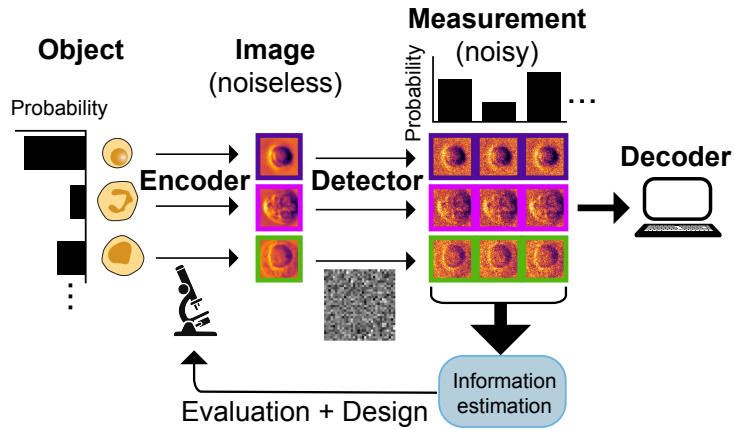
Thus, the spatial coordinate representation offers intuition about the spatial structure and correlations present in the images, while the energy coordinate representation reveals the statistical properties of pixel values and their dependencies. Together, these two perspectives offer complementary insights into the nature of image distributions and the flow of information.

---

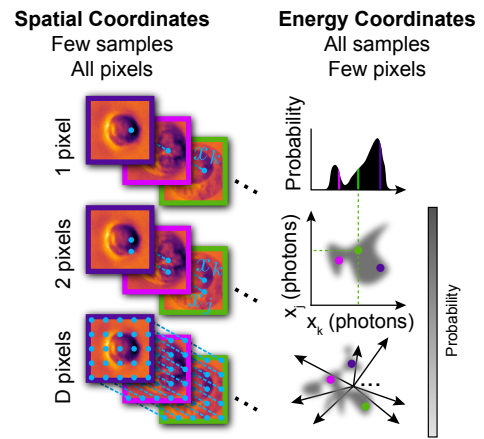
<sup>2</sup>This model is based on the widely used “semiclassical” theory of photodetection, which approximates the underlying quantum phenomena but yields accurate results in the vast majority of optical systems [28]

Visualizing the distribution of noisy measurements for a single clean image (i.e.  $p(\mathbf{y} | \mathbf{x})$ ) in energy coordinates demonstrates the effect of measurement noise (**Fig. 1c**): it spreads probability further from the point corresponding to the noiseless image. This increases the overlap between noisy distributions of different images, making it harder to determine the true object from a noisy measurement. The extent of this overlap determines how much object information is lost due to noise corruption.

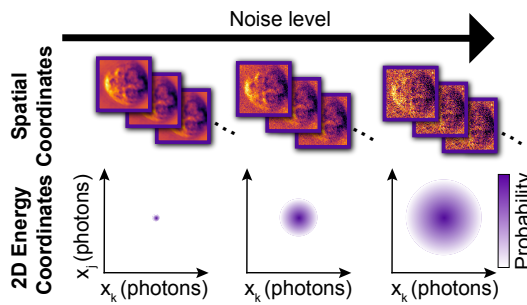
**a) Probabilistic model of imaging system**



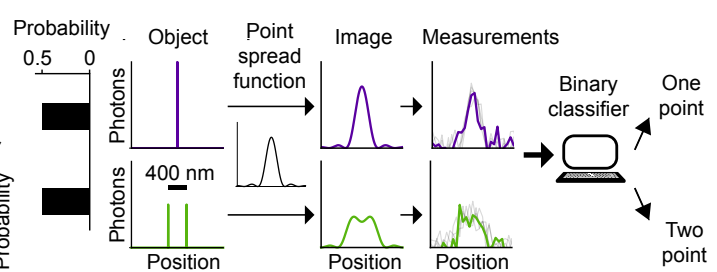
**b) Visualizing distributions**



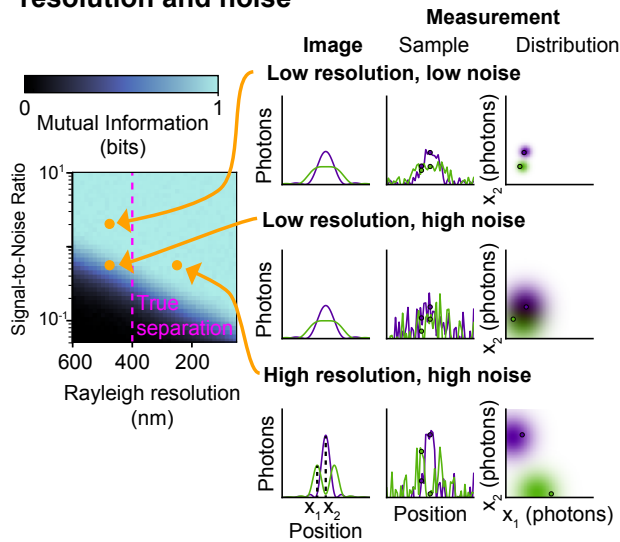
**c) Visualizing measurement noise**



**d) Probabilistic model of 2-point resolution**



**e) Information captures effects of resolution and noise**



**f) Dissimilar images are more robust to noise**

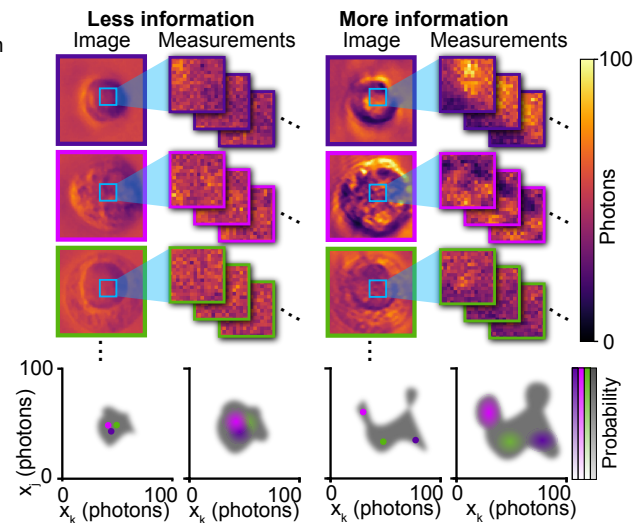


Figure 1: (Caption on next page)

Figure 1: **Information encoding in an imaging system.** **a)** Probabilistic model of an imaging system: a distribution of objects is encoded into images by an optical system and measured by a noisy detector, yielding a distribution of noisy measurements. These measurements can be used to estimate information content, guiding encoder design independently of decoding. **b)** Noisy image distributions can be visualized using complementary spatial and energy coordinate representations. In spatial coordinates, individual image samples are shown. In energy coordinates, each image is a point in a high-dimensional space, with the probability mass quantifying image likelihoods. Low-dimensional projections provide insight into the full distribution. **c)** In energy coordinates, the effect of measurement noise is to spread the probability mass of the noisy measurement away from the true noiseless image. **d)** Probabilistic two-point resolution model: an object (single point or two points with half energy) is convolved with a point spread function and corrupted by noise. Measurements are decoded by classifying if they came from one point or two points. **e)** Information analysis of two-point discrimination problem shows how information captures effects of both noise and resolution. (Left) Information as a function of signal-to-noise ratio and resolution, as determined by the Rayleigh criterion. (Right) Noiseless images, example noisy measurements, and energy coordinate views of measurement distribution illustrate how high resolution/high noise or low resolution/low noise contain equal information. **f)** Comparison of incoherent (left) and coherent (right) illumination encoders. Coherent illumination yields more distinct images and separable measurement distributions, while incoherent illumination produces more similar images and overlapping distributions.

### 1.1.1 Two-point resolution

To illustrate the information-theoretic view of imaging, we apply our framework to the classic two-point resolution problem, which quantifies an imaging system’s ability to distinguish between two closely spaced point objects. Classical two-point resolution criteria do not consider the effects of noise, which in practice can greatly affect the experimentally achievable resolution of a system. Information captures the effects of both resolution and noise, enabling a complete mathematical description of actual performance.

We use simplifying assumptions about the object, imaging system, and measurement noise in this illustrative example so that we can derive analytic expressions for the object information in the measurement as a function of resolution and signal-to-noise ratio, as well as the relationship between information and the accuracy of the optimal binary classifier. First, we assume a discrete object distribution with either a single point or two points (each with half the energy) occurring with probability  $\frac{1}{2}$ , in accordance with the interpretation of two-point resolution as the ability to distinguish between these scenarios [29, 30]. The object is imaged through a diffraction-limited point spread function and corrupted by additive Gaussian measurement noise (**Fig. 1d**).

The mutual information between the object  $\mathbf{O}$  and the noisy measurement  $\mathbf{Y}$ , denoted as  $I(\mathbf{O}; \mathbf{Y})$ , quantifies how much information is in  $\mathbf{Y}$  about  $\mathbf{O}$ . Since  $\mathbf{O}$  has two possibilities with equal probability, this binary choice can be made perfectly with 1 bit of information, providing an upper bound on  $I(\mathbf{O}; \mathbf{Y})$ . Assuming the optical system is deterministic, the

encoding process does not add uncertainty, so  $I(\mathbf{O}; \mathbf{Y}) = I(\mathbf{X}; \mathbf{Y})$ , allowing us to focus on the mutual information between the noiseless and noisy images.

To calculate  $I(\mathbf{X}; \mathbf{Y})$ , we decompose it into a difference of entropies:

$$I(\mathbf{X}; \mathbf{Y}) = H(\mathbf{Y}) - H(\mathbf{Y}|\mathbf{X}) \quad (1)$$

Here,  $H(\mathbf{Y})$  quantifies the randomness of the noisy measurement arising from both the random choice of object and the measurement noise, while  $H(\mathbf{Y}|\mathbf{X})$  is the randomness due to noise alone. For additive Gaussian noise,  $H(\mathbf{Y}|\mathbf{X})$  is a constant that can be calculated analytically as a function of the noise variance (**Sec. 18**). Since the probability density function of noisy measurements  $p(\mathbf{y})$  is known analytically in this case based on assumptions about the object, encoder and noise (**Sec. S1.3**),  $H(\mathbf{Y})$  can be estimated with arbitrarily high accuracy from samples of noisy measurements.

**Figure 1e** shows the measurement information content as a function of signal-to-noise ratio and optical resolution (as defined by the Rayleigh criterion [31]). This demonstrates how information directly quantifies the interplay of resolution and noise: equivalent information and decoding performance can be achieved with low-resolution, low-noise measurements or high-resolution, high-noise measurements, since the overlap of the measurement distributions remains the same.

**Extending to realistic scenarios** In real-world scenarios, object distributions are typically high-dimensional and have complex, unknown structures, unlike the simple discrete distribution in the two-point resolution problem. One way to interpret the two-point case is that better encoders create more distinct images that are more distinguishable in the presence of noise. On more complex objects/systems, this same goal can be achieved through various means, such as increasing optical resolution, improving signal-to-noise ratio, optimizing spectral sensitivity, adjusting sampling density, changing coherence properties of the illumination, etc. By strategically designing the imaging system to maximize the distinctiveness of the encoded images, one can enhance the information content of the measurements and ultimately improve the performance of downstream tasks.

**Figure 1f** illustrates this concept by comparing two microscope illumination patterns that differ in the spatial coherence of their illumination. The encoder on the left, which uses spatially incoherent illumination, maps different cells to lower-contrast, more similar images, resulting in noisy measurements that are difficult to distinguish from one another. In comparison, the encoder on the right, which uses spatially coherent illumination, creates higher-contrast, more distinct images, leading to noisy measurements that remain distinguishable. In the energy coordinate representation, more similar encoded images are closer together, resulting in overlapping and indistinguishable distributions of noisy measurements, while more distinct images have noisy measurement distributions that are still separable.

## 1.2 Estimating information

In practice, the true probability distributions of objects, images, and measurements are usually unknown, precluding the exact computation of information as in simplified models such

as two-point resolution (**Sec. 1.1.1**). However, in this section we demonstrate a practical, data-driven method to estimate the information content of measurements on complex, real-world scenarios.

Our approach estimates the object information in the measurement  $I(\mathbf{O}; \mathbf{Y})$  by instead estimating the mutual information between the noiseless image and noisy measurement  $I(\mathbf{X}; \mathbf{Y})$ . In an ideal imaging system, such as our two-point resolution example, these two quantities are equal. In real-world scenarios, this equivalence may not hold due to additional variations in images caused by uncontrolled additional sources of randomness. For example, images taken on a microscope may contain random effects from unpredictable movement of dust particles between exposures, or telescope imaging of a star may contain random distortions and variations arising from a fluctuating atmosphere. These variations introduce additional information into the measurements that is not related to the objects being imaged. To prevent overestimation of the true object information, the estimator can be calibrated by incorporating knowledge about relevant system state variables, effectively discounting the information arising from this system randomness (**Sec. S1.4.1**).

General-purpose information estimation methods often suffer from high bias and variance, computational complexity, and a lack of performance guarantees [32, 33, 34, 35, 36]. However, by leveraging the specific statistical structure of imaging systems, the estimation can be made much easier.

By decomposing mutual information to a difference of entropies (**Fig. 2a**),  $I(\mathbf{X}; \mathbf{Y}) = H(\mathbf{Y}) - H(\mathbf{Y}|\mathbf{X})$ , our estimator exploits a key property of imaging systems: the conditional independence of pixel values given the noiseless image, which allows for efficient computation of  $H(\mathbf{Y}|\mathbf{X})$ . This leaves just the problem of estimating  $H(\mathbf{Y})$ . We do this by fitting a parametric probabilistic model to the noisy measurement distribution, enabling the estimation of the  $H(\mathbf{Y})$  term using a tractable cross-entropy upper bound.

By taking advantage of these properties, our estimator can control its bias and variance based on the available data and computational resources, while also providing theoretical guarantees that lower estimates are less biased, enabling principled comparison of different estimates without knowledge of the true information value.

We begin by focusing on the conditional entropy term,  $H(\mathbf{Y} | \mathbf{X})$ , which is easier to estimate due to the common assumption of pixel-wise conditional independence given the noiseless image [28]. This simplifies a computationally intractable high-dimensional integration into a sum of one-dimensional integrals (**Sec. S2.3**). For commonly used noise models like Gaussian or signal-dependent shot noise, we can derive efficient closed-form estimators of this conditional entropy, which can be readily generalized to other analytic or empirical noise distributions (**Sec. S2.3**). Though the analytical expression for shot noise is a function of the noiseless pixel values, we found that it can be closely approximated using only noisy measurements, which importantly enables the estimator to be applied to noisy experimental data (**Fig. S15**).

Estimating the entropy of the noisy measurements,  $H(\mathbf{Y})$ , is more challenging because the true probability density function,  $p(\mathbf{y})$ , is unknown.

To address this, we fit a parametric probabilistic model,  $p_\theta(\mathbf{y})$ , to the data (**Sec. S2.4**). This enables us to estimate the cross-entropy, which upper bounds the true entropy (**Sec. S2.4**). As the model better fits the data, the bound becomes tighter, guaranteeing a less biased estimate, even though the true probability distributions are unknown. The complexity

and flexibility of the probabilistic model can be adjusted based on the available data and computational resources, allowing for a trade-off between the tightness of the bound and the complexity of the estimation procedure.

The cross-entropy estimation method is closely related to the theory of data compression [37]: a better-fitting model is compressing the data more effectively, and since data cannot be losslessly compressed beyond its inherent entropy, the cross-entropy provides an upper bound on the entropy of noisy measurements.

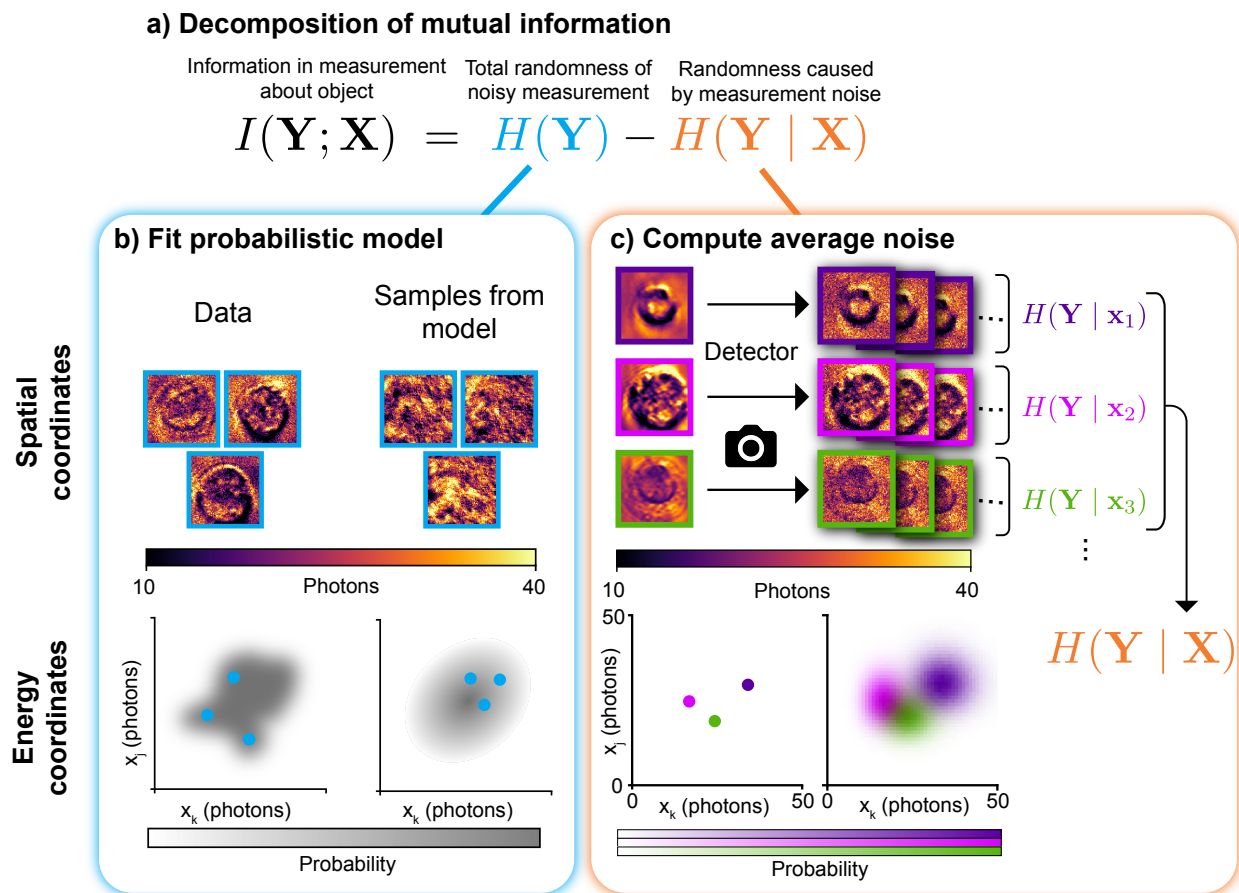


Figure 2: **Decomposition of mutual information as a difference of entropies.** **a)** The decomposition of mutual information into a marginal and conditional entropy used in our estimation procedure. **b)** The marginal entropy of the noisy measurements can be estimated by fitting a probabilistic model to the data and computing the expected value of the negative log-likelihood of held out test data. Left, samples from an energy coordinate view of the data distribution. Right, samples from a stationary Gaussian process model fit to the data distribution. **c)** The conditional entropy measures the average noise entropy across all measurements.

**Validating information estimation** We evaluated two probabilistic models in our information estimation framework: a computationally efficient stationary multivariate Gaussian

distribution and a more flexible but data-intensive deep neural network-based model called PixelCNN [38, 39, 40].

The choice of probabilistic model allows for a trade-off between computational efficiency and the tightness of the upper bound on the true information content. Simple models like stationary Gaussian processes provide fast estimates with minimal data requirements, while more complex models like PixelCNNs can yield tighter bounds at the cost of increased computational resources and data needs (**Figures S9, S10, S12, S13, S14**).

Since it is straightforward to compare the results of different models – the upper bound nature means the lowest estimate is most accurate – the best approach when using information estimation on new problems is to try a variety of models and see which performs best given the available resources.

### 1.3 Information predicts decoder performance

To validate the practical relevance of our information estimates, we investigate the relationship between estimated information content and the performance of various decoding tasks across different imaging systems and object types. Our experiments aim to establish information as a reliable metric for encoder quality and provide insights into the interpretation of information estimates in real-world scenarios. By demonstrating the predictive power of information content, we lay the foundation for its application in analyzing, comparing, and optimizing imaging systems.

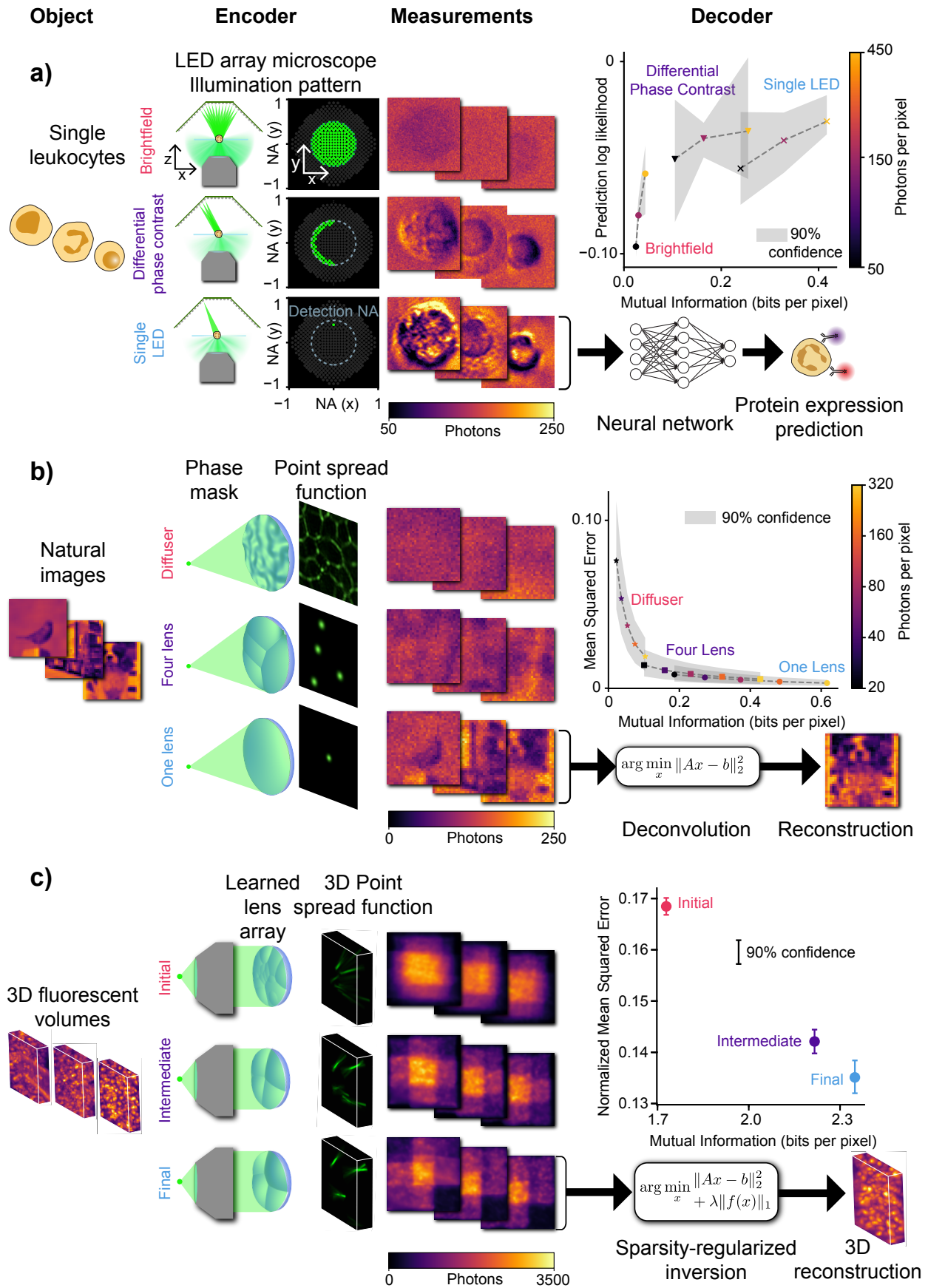


Figure 3: (Caption on next page)

Figure 3: **Measurement information content predicts decoding performance across various objects, imaging systems, and decoding tasks.** **a)** Protein expression prediction in single leukocytes encoded with different angular illumination patterns on an LED array microscope. **b)** Image deconvolution on natural images encoded with different lensless cameras. **c)** Single-shot 3D volume reconstruction on 3D fluorescent lung cells with different random lens arrays designed with end-to-end learning.

**LED array microscopy + single cell phenotyping** LED array microscopy [41, 42] is a versatile computational imaging technique that replaces the illumination lamp of a traditional transmitted light microscope with a programmable LED array. By illuminating with different patterns, it enables easy switching between various contrast generation mechanisms, including brightfield, darkfield, and differential phase contrast.

The Berkeley Single Cell Computational Microscopy dataset [43] contains images of  $\sim 400,000$  leukocytes, each imaged with multiple contrast modalities on an LED array microscope and fluorescently labeled for protein expression. We compared the estimated information content of measurements made with different illumination patterns to the performance of predicting the cells’ protein expression profiles (**Fig. 3a**). Synthetic noise was added to images of identical cells under Brightfield, Differential Phase Contrast, and Single LED illumination to simulate varying signal-to-noise ratios. We trained a convolutional neural network on each contrast modality to predict the expression of eight cell type-specific proteins, using the average log likelihood across proteins as an overall performance metric.

The illumination patterns exhibited significant variation in information content, and we found that measurements with more information indeed corresponded to better phenotyping performance. As expected, both estimated information and decoding performance increased with higher photon counts (i.e., higher signal-to-noise ratio).

This experiment demonstrates information estimation’s ability to quantify measurement quality across encoders with disparate physical operation. A key difference between the illumination patterns is spatial coherence: light from each LED is incoherent with other LEDs, so overall coherence depends on the number of active LEDs. Coherent, partially coherent, and incoherent light have distinct mathematical models for image formation [18, 44, 45]. Consequently, direct comparison of their resolution and contrast is challenging without additional assumptions [18, 44, 46]. However, information-based analysis abstracts away these differences, enabling direct comparison.

This example brings up an important point: The validity of approximating the object information  $I(\mathbf{O}; \mathbf{Y})$  with the image information  $I(\mathbf{X}; \mathbf{Y})$  depends on the degree of randomness in the image unrelated to noise or to the object itself. Spatially coherent illumination, such as that from a single LED, encodes more information per photon because it is more sensitive to small changes in the object structure. For the same reason, it can introduce more system-derived randomness due to dust or optical imperfections, leading to an overestimation of object information. However, calibration can account for this randomness and improve estimate accuracy (**Sec. S1.4.1**).

We tested the effects of this by estimating the information in blank images containing only contrast from optical imperfections (**Fig. S17**) to compare the magnitude of system

randomness and object randomness. While insignificant in this case compared to variations in object information, it illustrates the trade-off between maximizing captured information and minimizing calibration difficulty: some tasks require less information, and can therefore use systems that are easier to calibrate without sacrificing performance.

**Lensless imaging + image deconvolution** Next, we investigated the information encoding capabilities of lensless imagers (**Fig. 3b**). These compact computational cameras replace the traditional lens with a light-modulating mask near the sensor, enabling applications in photography, machine vision, fluorescence microscopy, and in-vivo imaging [47]. Lensless imagers offer a compact form factor, simple hardware, wide field of view, and the ability to encode additional dimensions such as depth, time, or wavelength in a single capture. Unlike traditional cameras, which map object points to sensor pixels one-to-one, lensless imagers capture multiplexed measurements where each object point maps to multiple pixels and vice versa. Consequently, their raw measurements require decoding through deconvolution to recover the object.

We compared three imagers with different phase masks: a single lens system, a random microlens array [48], and a Gaussian diffuser [49]. Simulated measurements of CIFAR10 natural images [50] at various signal-to-noise ratios were decoded using Wiener deconvolution with self-tuned regularization [51]. Plotting mutual information estimates against deconvolution performance (**Fig. 3b**) revealed a clear trend: higher information content corresponded to more accurate object reconstructions across signal-to-noise ratios and encoders, demonstrating that information quantitatively unifies the effects of noise and multiplexing on system performance.

Significantly, we did not see the same monotonic trend when evaluating accuracy of a 10-class object classification decoder (**Fig. S18**). This is likely a consequence of the  $100\times$  difference in total information in the measurements compared to information relevant to a simple classification task (**Sec. S4**). Thus, information may be less predictive of performance when only highly specific features of the images are relevant to decoding. In these cases, it may be more useful to focus on task-specific mutual information estimates (**Sec. S1.4.2**).

**End-to-end designed snapshot 3D microscopy** Finally, we applied information estimation to snapshot 3D fluorescence microscopy, which captures a single multiplexed 2D image at each time point and computationally reconstructs the 3D volume. This approach enables faster 3D imaging of dynamic processes compared to traditional methods that sequentially capture multiple focal planes. These systems extend the concept of multiplexed measurements from 2D lensless imaging, leading to a complex design space for the optimal 3D point spread function.

One promising approach places an array of microlenses in the microscope’s Fourier plane, creating a point spread function of small points that change focus over depth [52, 53]. While this design enables multiplexing without significantly degrading signal-to-noise, a theoretical understanding of the optimal microlens number and location is lacking and is hypothesized to depend on sample structure and signal-to-noise level, among other factors.

One way of designing 3D snapshot imagers is through end-to-end design [20, 21, 22, 23, 24, 25, 26], a data-driven technique for learning optimal system configurations in situations

with numerous tunable parameters and novel setups lacking established design principles. In this approach, a differentiable optical encoder model is combined with a differentiable decoder, creating a fully differentiable model of the entire computational imaging pipeline. By backpropagating the loss from a decoding task through the pipeline, both the hardware encoder and software decoder can be simultaneously optimized.

This data-driven method can discover specialized designs tailored to specific samples, surpassing the limitations of existing physical models and design intuitions. End-to-end design has proven successful across various imaging modalities, enabling the development of highly optimized systems for specific applications.

We hypothesized that end-to-end learned designs, though explicitly trained to reduce a loss function like mean squared error, also encode measurements with more information.

To test this, we performed end-to-end learning of microlens arrays, where lenses varied in their positions and focal lengths, on 3D fluorescently labelled lung tissue. The end-to-end design algorithm was initialized with many microlenses of varying focal lengths, and training converged to a few microlenses with focal lengths approximately uniformly distributed through the volume. Taking the lens arrays at the beginning, middle, and end of training, we estimated the information content of measurements and separately trained a sparsity-constrained inverse reconstruction algorithm (**Fig. 3c**).

The results show that the information content of the measurements did in fact increase as the learning progressed, even though data-driven end-to-end learning does not explicitly incorporate any notion of information. This result further validates information as a meaningful metric. In addition, just like the previous two systems, measurements with more information resulted in more accurate reconstructions of the 3D object.

## 1.4 Information Driven Encoder Analysis Learning (IDEAL).

Information content is not only a powerful tool for evaluating imaging systems – it can also be directly used to optimize their design. Inspired by the success of end-to-end design [20, 21, 22, 23, 24, 25, 26] in developing novel designs, we propose a new approach called Information Driven Encoder Analysis Learning (IDEAL).

Evaluating the microlens arrays for snapshot 3D microscopy showed that end-to-end design increases the information content of the measurements (**Fig. 3c**). Thus, we hypothesized that it might be possible to optimize the encoder based on information content alone, without the need for a decoder in the optimization loop.

Like end-to-end design, IDEAL uses differentiable encoder models, but instead of decoding measurements through an image reconstruction algorithm and backpropagating gradients through both the encoder and decoder, it estimates information directly from the measurements produced by the encoder and optimizes the physical parameters of the encoder with a negative mutual information loss function (**Fig. 4a**).

We tested IDEAL on the single-shot 3D fluorescence microscope [53] described previously (**Sec. 1.3**), using a loss function that estimates mutual information with a Gaussian model computed directly from the measurements. Optimizing this objective function increased the estimated information by positioning multiple microlenses to focus at different planes in the object (**Fig. 4b**), learning a similar design as the one learned from end-to-end design (**Fig. 3c**).

To confirm that the IDEAL optimization process improved measurement quality, we performed two analyses using the initial, intermediate, and final designs (**Fig. 4b, c**). First, we used a PixelCNN model, which is more accurate than the Gaussian approximation used in the IDEAL loss function, to get a more accurate estimate the information content. This analysis verified that the information increased over the course of optimization. Second, we trained image reconstruction decoders on measurements from each design. The average reconstruction error across decoders decreased as optimization progressed, demonstrating that IDEAL produces measurements better suited for decoding.

Surprisingly, the IDEAL-designed encoder outperformed the end-to-end optimized encoder in both information content (1.626 vs 1.491 bits/pixel) and reconstruction error (0.132 vs 0.135), even though end-to-end design explicitly optimizes reconstruction error. In addition, our IDEAL implementation converges 3-4 $\times$  faster than our end-to-end design implementation while using less GPU memory. We hypothesize that removing the complex decoder from the optimization improves the loss landscape, leading to better performance.

## Discussion

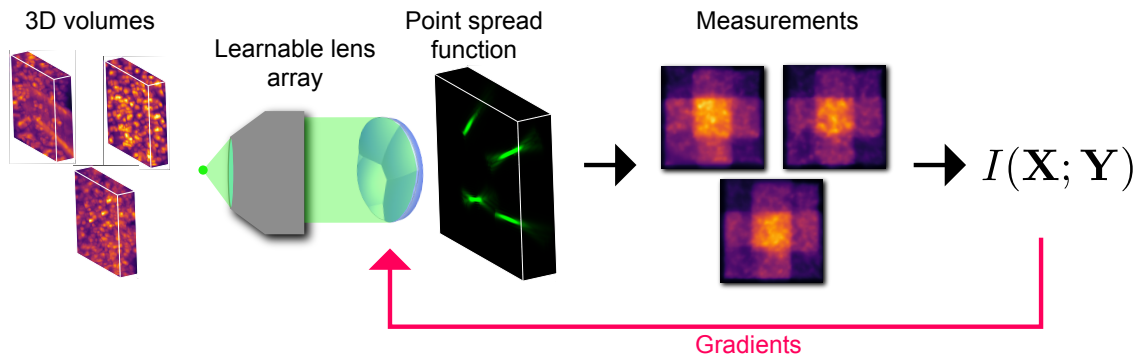
In this work, we have developed a framework that unlocks information theory as a potent, practical tool for designing and evaluating imaging systems. This opens the door to applying the same powerful principles that have transformed communication to advance imaging technology across a wide range of applications.

We expect this framework to have wide-reaching impacts on the ability to design imaging systems. We’ve demonstrated this potential on several nontraditional systems where human intuition of raw measurements is limited, and there is a lack of established engineering principles. Our approach also finds useful application in traditional systems where the interplay between different metrics is complex or powerful algorithms such as deep neural networks are employed to decode the measured data.

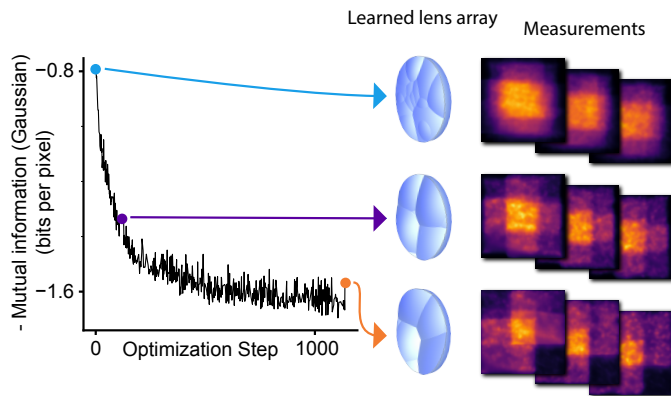
**Benefits of information-based design** Information-based design offers several benefits. First, it provides a comprehensive metric that unifies factors such as resolution and noise into a single quantity. Second, information is abstracted from the details of the image formation process allowing it to be applied to diverse imaging modalities despite their distinct physical operating principles. Third, information has a universal interpretation across all modalities—it quantifies how well objects can be discriminated based on noisy measurements. This enables direct comparisons between disparate imaging systems.

**Synergy with physics-based modeling** Though information’s universality and abstraction from the physics of image formation are powerful features, this does not diminish the value of physics-based modeling. In fact, incorporating physical modeling into information analyses of simulated systems enables a precise characterization of how particular design choices affect overall performance. This provides valuable insights for system optimization and can facilitate automated information-maximizing design, as demonstrated by our proposed technique: Information-Driven Encoder Analysis Learning (IDEAL).

**a) Information Driven Encoder Analysis Learning (IDEAL) on snapshot 3d microscopy**



**b) Training process**



**c) Training decreases decoder error and increases mutual information**

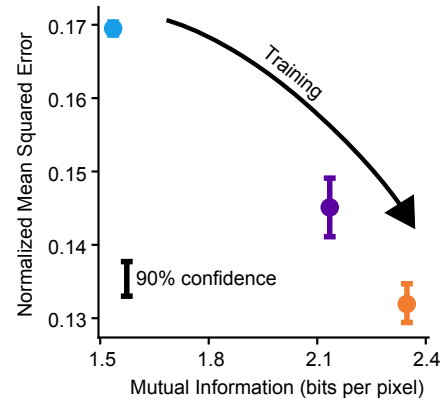


Figure 4: **Information Driven Encoder Analysis Learning (IDEAL) enables tuning of design parameters based on measurement information content.** **a)** Application of IDEAL to a single-shot 3D fluorescence microscope, optimizing microlens positions and focal lengths based on information content of measurements. **b)** The increase in measurement information content over the course of training and corresponding learned lens arrays. **c)** Reconstruction error of independently trained decoders on measurements with learned lens arrays vs high accuracy PixelCNN-based mutual information estimates confirm that IDEAL designs encode more information and achieve superior performance on downstream tasks.

**Benefits of IDEAL design** Decoder-independent evaluation also offers significant benefits when optimizing systems using Information-Driven Encoder Assessment Learning (IDEAL). This approach can dramatically reduce compute and memory requirements, freeing up resources for the optimization of larger and more complex systems. Moreover, it avoids the vanishing gradient problem, where gradients become extremely small as they propagate through deep neural networks, making it difficult to update the weights of earlier layers [54, 55]. In certain cases, specialized decoders are required to overcome this issue and correctly learn designs [26, 56]. Evaluating information on raw measurements sidesteps this challenge entirely.

**Objective comparisons between encoders** The need for comparing encoding mechanisms is increasingly important because powerful algorithms such as deep neural networks can perform the same downstream tasks using different types of measurements. For example, a common decoding task is to deconvolve raw measurements to obtain a more accurate image of the original object. When the same object is encoded on two imaging systems in different ways, the one that produces a deconvolved image more closely resembling the true object is considered to be of higher quality.

However, assessing the quality of the decoded image is inherently limited by the fact that even physics-based image processing algorithms, such as deconvolution, can introduce artifacts. More powerful algorithms, such as deep neural networks, can improve performance but may produce “hallucinations” that are even harder to detect because they appear visually plausible [57, 58]. As a result, subjective visual assessment or quantitative analysis of deconvolved images cannot be trusted as a reliable way to assess quality on their own. They must be compared with ground truth validation, which is often not available, especially in experimental settings.

Evaluating using information offers the best of both worlds. It provides a common basis for direct comparison, enabling the evaluation of different encoding mechanisms on a unified scale. In addition, information can be evaluated directly on the measurements, thereby avoiding the need for ground truth data, algorithmic artifacts, and subjective interpretation.

**General characteristics of good encoders** The ability to quantitatively evaluate the quality of encoders naturally raises the question: are there shared qualities among the best encoders that we should strive to incorporate in our designs? Information theory offers valuable guidance on the characteristics of ideal encoding schemes. The noisy channel coding theorem [1, 59, 37] suggests that the optimal encoding should produce measurement distributions that appear random or noise-like. This maximizes the entropy of the measurements, ensuring that small changes in the object lead to distinguishable changes in the measurements, thereby maximizing the information content.

However, the preference for encoders that exhibit large changes in images in response to small object changes may not always be well suited to human interpretation. For example, in spatially coherent systems, even small changes in the object can lead to seemingly random, high-contrast interference patterns known as speckle [28]. Historically, these effects have been considered “noise,” and efforts were made to suppress them to produce more visually interpretable images. However, since information is agnostic to human interpretability, it

may be possible to use it to expand notions of useful signal to include what has previously been considered noise. A challenge that seems likely to arise is systems that are sensitive to small changes in objects will also be sensitive to small imperfections – so calibration will be especially important.

**Calibration** Calibration is a key challenge when applying information estimation to experimental data. Our approach assumes that the object itself and detection noise are the only sources of randomness in the measurement distribution, allowing us to estimate the object information  $I(\mathbf{O}; \mathbf{Y})$  by estimating the information shared between noisy and noiseless measurements  $I(\mathbf{X}; \mathbf{Y})$ . While these quantities are identical in simulated systems with controlled randomness, experimental data always contains some degree of variation from image to image caused by the system itself, such as optical imperfections, lens position shifts, or illumination changes. If unaccounted for, these factors can inflate information estimates by incorrectly attributing system randomness to object randomness.

Two approaches can mitigate this issue. First, physically reducing system randomness through proper maintenance, securing lenses, and using stable illumination sources will produce more consistent measurements, benefiting both information-based and traditional methods.

Second, calibration can account for remaining sources of randomness. Probabilistically, this involves predicting variations arising from the system itself to avoid misinterpreting them as object information. For example, illumination brightness changes in a microscope may appear as random object variations, but if predictable, they can be incorporated into the model to better fit the entropy of measurement distributions. This can be achieved through conditional information-accepting neural networks or physical process models that capture the randomness-producing mechanisms.

**Improved estimators** There remain many areas to improve upon our information estimators in future work. The estimators rely on probabilistic models of varying complexity - more flexible neural network-based models can improve accuracy but require more data and computational power. We’ve demonstrated two such models: a stationary Gaussian process and a PixelCNN-based model. It is quite possible that there are better choices in the accuracy-complexity tradeoff space that provide better performance with similar or lower computational requirements. Incorporating them could enhance the speed and accuracy of information estimation. An advantage of the upper bound approach of our estimator is that enhancements are easily measured - if a refined model achieves lower estimates for fixed data, it provably tightens the bound closer to the true value.

The accuracy-complexity tradeoff is particularly relevant for IDEAL, where our current implementation uses a multivariate Gaussian approximation to model the distribution of noisy measurements for computational efficiency. Though more complex models would almost certainly improve the accuracy of the information estimation, it remains an open question whether more accurate estimates are would actually meaningfully change the learned encoders.

**Outlook** Our approach can be used to design and understand the constraints of a wide range of imaging systems. We have demonstrated its application in studying optimal patterns for coded angle illumination, phase mask design in lensless imaging, and lens design for compressive 3D fluorescence microscopy. By using information as a guiding principle, this approach can potentially lead to the discovery of novel encoding schemes that maximize the information content of measurements while accounting for system constraints. Moreover, our framework can readily be extended to different imaging regimes, such as multi-channel images (e.g., hyperspectral imaging) and video data, opening up new possibilities for information-driven design in these domains.

In addition, since our probabilistic model on which our estimator is based is highly generic, our approach could likely be adapted to a wide variety of measurement systems and sensors beyond imaging. This could include electronic, biological, geological, and chemical sensors.

## Code

Code for the work described in this manuscript can be found at <https://github.com/Waller-Lab/EncodingInformation>.

## Acknowledgements

For helpful feedback and discussions about this work we thank T. Courtade, E. Aras, K. Lee, M. Foxxe, C. Degher, and J. Goodman.

# Supplementary Rabbit Hole

## S1 Information encoding formalism

Information theory enables quantification of uncertainty and randomness. A formal mathematical model of uncertainty and randomness requires probability. Thus in order to use information theory to analyze imaging systems, we must first construct a probabilistic model of the imaging system.

The description below assumes familiarity with basic concepts in probability theory and information theory. A tutorial introduction to these concepts can be found in our previous work [60], as well as the textbooks [37, 59] and Shannon's original paper introducing information theory [1].

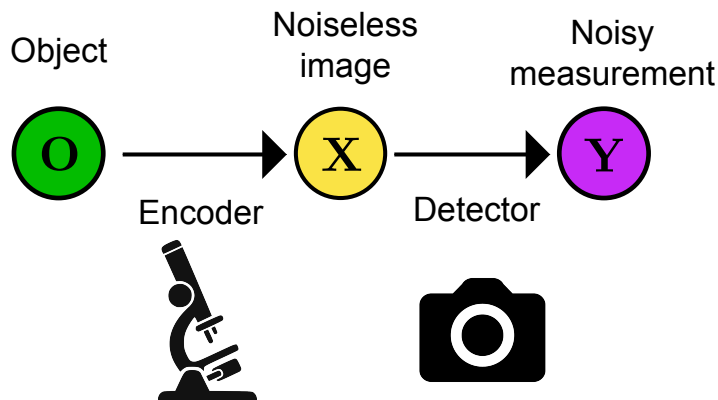


Figure S1: **A minimal probabilistic graphical model of an imaging system.** The object is a random variable that produces or modifies electromagnetic radiation. The encoder is a deterministic function that maps the object to a second random variable, the noiseless image. The detection process then stochastically maps the noiseless image to a third random variable, the noisy measurement. The arrows represent conditional dependencies between the random variables. The three random variables are connected in a Markov chain, meaning that the noisy measurement can only contain information about the object if it was also present in the noiseless image.

### S1.1 Minimal probabilistic model of an imaging system

A minimal probabilistic graphical model of an imaging system contains three random variables: the object, the noiseless image, and the noisy measurement (**Fig. S1**). These are modeled as random, because their exact properties are unknown.

The object either produces or modifies electromagnetic radiation incident upon it, and the resultant electromagnetic field is a function of the object’s physical properties. Since these properties are unknown, the object can be modeled as a random variable. The purpose of an imaging system is to reduce uncertainty about these properties by making a measurement of the object. It does this by using a physical imaging system to form a noiseless image on a sensor. The noiseless image is then measured through some detection process, which introduces an additional source of randomness, detection noise. The randomness introduced by detection noise will inevitably reduce our ability to infer the properties of the object from the measurement.

These three random variables are connected in a Markov chain. Mathematically, this means that the joint distribution  $p(\mathbf{o}, \mathbf{x}, \mathbf{y})$  can be factorized as  $p(\mathbf{o})p(\mathbf{x} | \mathbf{o})p(\mathbf{y} | \mathbf{x})$  or  $p(\mathbf{y})p(\mathbf{x} | \mathbf{y})p(\mathbf{o} | \mathbf{x})$ . The Data Processing Inequality [59] states that in such an arrangement, the mutual information between the object and the noisy measurement cannot exceed the mutual information between the noiseless image and the noisy measurement. Since there are no other sources of randomness in this minimal model, the mutual information between the noiseless image and the noisy measurement is equal to the mutual information between the object and the noisy measurement. Mathematically,  $I(\mathbf{X}; \mathbf{Y}) = I(\mathbf{O}; \mathbf{Y})$ .

Creating analytic models objects is not straightforward, in part because in all experimental situations they are unknown. As a result, unless we make extremely simplifying assumptions about them – e.g. that they have only two discrete possibilities as in the two point resolution example (**Sec. S1.3**) – direct estimation of  $I(\mathbf{O}; \mathbf{Y})$  will not be possible. Focusing instead on  $I(\mathbf{X}; \mathbf{Y})$  provides a tractable approach towards estimating information: quantifying information in the noisy measurement and subtracting the contribution of a well-understood noise process.

### S1.1.1 Separation of encoding and noise

Our model separates image encoding and noise using a “semi-classical” approach common in statistical optics ([28], Ch. 9) and has been proposed previously in general models of imaging systems [27]. This simplifying framework treats light classically until interacting with the detector, where quantum effects cause noise. The semi-classical method balances accuracy and simplicity between a more rigorous treatment based on quantum electrodynamics and purely classical models. For visible imaging with more than a few photons, it provides similar accuracy to quantum methods.

Within the semi-classical model, there are two potential sources of noise, classical and quantum. The classical noise arises from fluctuations in the intensity of light illuminating the object, which are characteristic of the physical process producing light. Classical examples include thermal light, as would be produced from the filament of a bulb, and laser light. Lasers in general produce light that is more stable, but nonetheless always have some degree of intensity fluctuation. Quantum noise arises from the fact the information is carried via photons whose behavior is governed by quantum mechanical effects. This inescapable randomness in photon arrival times is usually called “shot noise.”

In the visible region of the electromagnetic spectrum, quantum noise dominates classical noise, such that the latter can be ignored without affecting results. As a result, light can be treated as deterministic up to the point that it interacts with a photosensitive material (i.e. the detector) and the stochastic effects of quantum noise are realized. This approximation justifies considering encoding and detection to be considered in separate, independent steps.

### S1.1.2 Mathematical description of problem

There is a family of encoders  $\mathcal{E}$  consisting of functions  $e_\theta : \mathcal{O} \rightarrow \mathcal{X}$ , where  $\mathcal{O}$  is the domain - the space of possible objects,  $\mathcal{X}$  is the codomain - the space of possible noiseless images, and  $\theta$  is the parameter(s) that define a particular encoder. For example, in the case of a linear, shift-invariant encoder,  $\mathcal{E}$  would be the set of all linear, shift-invariant functions and  $\theta$  would define a specific point spread function.

The action of an encoder is to take an object  $o \in \mathcal{O}$  and form a noiseless image  $x \in \mathcal{X}$  of it. This noiseless image will then undergo a measurement process, resulting in a noisy measurement  $y \in \mathcal{Y}$ . The measurement process is modeled as a conditional probability distribution  $P_{\mathbf{Y}|\mathbf{X}}$ , which describes the probability of observing a particular noisy measurement given a particular noiseless image.

The information carried by noisy measurements is determined by the distributions  $P_{\mathbf{Y}|\mathbf{X}}$  and  $P_{\mathbf{X}}$ . It is quantified by the mutual information between the noiseless image and the

noisy measurement,  $I(\mathbf{X}; \mathbf{Y})$ , which can be expressed as:

$$I(\mathbf{X}; \mathbf{Y}) = \mathbb{E}_{\mathbf{X}} \left[ \mathbb{E}_{\mathbf{Y}} \left[ \log \left( \frac{p(x, y)}{p(x)p(y)} \right) \right] \right] \quad (2)$$

where  $p(x, y)$  is the joint probability of observing a particular noiseless image and a particular noisy measurement, and  $p(x)$  and  $p(y)$  are the marginal probabilities of observing a particular noiseless image and a particular noisy measurement, respectively.

Better encoders will produce noisy measurements that contain higher mutual information. It is thus of interest to investigate what limits the mutual information. One way of doing this is based on a decomposition of the mutual information into two terms:

$$I(\mathbf{X}; \mathbf{Y}) = H(\mathbf{X}) - H(\mathbf{X} | \mathbf{Y}) \quad (3)$$

$H(\mathbf{X})$  is the entropy of the noiseless images, and  $H(\mathbf{X} | \mathbf{Y})$  is the conditional entropy of the noiseless images given the noisy measurements, which quantifies the uncertainty about the noiseless images that remains after observing the noisy measurements.

There are multiple ways of mathematically modeling the space of noiseless images  $\mathbf{X}$ , which depends on whether the images are continuous or discrete over space and in energy. For example, a model of noiseless images over continuous space and energy would be a space of continuous functions over space which output real numbers corresponding to an amount of energy, whereas a discrete model would be a space of finite-dimensional vectors that take discrete values (the number of photons) at a discrete set of locations (the pixels). Combinations of these are also possible, such as a continuous model over space and discrete model over energy, or a discrete model over space and continuous model over energy.

With any model, the space of noiseless images is ultimately finite in some sense. Energy cannot be infinitely concentrated in a single point<sup>3</sup>, and the physics of wave-propagation effectively constrain electromagnetic waves to a finite number of degrees of freedom [61]. This means that even in the continuous/continuous case, any noiseless image can be represented to an arbitrary level of precision by a finite number of samples.

It is thus of interest to understand the limits of the entropy of the noiseless images, because this will determine the limits of the mutual information. The space  $\mathbf{X}$  will have either finite volume or finite cardinality, as dictated by physical constraints. A uniform distribution over this space, in which all noiseless images are equally likely, will have the maximum possible entropy. However, due to their physical constraints, encoders will not in general be able to produce noiseless images that are uniformly distributed over  $\mathbf{X}$ , leading to an inefficiency in the amount of information that can be carried by the noisy measurements.

## S1.2 Fundamental insights from a 1-dimensional example

To make these ideas more concrete, we consider a 1D example. This enables demonstration of the physical constraints and object-dependence of encoders, and the effect of system parameters on the amount of information that can be encoded. This provides deeper insights

---

<sup>3</sup>...without collapsing space into a black hole [61]

into the fundamental limits of information encoding, as well as connections to the existing literature analyzing information in imaging systems.

The family of encoders  $\mathcal{E}$  studied were 1D bandlimited, nonnegative, linear-shift invariant, infinitely periodic point spread functions. **Figure S2 a** shows the outputs of a representative encoder in this family (i.e. a specific point spread function) acting on a distribution of delta function objects. This system can be thought of as a simplified version of an imaging system that uses spatially incoherent illumination, such as in photography or microscopy [18].

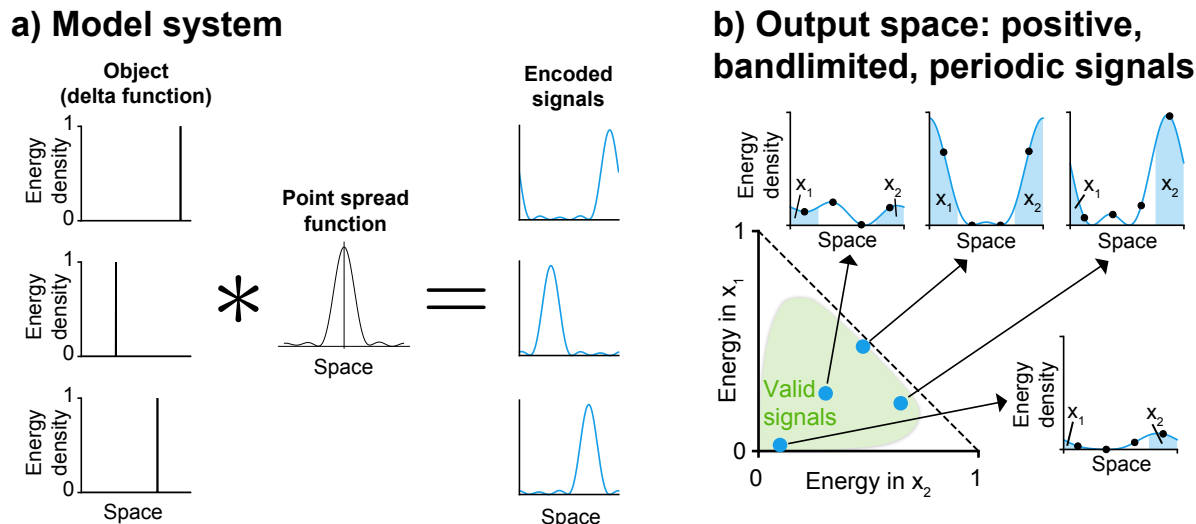


Figure S2: **1-dimensional model system.** **a)** An object distribution (e.g. a randomly located delta function) and a linear, shift-invariant point spread function encoder. **b)**  $M$ -dimensional energy coordinate representation of the set of all encodable signals in which each signal corresponds to a single point.

The set of possible output signals  $\mathbf{X}$  for this family of encoders is identical to the set of possible point spread functions: bandlimited, nonnegative, and infinitely periodic signals (**Fig. S4b**). These output signals (which are analogous to the noiseless images in **Section 1.1**) can be viewed either in spatial coordinates, in which their energy density is plotted as a function of space, or in energy coordinates, with values found by integrating areas of the signal corresponding to “pixels.”

In general, a signal cannot have both finite bandwidth and finite extent in space, and thus it takes an infinite number of samples to represent a particular signal with arbitrary accuracy. A common approximation is to assume that signals are approximately band-limited and of limited spatial extent, and to sample them at a finite density over a finite spatial extent. A more rigorous approach is to consider signals that are band-limited but have infinite spatial extent. Such signals can be shown to asymptotically have a finite number of degrees-of-freedom, and thus can be represented to an arbitrary level of accuracy by sampling at a finite rate [61].

Here, we avoid these complications by considering band-limited signals that are infinitely periodic in space. This means the signal can be represented exactly by sampling at the Nyquist rate over a single period (because sampling beyond this period would yield the same

values).

As a result of this simplification, there is a bijective mapping between the set of possible signals and non-negative vectors in  $D$ -dimensional space—that is, each signal in the set corresponds to a point in  $D$ -dimensional space (similar to the argument made in [19]). This allows us to computationally analyze this finite-dimensional space with insights that can be applied to the more complicated space of continuous signals.

Like the energy coordinate representation in **Section 1.1**, the effect of measurement noise in the energy coordinate representation is to turn a point (i.e. a signal/image) into a blob of probability mass representing the possible noisy realizations of that signal/image. Here we assume, without loss of generality, that all measurement noise is additive Gaussian (**Sec. S2.3.1**). The amount of information that can be encoded is determined by how well dispersed the distribution of encoded signals can be in this space such that the noisy versions of different signals minimally overlap. Thus, the volume of the space of possible signals is critical: it determines how much room there is to map different objects to non-overlapping signals. Though there are an infinite number of signals in the set, only a finite number can be distinguished with a given level of certainty in the presence of noise.

What is the volume of the space of possible signals? Given that all signals have energy  $\leq 1$ , the vector that defines their representation in energy coordinates must have  $L_1$  norm also  $\leq 1$ . Thus, all signals must correspond to points that lie inside the positive orthant of the  $L_1$  unit ball. However, not every point in this space will correspond to a valid signal: for example, a vector with a single 1 and the rest 0s will not be possible, because this would entail concentrating all of the signal’s energy within a single pixel.

It is unclear to us if there is an analytical expression that defines the set of possible signals, but the size of this set can be investigated experimentally. To do so, we set up an optimization problem in which we pick a fixed object and a target energy coordinate representation of a signal (e.g. a vector with a single 1 and the rest 0s). We then use gradient descent to find the optimal point spread function that brings the object closest to the target signal. Repeating this experiment over a grid of target signals shows which signals can be reached, and which cannot, thereby revealing the limits of the space of possible signals.

Repeating this experiment with different fixed objects illustrates an important insight about encoders: Their range is object dependent (**Fig. S3**). This is a direct of their physical constraints. The 1D encoder in this simulation is representative of imaging systems governed by intensity point spread functions [18]. Such encoders have at least two important physical constraints: 1) they can only reduce energy (if they attenuate light) or preserve it. They cannot, for example, encode a dim object to a signal with greater energy. 2) They can only disperse, and not re-concentrate, energy. Every point spread function (under the constraints of non-negativity and linear shift invariance) can only map objects to signals that are blurrier versions of it.

Figure S3 shows the consequence of the second constraint for three different objects with equal energy. The single delta function in the top row can be encoded to the broadest range of possible signals, since it is the most concentrated to begin with. More dispersed objects, like the 8 delta functions each with  $\frac{1}{8}$  energy in the bottom row can only be encoded to a smaller volume of possible signals.

The range of a family of encoders for a fixed object of a particular type determines

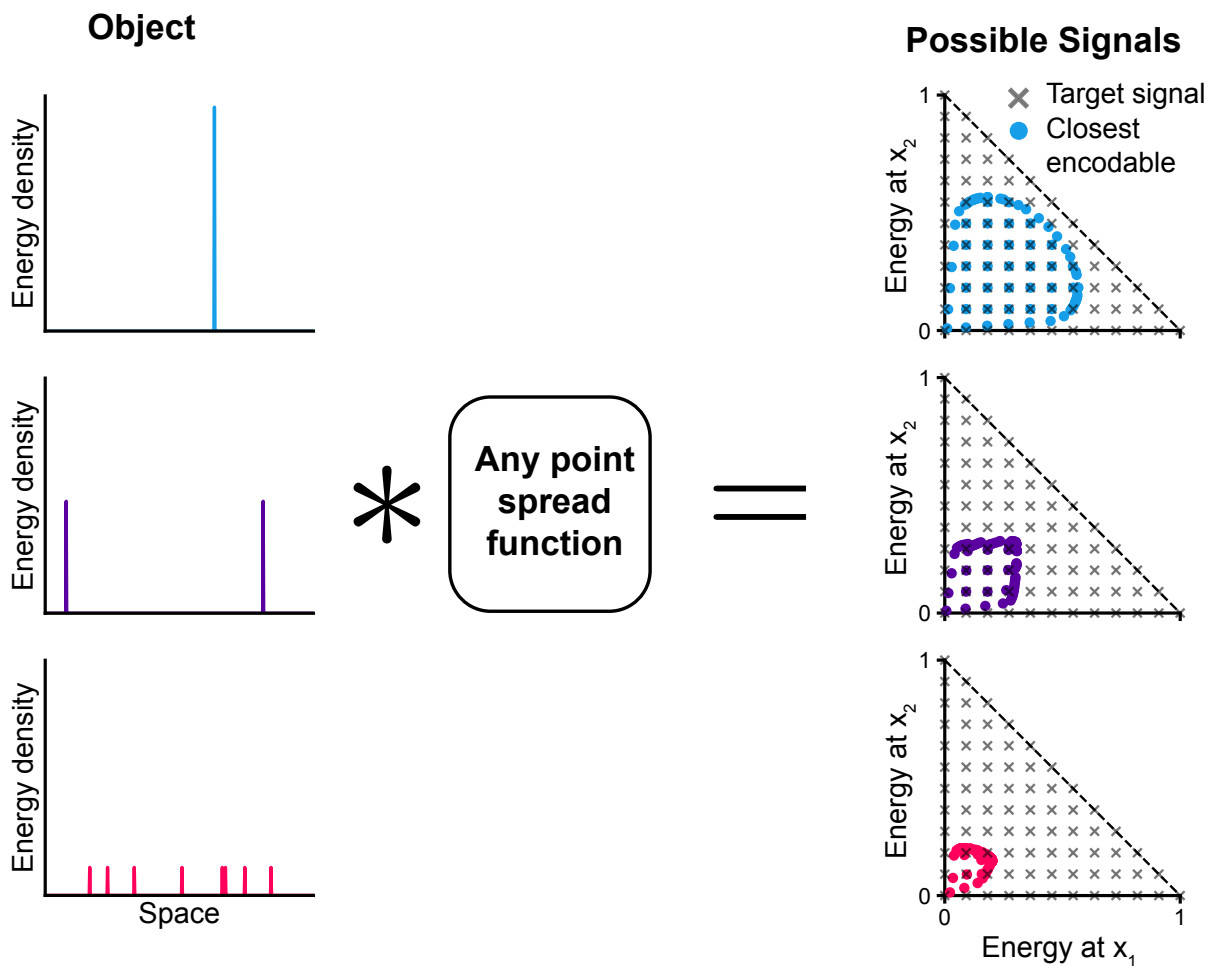


Figure S3: **Object-dependence of encoder range.** The set of signals encodable from an object depends on that object’s properties. More dispersed objects like the 8 delta functions (bottom) can only reach a subset of the signals reachable from a concentrated delta function (top), despite equal energies. This is due to physical constraints preventing reconcentrating light. The closest encodable signals to the target signals were found by solving an optimization problem to find the optimal encoder that encodes the object to the target signal.

the volume of the set of possible encoded signals, and thus places an upper limit on the amount of encoded information. However, since encoder families are constrained in the class of functions they can form, they will not, in general, be able to encode to the optimal distribution of signals (which, for additive Gaussian noise, is a uniform distribution over the set of possible signals). This is because a particular encoder does not just map one object to a single signal, but rather a distribution of objects to a distribution of signals. Even if it is possible to encode each object among a set to a specific signal individually, doing so may require a different encoder for each object, and thus it is not possible to encode the entire set of objects to the entire set of signals simultaneously with a specific encoder.

For a particular distribution of objects, a constraint on the amount of energy in the encoded signals, and a particular type of measurement noise, the optimal distribution of signals that can be encoded is the one that maximizes the mutual information between the encoded signals and the objects. However, due to physical constraints and object dependence of encoders, this optimal distribution may not be realizable by a particular encoder family. The gap between the optimal distribution of encoded and the best encodable distribution of signals is a measure of the inefficiency of the encoder family.

This **encoder inefficiency** can be experimentally estimated. Using an object distribution of delta functions with different positions and unit energy and additive Gaussian measurement noise, the optimal distribution of signals is a uniform distribution over the set of possible signals. To find the best encodable distribution, we must pick a particular distribution of objects and find the encoder within the family of encoders that maximizes the mutual information between the encoded signals and noisy measurements. For this experiment, we use a delta function object with random position and unit energy, and use Information-Driven Encoder Analysis Learning (IDEAL) (**Sec. 1.4**) to learn an optimal encoder. (Unsurprisingly, the optimal encoder learned in this simple 1D scenario is a concentrated function resembling a sinc function.) Using this encoder, we can then sample from the distribution of encoded signals by generating a random object (a delta function with a random position) and convolving it with the point spread function. Repeating this process many times yields a distribution of encoded signals, to which we add noise, and estimate the mutual information. To estimate mutual information, we took the noisy, pixelated versions of the signals in an  $N \times D$  matrix, where  $N$  is the number of samples and  $D$  is the number of pixels, and reshaped them into  $N \times \sqrt{D} \times \sqrt{D}$  “images”, so that we could use the PixelCNN-based mutual information estimator (**Sec. S2.5.3**).<sup>4</sup>

The results of this experiment are shown in **Figure S4**. The optimal point spread function encodes objects to only a small fraction of the total volume of possible signals, resulting in encoded signals that are significantly less random in appearance than the optimal uniform distribution of signals. (Note: the energy coordinate representation of these signals shown on the left side is a 2-dimensional projection of an  $D$ -dimensional space, with  $D = 4$  for the picture shown, which is why the distribution appears non-uniform.) The mutual information estimates shown on the right side demonstrate the gap between the optimal distribution of signals and the best encodable distribution given the family of linear, shift-

---

<sup>4</sup>Notably, using the PixelCNN was for experimental convenience, since this mutual information estimator is designed for images, and not 1D signals. More accurate results may be obtainable by using a mutual information estimator that uses a probabilistic model that is designed for 1D or general signals such as [62, 63].

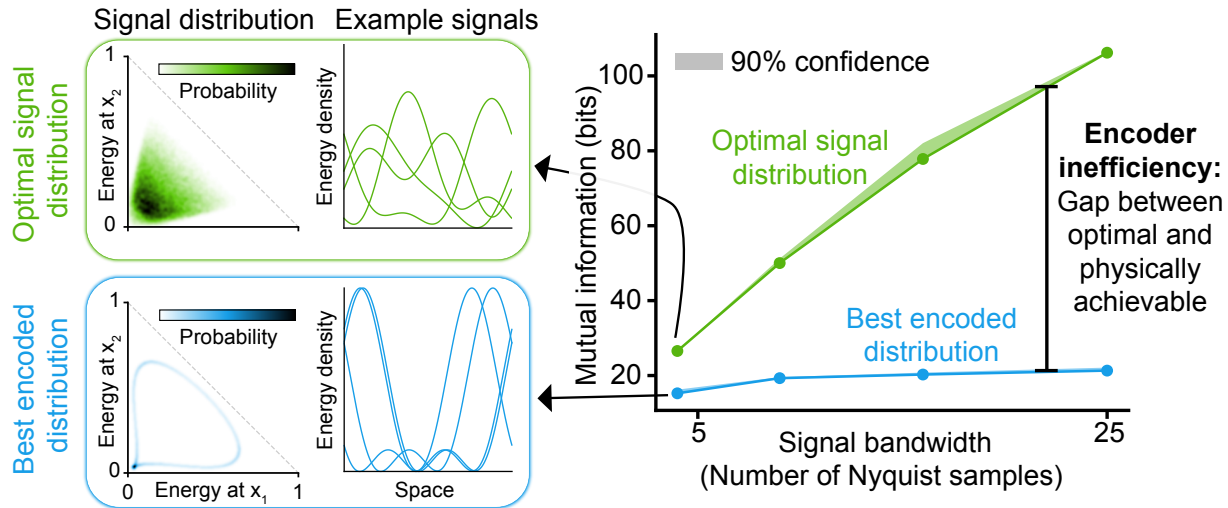


Figure S4: **Physical constraints limit the amount of information that can be encoded.** (Top left) The optimal distribution of energy limited signals for additive, signal-independent Gaussian noise is uniform (it appears non-uniform in this 2D projection of a 4D space). (Bottom left) The best encodable distribution using an optimal point spread function is far from uniform. (Right) The gap between the information in the optimal signal distribution and the best encodable distributions quantifies the inefficiency of the encoder family.

invariant encoders.

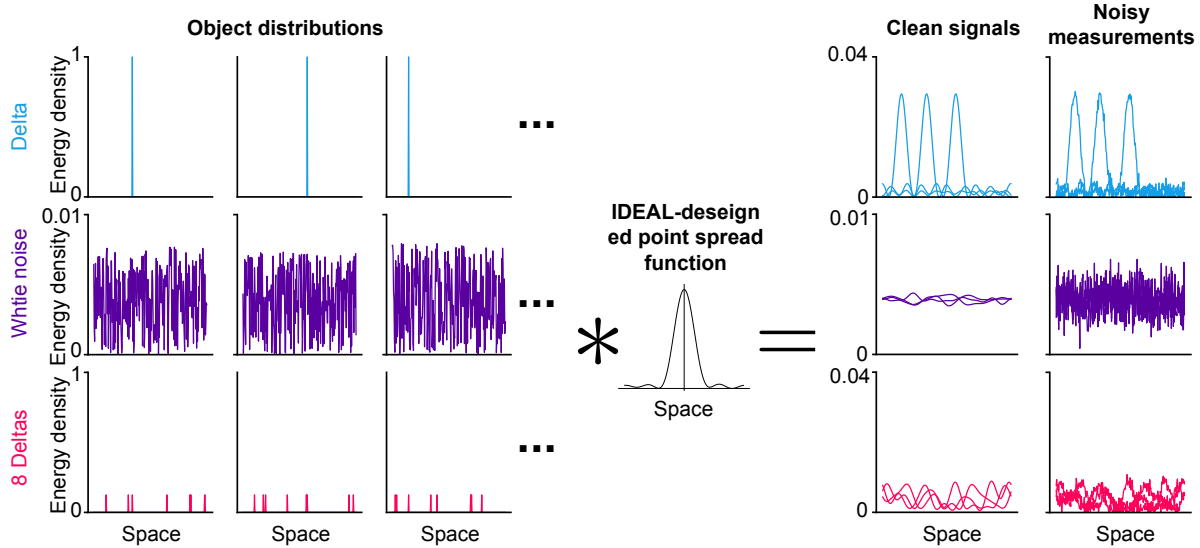
### S1.2.1 The effect of system parameters on encoded information

This same experimental setup can be used to investigate how different properties of the encoder/detection process, such as bandwidth, signal-to-noise ratio, and sampling density, affect the amount of information that can be encoded. These experiments provide insight into the tradeoffs between different system parameters as well as connections to the existing literature analyzing information in imaging systems.

**Signal-to-noise ratio** Signal-to-noise ratio is a key parameter in imaging systems, and it is widely-appreciated that higher signal-to-noise ratio is a desirable characteristic. For the additive Gaussian noise measurement model, noise is fixed, and the signal-to-noise ratio is determined by the amount of energy in the signal. It is simplest to consider the average signal-to-noise ratio over each signal, which can be found by dividing the energy of the signal by the standard deviation of the noise. Choosing an maximum average signal-to-noise ratio defines a set of signals that can be encoded, which consists of all possible signals with this average signal-to-noise ratio or less. This set has a finite volume, and thus a finite maximum amount of information that can be encoded. Within this set, there are subsets of signals that each have the same signal-to-noise ratio.

Sets of signals with higher average signal-to-noise ratios have increasing large volumes, and can thus carry larger amounts of information. As described in the previous section,

### a) Experimental framework



### b) Effects of measurement properties on information

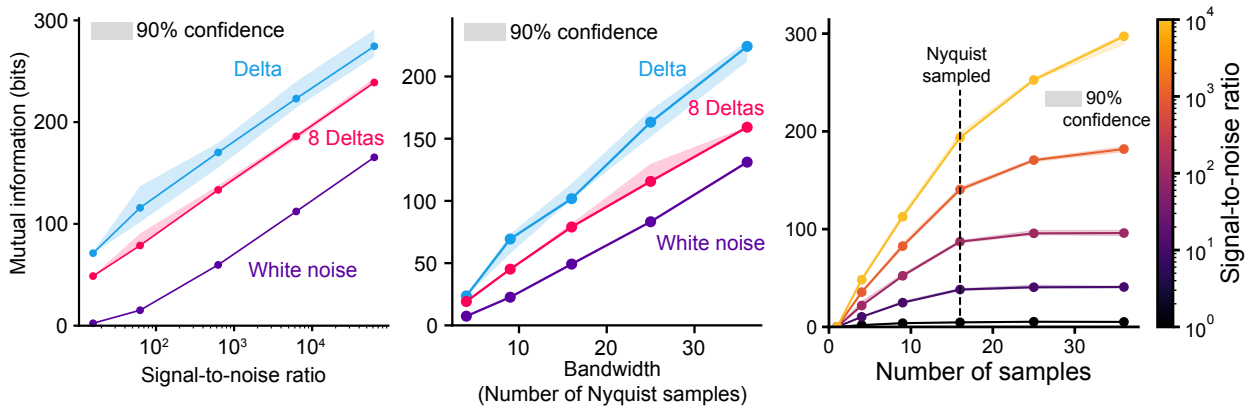


Figure S5: **Effects of signal-to-noise, space-bandwidth product, and sampling density on encoded information.** a) Samples from three different object distributions and the signals and noisy measurements to which they are encoded with an optimal point spread function. b) The amount of encoded information increases (Left) logarithmically with the average signal-to-noise ratio with object-dependent rates, (Middle) linearly with the space-bandwidth product of the signal with object-dependent rates. (Right) Sampling signals of fixed bandwidth at increasing densities increases the amount of encoded information, but with diminishing returns across different signal-to-noise ratios (for the 8 delta object distribution).

physical constraints of encoders impose object-dependent limits on the the maximum amount of information that can be encoded. To test how the maximum average signal-to-noise ratio affects the amount of information that can be encoded, we repeated the procedure described on three different distributions of objects: single, randomly-located, unit-energy delta functions, 8 randomly-located, delta functions each with  $\frac{1}{8}$  energy, and unit energy white noise patterns (note, these are objects, not measurement noise) (**Fig. S5a**). The results show that for all three object distributions, the best encodable distribution of signals grows logarithmically with the average signal-to-noise ratio, with different objects having different absolute amounts of information for a given signal-to-noise ratio (**Fig. S5b**). This is consistent with the intuition that higher signal-to-noise ratio allows for more information to be encoded, and that the amount of information that can be encoded is object-dependent.

**Space-bandwidth product** Next, we tested the effect of signal bandwidth on information capacity. Optical imaging systems are often characterized in terms of their space-bandwidth product [15], and the space-bandwidth product is often used synonymously with the word “information”. A more accurate term for the space-bandwidth product is “degrees of freedom,” since it quantifies the potential complexity of an electromagnetic field wave propagating through the system [61], while information (in Shannon’s entropy/mutual information sense) also depends on the signal-to-noise ratio and the object-dependent ability of encoders to map to distinct signals. In our numerical simulation, the spatial extent of signals is fixed, so increasing the bandwidth of the signal increases the space-bandwidth product. We found that captured information increases linearly with the space-bandwidth product, with rate of increase depending on the object distribution (**Fig. S5c**).

**Sampling density** Finally, we examined the effect of sampling density on the amount of information that can be encoded. For a fixed bandwidth, the sampling density determines the number of pixels in the signal. The Nyquist sampling theorem [64, 19] states that a bandlimited signal can be perfectly reconstructed from its samples if the sampling density is at least twice the bandwidth. However, in the presence of noise, even when sampling at the Nyquist rate, there remains residual uncertainty about the signal, and additional samples can reduce this uncertainty. Experimentally, we found that, as expected, increasing the sampling density increases the amount of information, even beyond the Nyquist rate (**Fig. S5d**). However, the additional increases in information were progressively smaller. These results were consistent across both different object distributions and different average signal-to-noise ratios (for a delta function object distribution).

### S1.3 Probabilistic two-point resolution

In this section we present the example from the main paper of 1-dimensional two-point resolution (**Fig. 1b,c**) in full mathematical detail. By making assumptions about the object distribution, the encoder, and the noise model, we can write down the exact probability density functions of the object, the noiseless image, and the noisy measurement. This enables writing an exact expression for the mutual information between object and noisy measurement, as well as the classification accuracy of the optimal binary classifier decoder that uses

the noisy measurement to classify the object as being a single-point source or two point sources.

**Object** The object is a mixture of two possibilities that each occur with probability  $\frac{1}{2}$ : Either a single point source with energy 1 or two point sources with energy  $\frac{1}{2}$  and separation distance  $\Delta$  with their midpoint at the same location as the single point source. We represent these objects mathematically as  $\mathbf{o}_1$  and  $\mathbf{o}_2$  respectively. Using  $r$  to denote spatial position, with the single-point source object located at  $r = 0$ :

$$\begin{aligned}\mathbf{o}_1(r) &= \delta(r) \\ \mathbf{o}_2(r) &= \frac{1}{2}\delta\left(r - \frac{\Delta}{2}\right) + \frac{1}{2}\delta\left(r + \frac{\Delta}{2}\right)\end{aligned}$$

where  $\delta$  is the Dirac delta function.

The random object  $\mathbf{O}$  has probability  $\frac{1}{2}$  of being  $\mathbf{o}_1$  and  $\frac{1}{2}$  of being  $\mathbf{o}_2$ . Thus, its probability density function can be written as:

$$p(\mathbf{o}) = \frac{1}{2}\delta(\mathbf{o} - \mathbf{o}_1) + \frac{1}{2}\delta(\mathbf{o} - \mathbf{o}_2)$$

$\delta(\mathbf{o} - \mathbf{o}_1)$  is 1 when the object is  $\mathbf{o}_1$  and 0 otherwise, and similarly for  $\delta(\mathbf{o} - \mathbf{o}_2)$ .

**Encoder** The encoder is a 1-dimensional linear shift-invariant imaging system with a diffraction-limited intensity point spread function  $h(r)$ :

$$h(r) = \frac{\sin\left(\frac{2\pi\text{NA}}{\lambda}r\right)}{\frac{2\pi\text{NA}}{\lambda}r}$$

where NA is the numerical aperture of the system,  $\lambda$  is the wavelength of light, and  $r$  is the spatial coordinate.

The noiseless image is the convolution of the object with the point spread function:

$$\mathbf{x} = \mathbf{o} * h$$

This gives rise to two possible noiseless images,  $\mathbf{x}_1$  and  $\mathbf{x}_2$ , corresponding to the two possible objects  $\mathbf{o}_1$  and  $\mathbf{o}_2$  respectively. The probability density function of the random noiseless image  $\mathbf{X}$  is thus:

$$p(\mathbf{x}) = \frac{1}{2}\delta(\mathbf{x} - \mathbf{x}_1) + \frac{1}{2}\delta(\mathbf{x} - \mathbf{x}_2)$$

**Detector** The noisy measurement is formed by adding independent Gaussian noise with variance  $\sigma^2$  to each pixel of the noiseless image. We assume a pixel size much smaller than the minimum pixel size dictated by the Nyquist sampling theorem, so sampling effects minimally influence the results.

The random noisy measurement  $\mathbf{Y}$  is thus a length  $D$  vector of pixels. Its probability distribution is found by taking the mixture of two deltas distribution of the noiseless images and adding Gaussian noise to each pixel. This gives a mixture of two multivariate Gaussian distributions with mean vectors given by the noiseless images and a diagonal covariance matrix with variances equal to the noise variance. The probability density function of the noisy measurement is thus:

$$p(\mathbf{y}) = \frac{1}{2}\mathcal{N}(\mathbf{y}; \mathbf{x}_1, \sigma^2 I) + \frac{1}{2}\mathcal{N}(\mathbf{y}; \mathbf{x}_2, \sigma^2 I) \quad (4)$$

where  $\mathcal{N}(\mathbf{y}; \mathbf{x}, \sigma^2 I)$  is the multivariate Gaussian distribution with mean vector  $\boldsymbol{\mu} = \mathbf{x}$  and covariance matrix  $\boldsymbol{\Sigma} = \sigma^2 I$ .

**Mutual information** The mutual information between the object and the noisy measurement  $I(\mathbf{O}; \mathbf{Y})$  is equal to the mutual information between the noiseless image and the noisy measurement  $I(\mathbf{X}; \mathbf{Y})$ , since the object is fully determined by the noiseless image. We focus on the mutual information between the noiseless and noisy images, which can be calculated by decomposing it into a difference of entropies:

$$I(\mathbf{X}; \mathbf{Y}) = H(\mathbf{Y}) - H(\mathbf{Y}|\mathbf{X})$$

where  $H(\mathbf{Y})$  is the entropy of the noisy measurement and  $H(\mathbf{Y}|\mathbf{X})$  is the conditional entropy of the noisy measurement given the noiseless image.

Under the additive Gaussian noise model,  $H(\mathbf{Y}|\mathbf{X})$  is a constant that is a function of the the variance  $\sigma^2$  and the number of dimensions (pixels)  $D$ . It can be analytically simplified as shown in equation 17.

The entropy of the noisy measurement  $H(\mathbf{Y})$  can be expanded as:

$$H(\mathbf{Y}) = -\mathbb{E}[\log p(\mathbf{y})]$$

Since we can easily generate samples from the distribution of the noisy measurements and we know the true probability density  $p(\mathbf{y})$ , we can estimate this entropy with a Monte Carlo approximation of  $N$  samples:

$$H(\mathbf{Y}) \approx -\frac{1}{N} \sum_{i=1}^N \log p(\mathbf{y}_i)$$

**Decoder** Since the goal of the imaging system in this simple example is to classify the object as being a single point source or two point sources [29], the decoder is a binary classifier that takes in the noisy measurement and outputs a decision as to whether the object was a single point or two points.

The optimal decoder is the Bayes classifier, which chooses the object class that maximizes the posterior probability given the noisy measurement. In this case, since the prior probabilities of the two object classes are equal, the Bayes classifier is equivalent to the maximum likelihood classifier, which chooses the object class that maximizes the likelihood of the noisy measurement.

Given the probability density of the noisy measurement in equation 4, the Bayes/maximum likelihood classifier decides the object is two points if:

$$\mathcal{N}(\mathbf{y}; \mathbf{x}_2, \sigma^2 I) > \mathcal{N}(\mathbf{y}; \mathbf{x}_1, \sigma^2 I)$$

Plugging in the expressions for the multivariate Gaussian distributions, this simplifies to:

$$\|\mathbf{y} - \mathbf{x}_2\|^2 < \|\mathbf{y} - \mathbf{x}_1\|^2$$

In other words, the noisy measurement  $\mathbf{y}$  is classified as two points if its Euclidean distance to the noiseless image  $\mathbf{x}_2$  is less than its distance to  $\mathbf{x}_1$ , and classified as one point otherwise.

Using the analytic expressions for mutual information and classification accuracy, they can be shown to have a monotonic relationship with each other (**Fig. S6**). This demonstrates the fundamental link between the information content of the measurements and the achievable performance of downstream decoding in this minimal example.

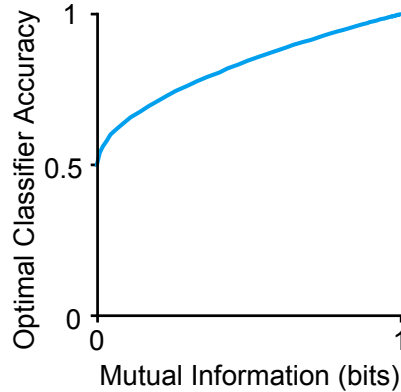


Figure S6: **Classification accuracy vs information in two-point resolution.** Performance of the optimal binary classifier decoder that uses the noisy measurement to classify the object as being a single point source or two point sources. The classification accuracy in this simple example has a monotonic relationship with the mutual information between the object/noiseless image and the noisy measurement.

## S1.4 Expanded model

The minimal model from the previous sections makes simplifying assumptions and abstracts away details that are relevant to real imaging systems. In the section we generalize to a more complex model, and explain the deeper insights and capabilities such a model can provide.

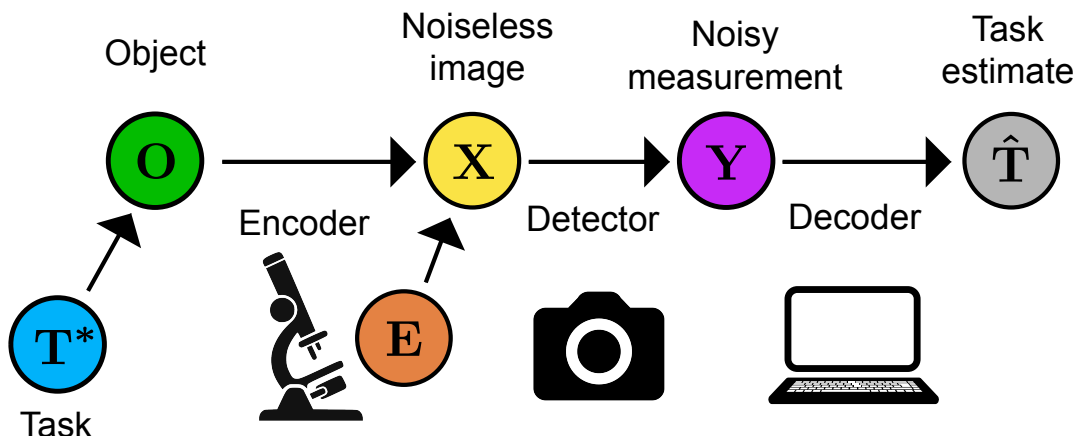


Figure S7: **An expanded probabilistic graphical model of an imaging system.** A generalization of the minimal probabilistic model in **Figure S1**, which in addition to modeling the object, noiseless image, and noisy measurement as random variables, also models randomness of the encoder, and the true and estimated values of the decoder task.

### S1.4.1 Encoder uncertainty and calibration

In the minimal model in the previous sections, the encoder function is fixed, so all variations in the noiseless images come from variations in the objects. This enables the simplifying assumption that the mutual information between the noisy measurements and noiseless images equals the mutual information between the noisy measurements and the objects:  $I(\mathbf{Y}; \mathbf{X}) = I(\mathbf{Y}; \mathbf{O})$ . As a result, estimating the former also reveals how much information about the objects is contained in the noisy measurements.

However, in practice the encoder may vary for different objects. For example, dust or imperfections in optical components, fluctuations in illumination brightness, and non-uniform resolution across the field of view can all change from measurement to measurement. Imaging systems are generally designed to minimize such variations - lenses provide uniform resolution across the field of view, light sources are engineered for stability, and care is taken to avoid dust in the optical path. But some degree of variation is inevitable.

As a result, observing noisy measurements provides information both about the object and about the measurement system itself. Not accounting for encoder variations will lead to overestimates of the object information contained in the measurements.

The randomness of encoders is qualitatively different than the randomness caused by detection noise. Detection noise arises from inherently unpredictable quantum phenomena

like photon arrival times. In contrast, the randomness of the encoder models a fixed but unknown distortion applied to the signal that can be learned.

Mathematically, the encoder sits outside the Markov chain from object to image. Thus the data processing inequality does not imply permanent information loss as a result of its randomness. Through calibration, the nature of the distortion can be learned. Once characterized, the apparent randomness in future measurements is reduced, enabling recovery of information about the object. There are many examples of this concept in practice - deconvolution algorithms can incorporate spatially varying point spread functions, shading corrections can be applied to account for varied illumination of the field of view [65, 66], etc.

A similar calibration approach can be taken with information estimators to avoid over-estimating the object information in the measurement. We describe this further in the context of our information estimation strategy in **Section S2.6**.

### S1.4.2 Task-specific information

Another useful generalization is to explicitly model the relationship between the decoding task and the object being imaged. For example, a perfect decoder for a specific task may require only a subset of the information needed to fully describe the object’s physical properties. Alternatively, even complete knowledge of the object’s physical properties may be insufficient to perfectly predict the task outcome - no encoder could encode enough task-relevant information to enable a flawless decoder.

To account for this, the model includes an additional random variable:

$\mathbf{T}^*$  - the true value of the decoding task, which sits upstream of the object  $\mathbf{O}$  in the Markov chain. This expresses that the object may not contain all task-relevant information, and also may contain additional irrelevant details.

The full Markov chain is now  $\mathbf{T}^* \rightarrow \mathbf{O} \rightarrow \mathbf{X} \rightarrow \mathbf{Y}$ . The key quantity of interest is  $I(\mathbf{T}^*; \mathbf{Y})$ , the mutual information between the true task value and the noisy measurement. This quantifies how much task-relevant information makes it through the entire imaging system. It can be substantially less than  $I(\mathbf{O}; \mathbf{Y})$ , as it excludes both irrelevant object details.

The greater the disparity between  $I(\mathbf{T}^*; \mathbf{Y})$  and  $I(\mathbf{O}; \mathbf{Y})$ , the less predictive estimated information may be of decoder performance.

This seems especially likely when the task is very simple, capturing just a small fraction of the information in the measurements about the full object state. As an example, in **Section S4** we observe a scenario where a simple classification task requires only a small fraction of the information present in the full measurements.

## S2 Estimating information: Theory

### S2.1 Overview

Using the minimal probabilistic model of an optical system described in **Section 1.1**, the object-relevant information in the noisy measurements can be quantified. Here,  $\mathbf{X}$  is a random 2D array of pixels with distribution  $p(\mathbf{x})$ , where each element quantifies the expected amount of energy (in photons) at a pixel of a noiseless image formed on a sensor.  $\mathbf{Y}$  is a

random 2D array of the same shape with distribution  $p(\mathbf{y})$ , where each element quantifies the amount of energy at that pixel in the noisy measurement.

The objective is to estimate  $I(\mathbf{X}; \mathbf{Y})$ , the mutual information between the noiseless image and the noisy measurement. This quantity has units of bits, which has the operational significance that for each bit collected,  $2^{I(\mathbf{X}; \mathbf{Y})}$  different objects can be perfectly discriminated in the presence of noise (i.e. with no overlap in their distributions of noisy measurements). In practice, however, different objects cannot be unambiguously identified in the presence of noise, so each bit quantifies multiple states that can be partially discriminated and how well.

Optical systems often exhibit varying performance across their field of view, both in resolution and in information content. However, it is often mathematically and conceptually convenient to ignore their field-varying optical performance and instead model them as shift-invariant, thereby enabling a single global quantification of their resolution [18]. Similarly, it is a convenient simplification to express the variation in information across the field of view with a single scalar quantity. To do so, we model the random variables  $\mathbf{X}$  and  $\mathbf{Y}$  as stationary stochastic processes, meaning their probability distributions are invariant to translations across the field of view. The information in such a model is quantified by the mutual information rate, which is the mutual information per pixel.

## S2.2 Mutual information estimator

Mutual information estimation is a well-studied problem in many fields, including machine learning, neuroscience, and computational biology, and a number of different approaches have been proposed, some of which attempt to estimate mutual information directly [32, 33, 34], and others which try to infer its value by computing upper or lower bounds [35, 36]. It is a challenging statistical problem to solve in general, and many estimators and bounds are known to suffer from high bias and/or variance, particularly on high-dimensional problems [35, 36].

Many mutual information estimators rely on first estimating entropy, which is a measure of the uncertainty of a random variable (**Fig. 2a**). The outcome of random variables with higher entropy are more uncertain and harder to predict than the outcome of those with lower entropy, because they are more random. Equivalently, the higher a distribution's entropy is, the more spread out it is, and the harder it would be to digitally compress samples from it. Mathematically, entropy is defined as the expected value of the negative log of the probability density/mass function:

$$H(\mathbf{Y}) = -\mathbb{E}[\log p(\mathbf{Y})] \quad (5)$$

Like mutual information estimation, there is a large body of literature on entropy estimation and many different approaches have been proposed [67], including those that form an estimate of the probability density function  $\hat{p}(\mathbf{y})$  and plug it into the definition of entropy, and those that estimate entropy based on the similarity of samples from  $p(\mathbf{y})$  [68, 69, 70]. Both approaches, however, face difficulties in high dimensions.

There are multiple ways of decomposing mutual information into a difference of entropies. Our approach is based upon the decomposition (**Fig. 2b**):

$$I(\mathbf{X}; \mathbf{Y}) = H(\mathbf{Y}) - H(\mathbf{Y} | \mathbf{X}) \quad (6)$$

Here,  $H(\mathbf{Y})$  is the entropy of the noisy image distribution  $p(\mathbf{y})$  (**Fig. 2c**). Both variations in the object and measurement noise contribute to the randomness of measurements. We are interested in the information about the object, thus to quantify how much of these variations the measurements contain, we must subtract the entropy contributed by the noise,  $H(\mathbf{Y} | \mathbf{X})$  (**Fig. 2d**).

This decomposition is particularly useful for the problem of estimating mutual information in optical imaging, because the conditional entropy  $H(\mathbf{Y} | \mathbf{X})$  can be greatly simplified due to the fact that commonly used analytic noise models in optical imaging can generally be computed for each pixel independently.

(A technical note: the outcomes of the random variables  $\mathbf{X}$  and  $\mathbf{Y}$  in our model are discrete, because they are 2D arrays of pixels, where each pixel takes on an intensity value that is an integer number of photons. However, for computational simplicity, we will approximate them as continuous random variables and use differential entropy instead of discrete entropy [59, 37]. These approximations break down at very low photon counts, less than  $\sim 20$  photons, so in this paper, we use only data with photon counts greater than this. A possible direction of future work is to extend our approach to work with discrete random variables, which would allow it to be applied to data with lower photon counts.)

We begin by describing the simpler of the two terms to estimate, the conditional entropy  $H(\mathbf{Y} | \mathbf{X})$ .

### S2.3 Estimating Conditional Entropy of Measurement Noise

The conditional entropy of noisy measurements given noiseless images can be written out in terms of expectations over the logarithm conditional probability of noisy measurements given a noiseless image  $p(\mathbf{y} | \mathbf{x})$ :

$$H(\mathbf{Y} | \mathbf{X}) = -\mathbb{E}_{\mathbf{X}} [\mathbb{E}_{\mathbf{Y}} [\log p(\mathbf{Y} | \mathbf{X})]] \quad (7)$$

$p(\mathbf{y} | \mathbf{x})$  embodies the various sources of noise in the detection process, including photon shot noise, detector read noise, etc. Here, we utilize established analytic models of detection noise in optical imaging [28]. Empirical results suggest that the true noise in systems deviates from these models in low-light conditions [71], but since our experiments are conducted in the high-light regime, we will assume that these models are accurate for the purposes of this paper. A possible direction for future work is to learn more accurate noise models from the data, as was done in [72].

Assuming we have access to a dataset of  $N$  samples from the distribution of noiseless images  $\{\mathbf{x}^{(1)}, \mathbf{x}^{(2)}, \dots, \mathbf{x}^{(N)}\}$ , the outer expectation can be estimated through Monte Carlo approximation:

$$-\mathbb{E}_{\mathbf{X}} [\mathbb{E}_{\mathbf{Y}} [\log p(\mathbf{Y} | \mathbf{X})]] \approx -\frac{1}{N} \sum_{i=1}^N \mathbb{E}_{\mathbf{Y}} [\log p(\mathbf{Y} | \mathbf{x}^{(i)})] \quad (8)$$

$$= -\frac{1}{N} \sum_{i=1}^N H(\mathbf{Y} | \mathbf{x}^{(i)}) \quad (9)$$

Here,  $H(\mathbf{Y} | \mathbf{x}^{(i)})$  is the conditional entropy of the distribution of noisy images given the  $i$ th noiseless image.

**Conditionally independent noise at each pixel**  $H(\mathbf{Y} | \mathbf{x}^{(i)})$  is a function of the noise introduced in the detection process, which is modeled by the probability distribution  $p(\mathbf{y} | \mathbf{x}^{(i)})$ . In optical imaging, common analytic noise models like additive Gaussian and Poisson shot noise typically assume that the noise at each pixel is conditionally independent of the noise at other pixels, given the true (noiseless) pixel value. When this is true,  $p(\mathbf{y} | \mathbf{x}^{(i)})$ , which is a joint distribution over all  $D$  pixels in the noisy measurement, can be simplified by factoring it into a product of scalar distributions for each pixel, where  $y_k$  and  $x_k^{(i)}$  are the intensity values at the  $k$ th pixel in the noisy measurement and the  $i$ th noiseless image, respectively:

$$\begin{aligned} p(\mathbf{y} | \mathbf{x}) &= p(y_1, y_2, \dots, y_D | x_1^{(i)}, x_2^{(i)}, \dots, x_D^{(i)}) \\ &= \prod_{k=1}^D p(y_k | x_k^{(i)}) \end{aligned}$$

This factorization simplifies the calculation of conditional entropy, because it is much easier to compute  $D$  scalar conditional entropies than a single joint conditional entropy over  $D$  variables. Mathematically, this simplification can be seen by plugging the factorized distribution into the definition of conditional entropy:

$$H(\mathbf{Y} | \mathbf{x}^{(i)}) = -\mathbb{E}_{\mathbf{Y}} \left[ \log \prod_{k=1}^D p(y_k | x_k^{(i)}) \right] \quad (10)$$

$$= -\mathbb{E}_{\mathbf{Y}} \left[ \sum_{k=1}^D \log p(y_k | x_k^{(i)}) \right] \quad (11)$$

$$= -\sum_{k=1}^D \mathbb{E}_{\mathbf{Y}} \left[ \log p(y_k | x_k^{(i)}) \right] \quad (12)$$

$$= \sum_{k=1}^D H(Y_k | x_k^{(i)}) \quad (13)$$

Here,  $H(Y_k | x_k^{(i)})$  is the conditional entropy of the  $k$ th pixel in the noisy image given the intensity of the  $k$ th pixel in the noiseless image.

This is a scalar quantity and can be calculated analytically for many common noise models. We will discuss two such models here: additive Gaussian noise and Poisson noise.

### S2.3.1 Conditional entropy with additive Gaussian noise

Additive Gaussian noise is a simple noise model often used in optical images, especially in low-light conditions where the read noise of the detector is the dominant source of noise. In this model, the noise at each pixel is drawn from a Gaussian distribution with mean zero and variance  $\sigma^2$ . Mathematically:

$$\begin{aligned} Y_k &= X_k + N_k \\ N_k &\sim \mathcal{N}(0, \sigma^2) \end{aligned}$$

The entropy of a (scalar) Gaussian distribution  $\mathcal{N}(\mu, \sigma)$  is [59]:

$$H(N_k) = \frac{1}{2} \log_2(2\pi e\sigma^2)$$

Since the noise is independent of the noiseless image, the conditional entropy of the noise at each pixel is the same, and the full conditional entropy (Equation 13) simplifies to:

$$H(\mathbf{Y} | \mathbf{x}^{(i)}) = \sum_{k=1}^D H(Y_k | x_k^{(i)}) \quad (14)$$

$$= \sum_{k=1}^D H(N_k) \quad (15)$$

$$= \frac{D}{2} \log_2(2\pi e\sigma^2) \quad (16)$$

Plugging this result into equations 9 and 7 yields:

$$H(\mathbf{Y} | \mathbf{X}) = \frac{D}{2} \log_2(2\pi e\sigma^2) \quad (17)$$

To summarize, the conditional entropy of the noisy image given the noiseless image is a constant, independent of the intensity values of the noiseless images, and is equal to the number of pixels in the image times the entropy of the noise distribution at each pixel.

### S2.3.2 Conditional entropy with shot noise

Images with high photon counts are limited in their signal-to-noise ratio by the inherently random arrival times of photons, due to the quantum nature of light. This noise is called shot noise, and it follows a Poisson distribution with rate parameter equal to the expected number of photons at that pixel [28]. As the rate parameter of a Poisson distribution increases, it

becomes more and more similar to a Gaussian distribution with equal mean and variance. In regimes in which shot noise is the dominant source of noise, this noise can thus be very accurately approximated with a Gaussian distribution with equal mean and variance [28]. Thus, the conditional entropy of the noise at pixel  $k$  for the  $i$ th noiseless image can be approximated as:

$$H(Y_k | x_k^{(i)}) = \frac{1}{2} \log_2(2\pi e x_k^{(i)}) \quad (18)$$

Once again making use of the fact that the measurement noise at each pixel is independent of the noise at other pixels conditional on the intensity of the noiseless image at that pixel (Section S2.3), we can write the conditional entropy for noiseless image  $\mathbf{x}^{(i)}$  as:

$$H(\mathbf{Y} | \mathbf{x}^{(i)}) = \sum_{k=1}^D H(Y_k | x_k^{(i)}) \quad (19)$$

$$= \sum_{k=1}^D \frac{1}{2} \log_2(2\pi e x_k^{(i)}) \quad (20)$$

The full conditional entropy (Equation 13) simplifies to:

$$H(\mathbf{Y} | \mathbf{X}) \approx \frac{1}{N} \sum_{i=1}^N \sum_{k=1}^D \frac{1}{2} \log_2(2\pi e x_k^{(i)}) \quad (21)$$

To summarize, the conditional entropy under a Poisson noise model can be approximated as a sum of the log of the intensity values of the noiseless image at each pixel, averaged over  $N$  noiseless images. This approximation is accurate when the photon counts are high, and breaks down when the photon counts are low, and is discussed further in Section S3.5.

## S2.4 Estimating Entropy of Noisy Images

The second, more challenging term to estimate in the decomposition of mutual information (Equation 6) is the entropy of the noisy images,  $H(\mathbf{Y})$ . It is challenging because unlike the conditional entropy estimates in Section S2.3, the relevant joint probability distribution  $p(\mathbf{y})$  cannot be factorized into a product of independent distributions for each pixel. That is, the pixels in a noisy measurement (like those of a noiseless image) are not independent of each other.

Our approach for computing this entropy is to compute an upper bound by fitting a probabilistic model to it, which empirically has been shown to be more accurate than other types of entropy bounds in high dimensions [35].

Specifically, we create a parametric model for the distribution of noisy images  $p_\theta(\mathbf{y})$ , where  $\theta$  are the parameters of our model. We estimate these parameters  $\theta$  by fitting the model to samples from the empirical distribution of noisy images  $p(\mathbf{y})$  using maximum likelihood

estimation. Mathematically, the maximum likelihood fit  $\hat{\theta}_{\text{MLE}}$  is found as the solution to the following optimization problem, which uses the negative log likelihood of the data as the objective function:

$$\hat{\theta}_{\text{MLE}} = \arg \min_{\theta} -\mathbb{E} [\log p_{\theta}(\mathbf{Y})] \quad (22)$$

This loss function,  $-\mathbb{E} [\log p_{\theta}(\mathbf{Y})]$ , is also known as the cross entropy between the model distribution  $p_{\theta}(\mathbf{y})$  and the empirical distribution  $p(\mathbf{y})$ .

In practice, it is fit using a dataset of  $N$  samples from the empirical distribution  $p(\mathbf{y})$ :

$$\hat{\theta} = \arg \min_{\theta} -\frac{1}{N} \sum_{i=1}^N \log p_{\theta}(\mathbf{y}^{(i)}) \quad (23)$$

When the model distribution  $p_{\theta}(\mathbf{y})$  is identical to the empirical distribution  $p(\mathbf{y})$ , the data has been fit perfectly, and the value of the cross entropy loss function is equal to the entropy of the noisy images,  $H(\mathbf{Y})$ .

$$-\mathbb{E} [\log p_{\theta}(\mathbf{Y})] = -\mathbb{E} [\log p(\mathbf{Y})] \quad (24)$$

$$= H(\mathbf{Y}) \quad (25)$$

In practice, the model will not be able to fit the true distribution exactly, and the average value of the loss function will be greater than the entropy of the noisy images. The gap between the entropy that we are interested in estimating and the cross-entropy loss function is given by the Kullback-Leibler divergence between the model distribution and the empirical distribution:

$$-\mathbb{E} [\log p_{\theta}(\mathbf{Y})] = H(\mathbf{Y}) + D_{KL}(p_{\theta} \parallel p) \quad (26)$$

The Kullback-Leibler divergence is a measure of the difference between two probability distributions. It is always non-negative and is zero only when the two distributions are identical. Thus, the cross-entropy loss function is an upper bound on the entropy of the noisy images. The better our model fits the data, the tighter this bound will be. Finding the right model that balances the accuracy of this bound with the computational cost of fitting the data is an important choice that is discussed further in **Section S3.2**.

In practice, the cross entropy loss function is evaluated on separate test set of samples from the empirical distribution, to avoid overfitting to a subset of the data and generating a model that is overly optimistic about its performance.

This process is mathematically equivalent to the problem of data compression in information theory<sup>5</sup>. In this problem, the goal is to compress data by mapping each outcome to

---

<sup>5</sup>Technically, this is only completely true when the model distribution is a discrete distribution, because continuous data cannot be losslessly compressed in a discrete setting. For example, it would take an infinite number of bits on a computer to represent an arbitrary real number exactly. But the intuition remains the same.

a string of bits, such that the total number of bits needed on average is as small as possible. The optimal compression scheme maps more probable outcomes to shorter bit strings, and less probable outcomes to longer bit strings. The efficiency with which this can be done is determined by how random the true distribution is (i.e. its entropy).

## S2.5 Probabilistic models

In this section, we describe two different probabilistic models  $p_\theta(\mathbf{y})$  that we will use to fit the empirical distribution of noisy measurements  $p(\mathbf{y})$ , and thus estimate via an upper bound the entropy of noisy measurements, as described in **Section S2.4**. The two models differ in their complexity, the tightness with which they upper bound the true entropy, and the computational resources and data needed to fit them.

The first model is based on a multivariate Gaussian distribution. It is simpler and faster to fit, but it is less flexible in its ability to fit the data, and thus provides a looser upper bound on the entropy of the noisy images.

The second model, a PixelCNN, is a type of model called an autoregressive model, and is based on a neural network. It is more complex and computationally expensive to fit in terms of time and data, but it is more flexible in its ability to fit the data and can thus provide a tighter upper bound on the entropy of the noisy images given sufficient resources.

There are many other possible models that could be used to fit the data using this general procedure. Any model for which the likelihood function can be directly evaluated can be used. There are several classes of such models based on neural networks that have been studied in recent years, including other types of auto-regressive models like transformers [73], normalizing flows [74], and energy-based models such as diffusion models [75, 76].

Notably, the perceptual quality of samples is not necessarily an indicator that it fits the data in terms of cross entropy loss [77], though state-of-the-art models in terms of perceptual quality of samples can be adapted to perform well for both [78]. We chose the PixelCNN model for its relative simplicity and computational efficiency and because it has been shown to produce good fits in terms of cross-entropy of test data [40]. However, it seems quite likely that there already is or will be a better model for this task. One that improves on our approach in terms of data and compute requirements and tightness of the upper bound on the entropy of the noisy images.

### S2.5.1 Stationary stochastic processes and entropy rate

In order to be able to quantify the performance over the full field of view of an imaging system by a single scalar quantity, we make a simplifying assumption that the noiseless image and the noisy image are stationary stochastic processes. This is the probabilistic analog of the assumption of a constant optical resolution across the field of view [18].

A stationary stochastic process with distribution  $p(\mathbf{y})$  is one in which the joint distribution of any set of pixels is invariant to translations across the field of view. Focusing on a 1D stationary process (i.e. a single row of pixels in an image) for simplicity, this means that the joint distribution of any set of pixels depends only on their relative locations in the image, not on their absolute locations. Mathematically, this means that for any vector of pixels  $(y_1, y_2, \dots, y_D)$  with joint distribution  $p(y_1, y_2, \dots, y_D)$ , the joint distribution of pixels

with the same relative locations but all offset by a constant amount  $y_{1+k}, y_{2+k}, \dots, y_{D+k}$  is the same:

$$p(y_1, y_2, \dots, y_D) = p(y_{1+k}, y_{2+k}, \dots, y_{D+k}) \quad (27)$$

Practically, this means that we can view cropped patches from different parts of the field of view as samples from the same distribution. This simplifies the model and reduces the number of parameters that need to be fit.

Stationary stochastic processes have the useful property that they have a constant entropy per pixel, called the entropy rate [59] (explained in Figure 8 of [60]). This entropy rate can be equivalently viewed as the limit of the joint entropy  $H(y_1, y_2, \dots, y_D)$  as the number of pixels  $D$  goes to infinity divided by  $D$ , or as the conditional entropy of the  $D$ th pixel given the previous  $D - 1$  pixels as  $D$  goes to infinity. Mathematically:

$$\lim_{D \rightarrow \infty} \frac{1}{D} H(y_1, y_2, \dots, y_D) = \lim_{D \rightarrow \infty} H(y_D | y_1, y_2, \dots, y_{D-1}) \quad (28)$$

This can be understood in practical terms by considering the conditional entropy of the  $D$ th pixel given the previous  $D - 1$  pixels, which quantifies how random the  $D$ th pixel is given the previous  $D - 1$  pixels. As  $D$  increases, we have seen more pixels of the image, and thus predicting the next pixel becomes easier, and the conditional entropy decreases. Essentially, it can be much easier to predict the value of a pixel in an image if you know the values of neighboring pixels.

Since in practice we will not have images with an infinite number of pixels, the models that we fit to the data will be finite length approximations of the true underlying stochastic process. In general, modeling more pixels at once will be able to fit more complex dependencies in the joint distribution, and thus provide a tighter upper bound on the entropy of the noisy images.

### S2.5.2 Stationary Gaussian Process

In the stationary Gaussian model, the true distribution of noisy images is approximated with a multivariate Gaussian distribution. A multivariate Gaussian distribution is a generalization of the univariate Gaussian distribution to multiple dimensions. It is fully specified by a mean vector  $\boldsymbol{\mu}$  and a covariance matrix  $\boldsymbol{\Sigma}$ . Its probability density function is given by:

$$p_{\theta}(\mathbf{y}) = \frac{1}{\sqrt{(2\pi)^D \det(\boldsymbol{\Sigma})}} \exp\left(-\frac{1}{2}(\mathbf{y} - \boldsymbol{\mu})^T \boldsymbol{\Sigma}^{-1}(\mathbf{y} - \boldsymbol{\mu})\right) \quad (29)$$

Compared to an arbitrary multivariate Gaussian process, the stationary Gaussian process has additional constraints on its mean vector and covariance matrix, which simplify the model by reducing the number of parameters that need to be fit. Mean vectors for non-stationary Gaussian processes can have arbitrary values, but for stationary Gaussian processes they must be constant vectors, reducing the number of parameters from the number of pixels  $D$  to just 1.

Covariance matrices for non-stationary Gaussian processes can be any symmetric, positive definite matrix. For stationary Gaussian processes, the covariance between any two pixels is only a function of their relative positions in the image, not their absolute positions. For a 1-Dimensional stationary Gaussian process (i.e. a single row of pixels in the image), the matrix must be a Toeplitz matrix: a matrix in which each descending diagonal from left to right is constant. For a 2-Dimensional stationary Gaussian process (i.e. the full image), the matrix is a doubly Toeplitz matrix: It is made up of submatrix blocks of Toeplitz matrices, and these blocks are themselves arranged in a Toeplitz pattern (**Fig. S8**). These symmetric Toeplitz/doubly Toeplitz matrices have only  $D$  parameters, since the full matrix can be constructed by repeating the values in the first column. This is less than the  $\frac{D(D+1)}{2}$  parameters needed to specify an arbitrary symmetric, positive definite matrix.

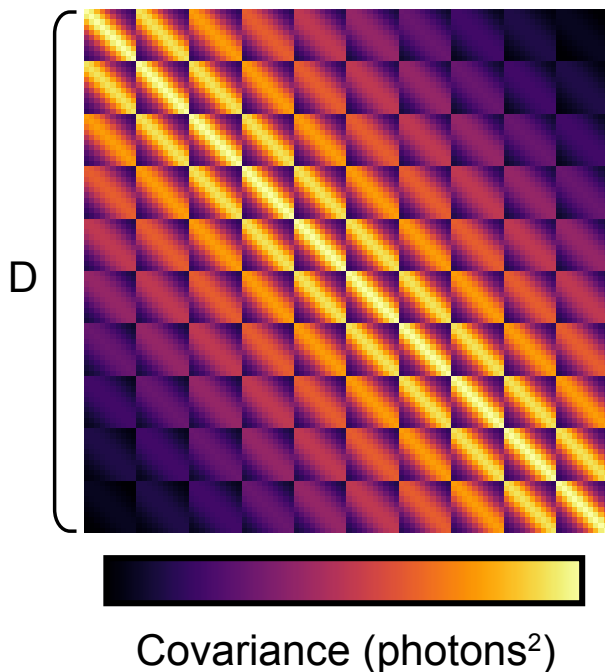


Figure S8: **The doubly Toeplitz  $D \times D$  covariance matrix of a stationary 2D Gaussian process.**

### S2.5.3 PixelCNN

The PixelCNN [38, 39, 40] is a type of autoregressive probabilistic model that uses neural networks to model complex dependencies between pixels.

Autoregressive models in general are a class of probabilistic models that factorize a joint distribution into a product of conditional distributions, and then model each of the conditional distributions. Mathematically:

$$p(\mathbf{y}) = \prod_{k=1}^D p(y_k \mid y_1, y_2, \dots, y_{k-1}) \quad (30)$$

$$= p(y_1)p(y_2 \mid y_1)p(y_3 \mid y_1, y_2) \dots p(y_M \mid y_1, y_2, \dots, y_{D-1}) \quad (31)$$

This factorization does not require specific assumptions about the joint distribution, so in theory it can be applied to any distribution.

Creating the full model thus requires creating  $D$  models for each of the conditional distributions. Each conditional distribution model takes between 1 and  $D - 1$  arguments, which are the values of the previous pixel of a particular image, and outputs a 1D probability distribution over the possible values of the next pixel.

While it is possible to implement this approach with  $D$  different models for each conditional distribution, the PixelCNN instead uses a specific type of convolutional neural network that enables all the conditionals to be modeled simultaneously, thus dramatically reducing computational complexity.

#### S2.5.4 Sampling and likelihood evaluation

The primary purpose of fitting probabilistic models to data is to be able to evaluate the likelihood of data under the model and compute an upper bound of the data distribution entropy, as described in **Section S2.4**. However, it is also useful to generate samples from the model, which can be used to visualize the model and qualitatively assess its fit to the data. The visual quality of samples and the likelihood of samples from the data distribution are correlated for simple models like the stationary Gaussian process, and thus inspecting quality of the samples can be a useful way to assess the quality of the model fit. However, this is not necessarily true for more complex models like the PixelCNN [77]. Nonetheless, in these cases it can still be useful to visualize samples to better understand its fit to the data.

Both the PixelCNN and the stationary Gaussian process models are trained on image patches of a fixed size  $\sqrt{D} \times \sqrt{D}$ . These models are thus incapable of capturing dependencies between pixels that are larger than this patch size. Increasing the patch size will give the models the ability to capture longer range dependencies, and thus more accurately fit the data.

However, despite the fixed patch size, since the models are both stationary, they can be used to evaluate likelihood and generate samples for images of arbitrary size, by iteratively sliding their fixed extent over a large area of an image (though these procedures are iterative and substantially slower than likelihood computation/sampling that is less than or equal to the model patch size). This is because both models can be autoregressively factored into a product of conditional distributions. Using a 1-dimensional model with  $D$  pixels for simplicity, this means that the joint distribution can be written as:

$$p(\mathbf{y}) = \prod_{k=1}^D p(y_k \mid y_1, y_2, \dots, y_{k-1}) \quad (32)$$

$$= p(y_1)p(y_2 \mid y_1)p(y_3 \mid y_1, y_2) \dots p(y_D \mid y_1, y_2, \dots, y_{D-1}) \quad (33)$$

Taking the log likelihood turns this product into a sum:

$$\log p(\mathbf{y}) = \sum_{k=1}^D \log p(y_k | y_1, y_2, \dots, y_{k-1}) \quad (34)$$

$$= \log p(y_1) + \log p(y_2 | y_1) + \log p(y_3 | y_1, y_2) + \dots + \log p(y_D | y_1, y_2, \dots, y_{D-1}) \quad (35)$$

Computing the likelihood over an image larger than the length  $D$  model the pixel was trained on can be accomplished by adding additional terms to this sum. For example, computing the log likelihood of an  $D + 1$  length image would require adding an additional term to the sum of the log likelihood of the the  $D + 1$  pixel conditioned on the previous  $D - 1$  pixels (the maximum extent of the model) that preceded it:

$$\log p(\mathbf{y}) = \left( \sum_{k=1}^D \log p(y_k | y_1, y_2, \dots, y_{k-1}) \right) + \log p(y_{D+1} | y_2, y_3, \dots, y_D) \quad (36)$$

Details of the likelihood computations for PixelCNNs are described in [38]. For stationary Gaussian processes, there is a closed form solution for finding the mean  $\mu_D$  and variance  $\sigma_D^2$  of a 1-dimensional Gaussian distribution conditioned on  $D - 1$  previous values. This involves decomposing the covariance matrix into a top left  $(D - 1) \times (D - 1)$  block  $\Sigma_{1,1}$ , a top right  $(D - 1) \times 1$  column vector  $\Sigma_{1,2}$ , and a bottom left  $1 \times (D - 1)$  row vector  $\Sigma_{2,1}$ :

$$\Sigma = \begin{bmatrix} \Sigma_{1,1} & \Sigma_{1,2} \\ \Sigma_{2,1} & \sigma_M^2 \end{bmatrix} \quad (37)$$

Given  $D - 1$  previous values  $\mathbf{y}_{D-1}$ , the mean and variance of the  $D$ th value can be computed as:

$$\mu_D = \mu + \Sigma_{2,1} \Sigma_{1,1}^{-1} (\mathbf{y}_{D-1} - \mu) \quad (38)$$

$$\sigma_D^2 = \sigma^2 - \Sigma_{2,1} \Sigma_{1,1}^{-1} \Sigma_{1,2} \quad (39)$$

The likelihood the the  $D$ th pixel can then be evaluated using the probability density function of a 1D Gaussian distribution with mean  $\mu_D$  and variance  $\sigma_D^2$ .

Similarly, sampling images larger than the patch size on which the models were trained can be accomplished by iteratively sampling each pixel conditioned on the previous  $D - 1$  pixels.

## S2.6 Accounting for encoder uncertainty

As described in **Section S1.4.1**, measurements often contain information about both the object and the system itself. To avoid overestimating object information, the strategy for estimating mutual information must be modified.

Specifically, instead of estimating the full entropy of noisy measurements  $H(\mathbf{Y})$ , the conditional entropy  $H(\mathbf{Y}|\mathbf{E})$  should be estimated. The conditional entropy estimate  $H(\mathbf{Y}|\mathbf{X})$  is unaffected. But  $H(\mathbf{Y})$  now includes randomness from the object, system variations, and noise. Conditioning on the encoder state  $\mathbf{E}$  eliminates the contribution of system variations, leaving only object and noise entropy.

In practice, conditioning can be accomplished by providing additional encoder state information like field position or calibration images to the entropy model during training. Flexible models like PixelCNN can readily accept such conditional data [39]. This reduces the entropy estimate by eliminating variations predictable from the system state. We leave developing such conditional entropy estimation to future work.

## S3 Estimating information—Experiments

Having described the theoretical background of information estimation, we now turn to experiments on simulated and experimental data to validate its performance. For both methods of entropy estimation described below, we treat noiseless images and noisy measurements as stationary stochastic processes, as described in Section S2.5.1. The training data used to optimize the models described below are thus cropped patches from random locations in the images, since patches from any location should be statistically identical under such a model. When simulating data, we can ensure that images are in fact stationary by generating them from shift invariant probability distributions. Experimental data does not have this property in reality, so the estimates produced should be regarded as an average over spatially varying information rates.

### S3.1 Probabilistic models for entropy estimation

#### S3.1.1 Fitting stationary Gaussian processes

Fitting a stationary Gaussian process to a dataset of  $N \sqrt{D} \times \sqrt{D}$  image patches consists of using the image patches to estimate the mean vector  $\boldsymbol{\mu}$  and covariance matrix  $\boldsymbol{\Sigma}$  of the model. The mean vector can be easily estimated by taking the mean of all pixels in the dataset across all patches.

The covariance matrix of a stationary Gaussian process has a special structure: it is symmetric and positive definite (like every covariance matrix), as well as being doubly Toeplitz (Section S2.5.2). This means that it is composed of blocks of submatrices with constant diagonals, and the blocks themselves are arranged in a repeated pattern along the diagonals.

Our initial estimator for the covariance matrix consisted of taking the set of image patches, vectorizing them, computing the covariance matrix of the sample, and then averaging along the diagonals and blocks to enforce this special structure. However, this procedure is not guaranteed to produce a covariance matrix that is positive definite, and we found empirically that the averaging operation led the resulting estimate to have negative eigenvalues, making an invalid covariance matrix.

To address this, we then regularized the estimates by enforcing an eigenvalue floor, a minimum small, positive value for the eigenvalues. This was insufficient for two reasons. 1) Modifying the eigenvalues in practice tended to then break the doubly Toeplitz structure of

the matrix, making it slightly violate the requirements of a stationary Gaussian process. 2) More importantly, the purpose of fitting this model was to be able to evaluate the likelihood of data under the model to upper bound entropy, and this likelihood is highly sensitive to the small eigenvalues of the covariance matrix. Thus, the heuristic choice of eigenvalue floor has a significant impact on the estimated entropy upper bound, and that effect varied from dataset to dataset.

To address these limitations, we developed an iterative optimization procedure to improve the fit of the covariance matrix to the data. Using a dataset of  $N \sqrt{D} \times \sqrt{D}$  image patches vectorized into  $N D$  length vectors  $\mathbf{y}^{(1)}, \mathbf{y}^{(2)}, \dots, \mathbf{y}^{(N)}$ , we solve the following optimization problem to minimize the negative log likelihood of a multivariate Gaussian distribution  $\mathcal{N}(\cdot; \hat{\boldsymbol{\mu}}, \boldsymbol{\Sigma})$ :

$$\hat{\boldsymbol{\Sigma}} = \arg \min_{\boldsymbol{\Sigma}} - \sum_{i=1}^N \log \mathcal{N}(\mathbf{y}^{(i)}; \hat{\boldsymbol{\mu}}, \boldsymbol{\Sigma}) \quad (40)$$

Where  $\hat{\boldsymbol{\mu}}$  is the fixed mean vector estimated from the data as described above.

We solved this optimization problem using proximal gradient descent with momentum. At each step, we computed the eigendecomposition of the covariance matrix, fixed the eigenvectors, and computed and applied the gradient to the eigenvalues. After each gradient step, a proximal operator was applied that averaged along diagonals and blocks as described above, and then enforced a minimum eigenvalue floor. The procedure was regularized using early stopping, in which the optimization was stopped when the loss had not decreased for a fixed number of iterations, and the parameters from the iteration with the lowest loss were used as the final estimate. The parameters were initialized with the estimate directly computed from the data as described above.

Empirically, we found that the optimization procedure was unstable and prone to divergence. This seemed to be because the likelihood was very sensitive to small eigenvalues of the covariance, which tended to produce extremely large gradients for these eigenvalues. To account for this, we implemented gradient clipping to limit the magnitude of the gradients for the eigenvalues.

The likelihood of a probability distribution can be very sensitive to small changes in parameters because the Euclidean distance between parameter vectors does not always accurately reflect the dissimilarity of the resulting distributions (as described in section 2.3 of [79]). In theory this can be corrected by multiplying the gradient by the inverse of the Fisher information matrix to reorient it from the steepest direction in Euclidean space to the steepest direction in Riemannian space, which accounts for the natural geometry of the parameters. However, in practice we found this to be expensive to compute without obvious performance benefits over gradient clipping.

**Figure S9** shows the results when fitting stationary Gaussian processes to images from the BSCCM dataset [43]. The direct estimate contained several negative eigenvalues, which were then set to an arbitrary eigenvalue floor. The optimization procedure was able to correct these negative eigenvalues, and produced robust results for a variety of settings of the eigenvalue floor parameter (provided it was smaller than the true minimum eigenvalue) (**Fig. S9b**). As a consequence of the small, incorrect eigenvalues in the direct estimate, samples

produced from the model that were larger than the patch size on which they were trained (Sec. S2.5.4) exhibited numerical instability that created large oscillation in the samples. In contrast, samples from the optimized model were stable and did not exhibit this oscillation (Fig. S9b). The optimization quickly converged in a few iterations (Fig. S9c), taking  $\sim 3$  seconds to complete on an NVIDIA GeForce RTX 3090 GPU. Comparing estimates of a non-stationary Gaussian process, the direct estimate stationary Gaussian process, and the optimized stationary Gaussian process showed that the optimized stationary Gaussian process produced more robust results in terms of its eigenvalue distribution using smaller datasets (Fig. S9d).

### S3.1.2 Fitting PixelCNNs

PixelCNNs were constructed and optimized as described previously [38, 39]. Briefly, the architecture consists of a series of masked convolutions, to ensure an autoregressive ordering to pixels, with a final output layer that outputs a conditional probability distribution at each pixel. This distributions can be used both to iteratively generate samples, and to evaluate the likelihood of data under the model.

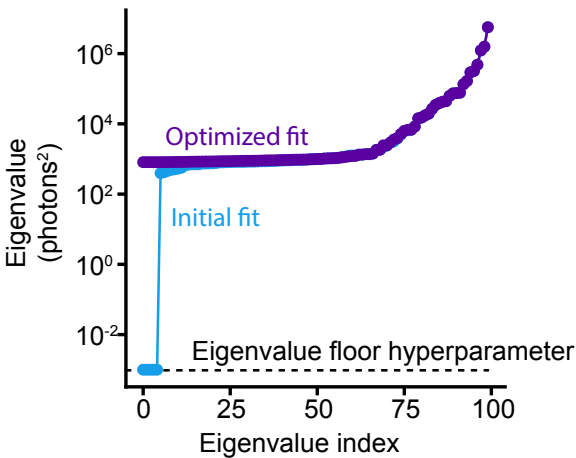
We made one important modification to the standard PixelCNN architecture. Rather than using a softmax layer as the final output for the conditional distribution at each pixel, we use a mixture of Gaussians parameterized by the output of the network (also known as a mixture density network [80]). This strategy is capable in theory of approximating any conditional probability distribution, in the same way that a neural network is capable of approximating any function [81]. This modification is essential for estimating entropy in our framework, because it means the output distributions will be a continuous probability density, instead of discrete probability mass functions. In order to subtract the conditional entropy  $H(\mathbf{Y} | \mathbf{X})$  from the entropy estimate of  $H(\mathbf{Y})$  made by the PixelCNN, it is essential that these are either both discrete entropies (i.e. based on a probability mass function) or continuous entropies (based on a probability density function). Since the optical noise models  $p(\mathbf{y} | \mathbf{x})$  we employ are continuous (e.g. Gaussian distributions), the entropy estimates for  $H(\mathbf{Y})$  must also be continuous.

## S3.2 Comparing Stationary Gaussian Process and PixelCNN estimates

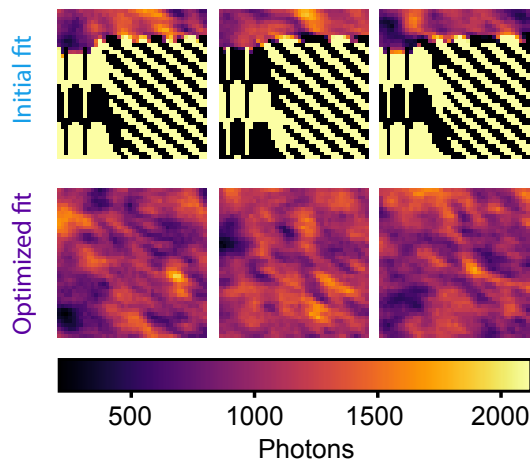
The fit of PixelCNN and Gaussian process models was compared by evaluating the negative log likelihood on held out test data, and by visualizing samples from the models. An important consideration for fitting either model to data is the size of image patches used in the training set. Larger patches allow the model to capture longer range dependencies and thus fit the data better in terms of per pixel negative log likelihood. However, this comes at the cost of greater data requirements and computational resources to train. Thus we sought to find the largest patch size that produced a sufficient fit to the data to form an accurate estimate of entropy.

**Figure S10** shows samples produced when fitting models to patches of different sizes. As expected, larger patch sizes were able to capture more complex statistical relationships between pixels (Fig. S10a), decrease the per pixel loss (Fig. S10b), and more tightly

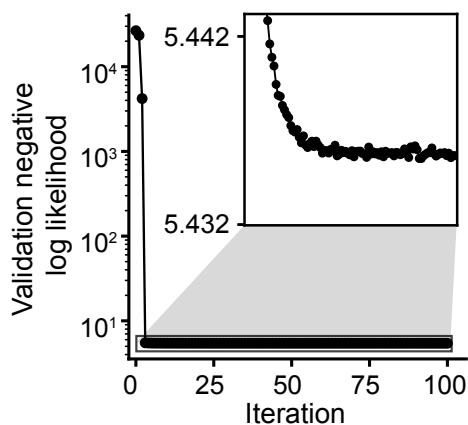
**a) Optimization improves covariance matrix conditioning**



**b) Improved conditioning prevents numerical instability when sampling**



**c) Optimization progression**



**d) Optimizing gives better fit with less data**

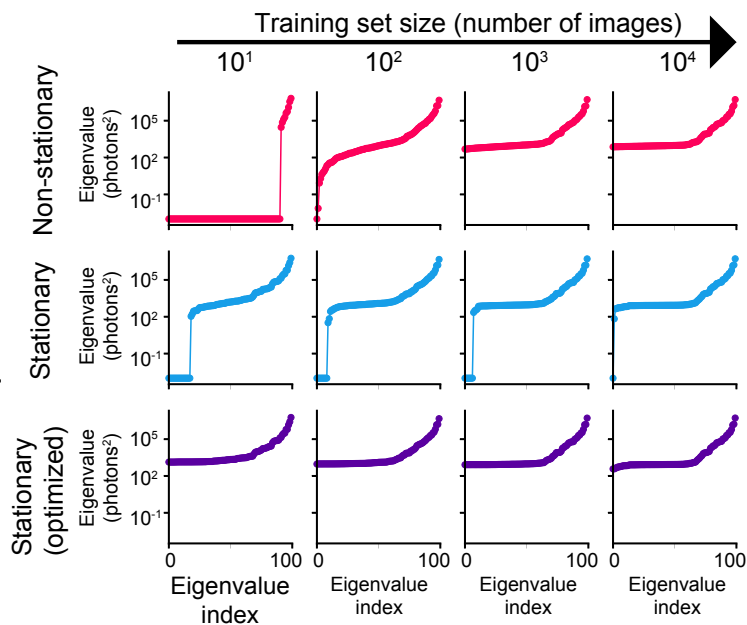


Figure S9: **Fitting Gaussian Process models.** **a)** Eigenvalues of the covariance matrix before and after optimization, indicating improved conditioning post-optimization. The conditioning of the covariance matrix of non-optimized fits is highly dependent on the choice of the eigenvalue floor hyperparameter. **b)** Comparison of numerical stability during sampling pre- and post-optimization, demonstrating that optimization prevents the instability that manifests in the initial fit. **c)** The optimization process takes only a few iterations to converge and shows an extremely large improvement in the negative log likelihood of the data for poor initial fits. **d)** Efficacy of the optimization across varying training set sizes, illustrating that optimized fitting requires fewer images to achieve a comparable or better fit than the non-optimized approach.

upper bound the entropy of the noisy images (**Fig. S10c**). The gains in performance were minimal beyond a patch size of  $35 \times 35$  pixels for the Gaussian model, while the PixelCNN was able to continue to produce a more accurate estimate as patch size increased further. This is presumably due to its much greater flexibility in modeling complex dependencies between pixels. However, the magnitude of the gains was small relative to the differences between the estimates of mutual information for different contrast modalities (**Fig. S11**) for these experimental images.

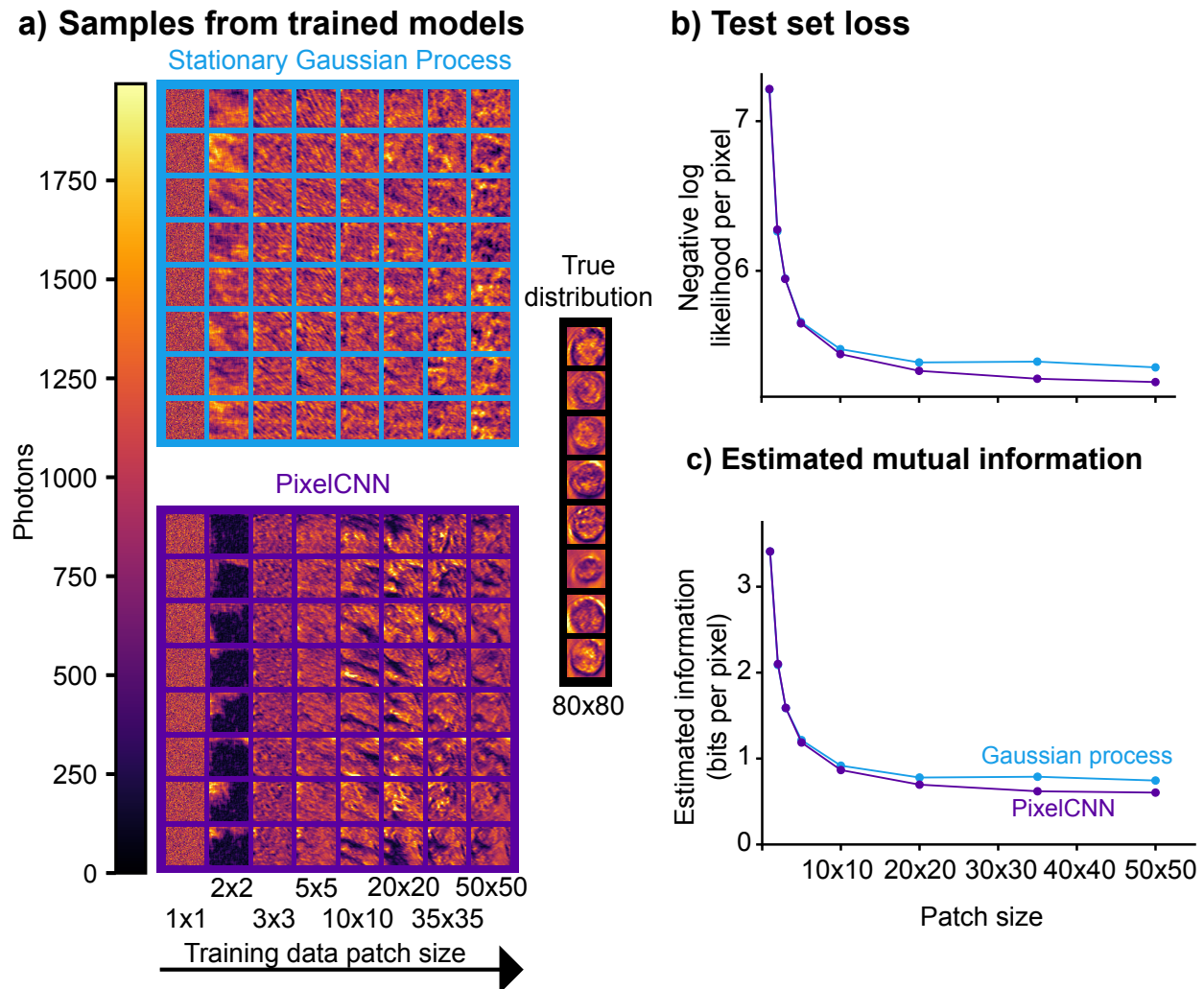


Figure S10: **The effects of patch size on model fit.** a) Samples generated from a Stationary Gaussian Process and PixelCNN, alongside samples from the the true distribution. As the patch size increases, the models are able to capture more long range dependencies between pixels, and b) achieve lower negative log likelihood per pixel and thus c) a tighter upper bound on mutual information.

When comparing the samples produced by the two models when fit to images with different illumination patterns on the LED array, both the Gaussian process and PixelCNN

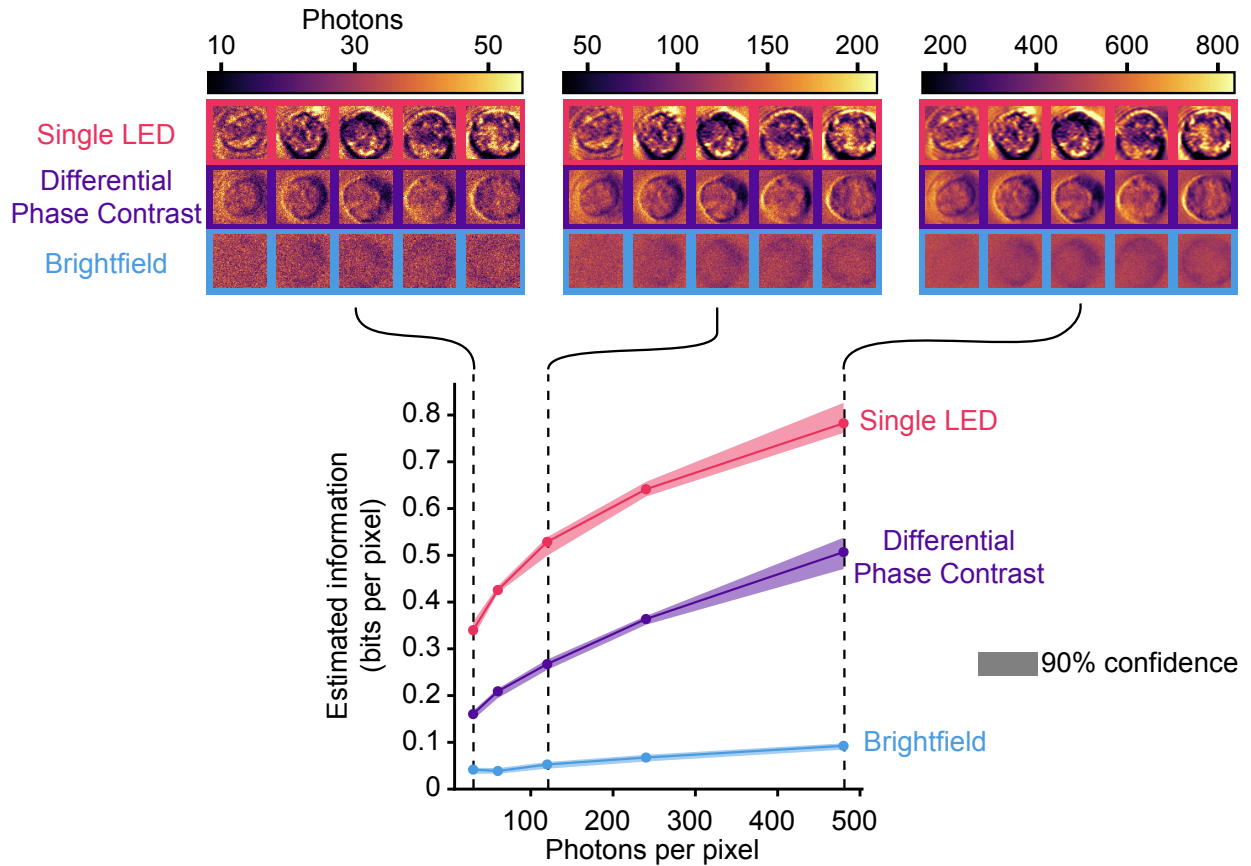


Figure S11: **Mutual information and photon count.** As the average number of photons per pixel increases, the signal-to-noise ratio and mutual information both increase. (Top) Example images of three different contrast modalities at varying photon counts. (Bottom) The mutual information per pixel for each contrast modality as a function of photon count.

models were able to capture statistical patterns to each type of contrast modality (**Fig. S12a**). Samples from the trained models appear to show that the Gaussian model was able to learn the statistical patterns of the texture of the images of objects under different illumination, while the PixelCNN model additionally learned higher order structures like the edges of cells.

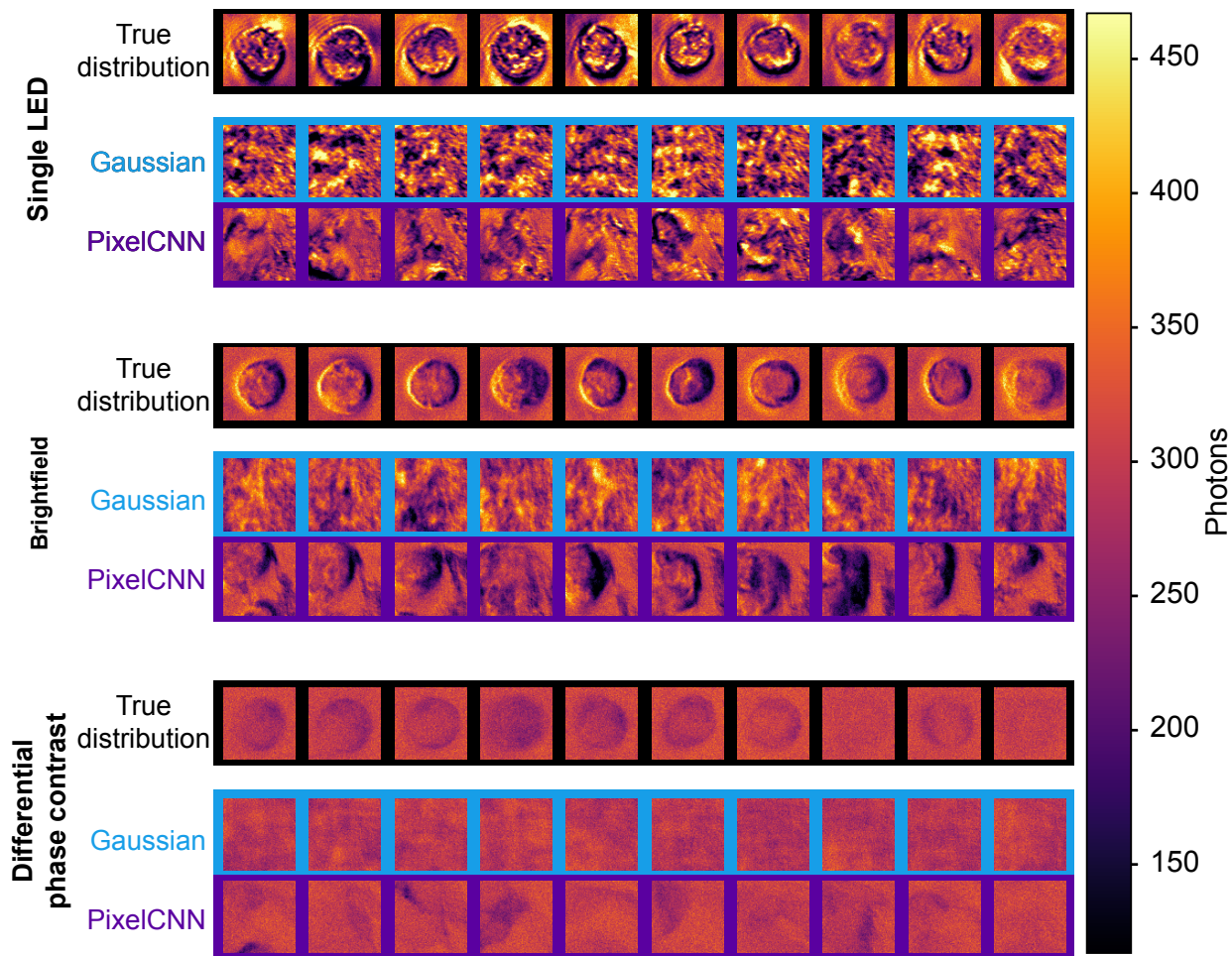


Figure S12: **Model samples for different contrast modalities.** Samples from the stationary Gaussian process and PixelCNN models for Brightfield, Differential phase contrast, and Single LED illumination.

### S3.3 Failures of stationary Gaussian estimates on highly non-Gaussian data

The similar performance between the stationary Gaussian process and PixelCNN models on the BSCCM dataset of single cells taken with coded-angle illumination is likely due to the fact that the data is relatively close to a multivariate Gaussian distribution, which is not something that can be assumed to be true for all types of data. An extreme example of

this can be seen by comparing mutual information estimates using the MNIST handwritten digits dataset as the object [82].

To demonstrate this, we take the MNIST dataset and simulate a minimal optical encoder (i.e. a single lens) by convolving the images with a Gaussian point spread function. We then add Poisson noise to simulate noisy measurements, and fit both the stationary Gaussian process and PixelCNN models to the data. Sampling from the fitted models shows that the PixelCNN model can produce images that appear similar to true measurements, unlike the Gaussian process model (**Fig. S13a**).

This occurs because the best approximating Gaussian fit is very dissimilar to the true distribution of the measurements. This can be seen by looking at the histograms of image pixels of the true data and samples from the models, pooled across all many images (**Fig. S13b**). The true data and PixelCNN samples have similar histograms, while the histogram from the Gaussian process samples has a very different shape. As a result of this poor fit, the upper bound given by the mutual information estimator is quite loose for the stationary Gaussian model compared to the PixelCNN model (**Fig. S13c**).

These findings demonstrate that a stationary Gaussian process model is inadequate to capture certain image distributions. Since the tightness of the upper bound in our information estimation procedure depends on accurately fitting the distribution of noisy measurements, this suggests that achieving a tight upper bound/accurate estimate in many cases may require more flexible probabilistic models, like the PixelCNN.

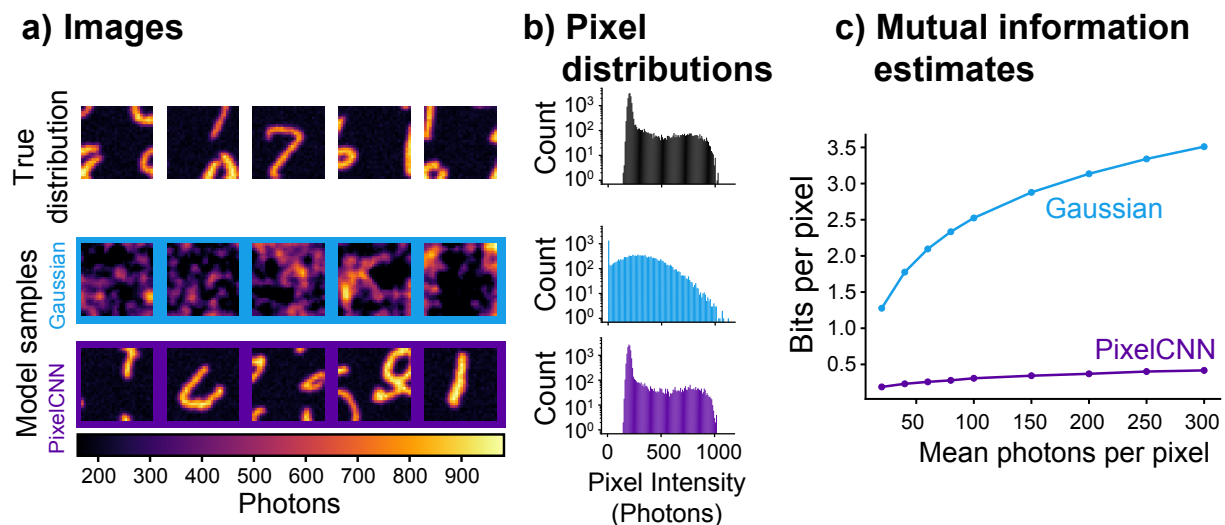


Figure S13: **PixelCNN can fit non-Gaussian data better than stationary Gaussian processes.** **a)** Samples from the stationary Gaussian process and PixelCNN models for MNIST digits. The Gaussian process samples do not resemble the true distribution, indicating a poor fit. **b)** Histograms of pixel values for the true distributions and samples from the two models indicate that the marginal distribution of pixels is non-Gaussian, which the PixelCNN, unlike the Gaussian model, is able to fit. **c)** As a result of the poor fit, the upper bound on mutual information given by the Gaussian process estimator is much looser than the PixelCNN estimator.

### S3.4 Consistency of mutual information estimates

An important and desirable property of an estimator is its consistency: whether it converges to the true value of the parameter being estimated given enough data. This is also an important practical consideration for using estimators, because it determines how much data is needed to achieve a desired level of accuracy.

In order to evaluate the accuracy of the estimators on high-dimensional data, we must first generate samples from an image distribution with known mutual information. This can be accomplished using a multivariate Gaussian distribution with independent additive Gaussian noise at each pixel 17. In this scenario,  $H(\mathbf{Y} | \mathbf{X})$  is simply a constant, and  $H(\mathbf{Y})$  can be computed analytically by taking the covariance matrix of the noiseless data and adding the variance of the noise to its diagonal, and analytically computing the entropy of the resulting multivariate Gaussian distribution.

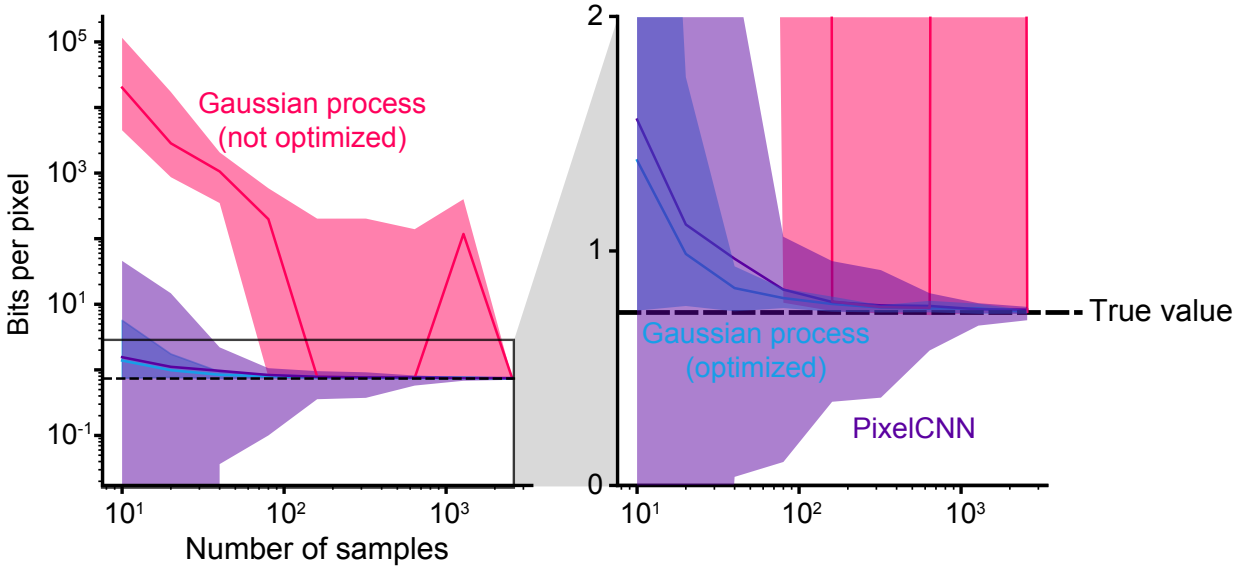
We started by estimating a stationary Gaussian process from real data filtered with a 3x3 median filter to use as the ground truth distribution of noiseless images. We then estimated the mutual information of noisy samples from this distribution using the PixelCNN, stationary Gaussian estimator, and a non-stationary multi-variate Gaussian estimate (found by directly using the covariance matrix of the samples) (**Fig. S14a**). All three estimators were able to accurately estimate the mutual information of the data given enough samples. The stationary Gaussian process estimator was the most efficient at this, showing the lowest variance in its estimate of mutual information for a given number of samples. The full Gaussian process estimator was the least efficient, due to its sensitivity to the eigenvalue floor hyperparameter described in (40).

These results are unsurprising, given that the stationary Gaussian process is the least flexible class of models and the data itself was generated from a stationary Gaussian process. To evaluate a more realistic scenario where data is not perfectly Gaussian, we repeated the same experiment on cell images under single LED illumination (**Fig. S14b**). In this scenario, the stationary Gaussian estimator showed lower variance, more accurate estimates for smaller amounts of data, but was less accurate than the PixelCNN estimator for larger amounts of data. Despite not knowing the ground truth value of mutual information in this scenario, since our estimator is an upper bound, we know that lower estimates are more accurate. The full Gaussian estimator was the least accurate in this scenario. Once again these results are unsurprising: real data is not Gaussian, and flexible, neural network models like the PixelCNN are able to produce more accurate results given enough data and computational resources.

### S3.5 Conditional entropy estimates on noisy data

The accuracy of the mutual information estimate depends on the accuracy of the separate estimates of its two components:  $H(\mathbf{Y})$  and  $H(\mathbf{Y} | \mathbf{X})$ . To better understand which estimate limits the accuracy of the mutual information estimator, we examined the consistency of the conditional entropy estimator  $H(\mathbf{Y} | \mathbf{X})$  on simulated data. When the noise model is additive Gaussian noise, the conditional entropy is independent of the noiseless images, and thus can be computed analytically exactly (**Sec. S2.3.1**). We thus focus on the more challenging scenario of signal-dependent Poisson noise (**Sec. S2.3.2**).

**a) Mutual information estimates vs. dataset size (Gaussian data)**



**b) Mutual information estimates vs. dataset size (Real data)**

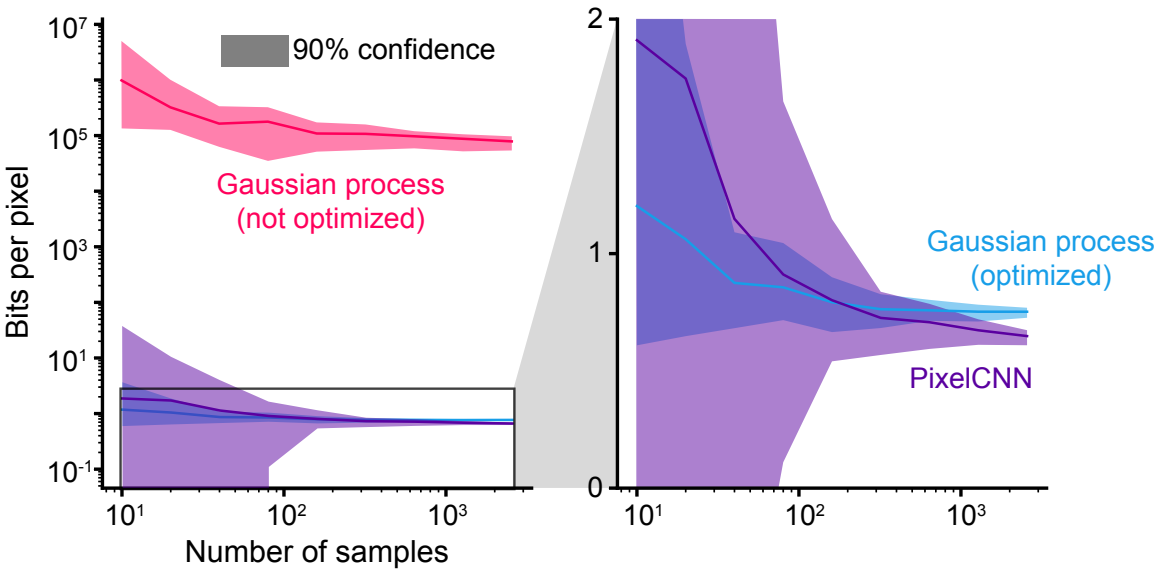


Figure S14: **Estimator consistency.** **a)** Estimating mutual information on simulated data consisting of samples from a stationary Gaussian process. With an increasing number of samples, all three estimators converge to the true value of mutual information, with the stationary Gaussian estimator producing the most reliable estimates for a given amount of data. **b)** When estimating on non-Gaussian data, the stationary Gaussian process has less variation in its estimates for a given amount of data, but cannot perfectly fit the non-Gaussian data, as seen from the fact that it converges to a looser upper bound than the PixelCNN estimator.

Once again using images of cells from the BSCCM dataset, we filtered the images with a  $3 \times 3$  median filter to produce simulated noiseless images and then added simulated shot noise to the noiseless images to produce noisy images for which the ground truth conditional entropy could be computed analytically. We then compared our estimates of the conditional entropy to this ground truth value as a function of the number of images used to estimate it (**Fig. S15a**). Our conditional entropy rapidly converged to the true value, with variations in its estimate on the order of  $10^{-2}$  differential entropy per pixel, even when the estimate was made from a single image patch. These variations were 1 – 2 orders of magnitude smaller than the variations seen in the estimation of  $H(\mathbf{Y})$  and the differences between different encoders, leading us to conclude that the conditional entropy estimation was an insignificant source of error in our information estimates.

Our approach for estimating conditional entropy relies on a Monte Carlo approximation using samples from the distribution of clean images (Equation 9). However, when applying the mutual information estimator to experimental data, noiseless images are not available. Thus we must resort to an approximation in which we estimate this quantity from samples from the distribution of noisy measurements instead. This may introduce some error into the estimator, and it is important to understand how much and what effect this error will have on the final estimate of mutual information.

In the case of additive Gaussian noise (**Sec. S2.3.1**), the conditional entropy is independent of the noiseless images, and thus there is no additional error. However, in the case of shot noise (**Sec. 18**), the conditional entropy is dependent on the noiseless images, and thus the approximation will introduce some error. Mathematically, our approach to estimating conditional entropy is to replace the noiseless pixel values in **Equation 21** with noisy pixel values:

$$H(\mathbf{Y} | \mathbf{X}) \approx \frac{1}{N} \sum_{i=1}^N \sum_{k=1}^D \frac{1}{2} \log_2(2\pi e x_k^{(i)}) \quad (41)$$

$$\approx \frac{1}{N} \sum_{i=1}^N \sum_{k=1}^D \frac{1}{2} \log_2(2\pi e y_k^{(i)}) \quad (42)$$

To test this we generated simulated noiseless images by applying a  $3 \times 3$  median filter to images from the BSCCM dataset and generated simulated noisy images by adding Poisson noise to these. We then estimated mutual information for different contrast modalities and photon counts, either using the true noiseless images or the simulated noisy images to estimate the conditional entropy. We found that the error introduced by using the noisy images was small relative to the differences between the estimates of mutual information for different contrast modalities (**Fig. S15b**), with appreciable differences only occurring at photon counts below  $\sim 40$  photons per pixel. Furthermore, the errors introduced a consistent bias in the estimates, giving overestimates of mutual information due to underestimates of the conditional entropy. Given the predictable nature of this bias, it could be possible to explicitly introduce a correction factor to the estimator to account for it. However, given that other assumptions of our estimator, like the Gaussian approximation to Poisson noise (**Sec. S2.3.2**), are also not valid in this regime, we leave this for future work and instead focus on the higher photon count regime where our estimator is more accurate.

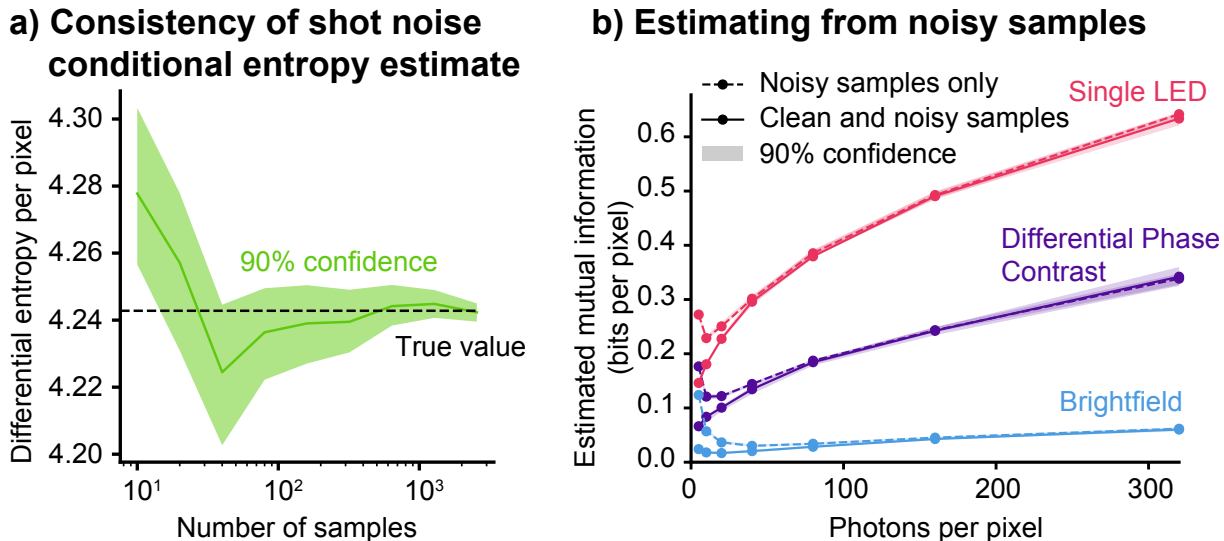


Figure S15: **Estimating conditional entropy.** a) The estimate of conditional entropy for shot noise quickly converges to the true value as the number of samples increases, showing much smaller variations than the entropy estimators considered in Figure S14. b) When noisy experimental images are used to estimate conditional entropy instead of ground truth noiseless images, the error introduced is small relative to the differences between the estimates of mutual information for different contrast modalities, and only deviates from the true value at low photon counts.

### S3.6 Analytic Gaussian entropy vs. upper bound

In addition to estimating entropy by upper-bounding it using the test set negative log likelihood, an alternative is to fit a probabilistic model to the data, and then analytically compute the entropy of the model. Though this is not possible for all models, it is possible for the stationary Gaussian process model, since the entropy of a multivariate Gaussian distribution can be computed analytically. It is unclear what the theoretical relationship between this analytic estimate and the true entropy is, unlike the test set negative log likelihood method, which upper bounds the true entropy.

We tested this approach empirically and compared it to the upper bound entropy estimates produced by the PixelCNN and stationary Gaussian process models on three different contrast modalities of the BSCCM dataset (**Fig. S16**). In this experiment, the values for the analytic stationary Gaussian entropy estimator were slightly lower than those of the stationary Gaussian upper bound, while being slightly higher than the PixelCNN upper bound estimates. Since we know the true entropy is lower than the PixelCNN upper bound, this suggests that the analytic Gaussian entropy is more accurate than the Gaussian upper bound estimator. However, these differences were small in comparison to the differences between the estimates of mutual information for different contrast modalities and different photon counts. The similarity between the analytic Gaussian entropy and the upper bound Gaussian entropy is advantageous, as we employ the analytic Gaussian entropy in our IDEAL (**Sec. 1.4**) loss function, and its close agreement with the upper bound estimator supports its validity.

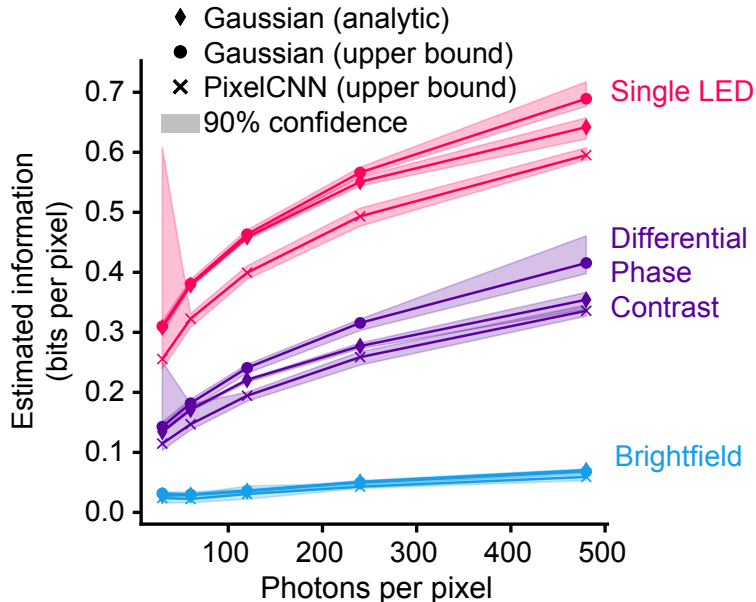


Figure S16: **Analytic Gaussian entropy vs. upper bound.** The analytic Gaussian entropy estimator produces slightly different estimates than the upper bound estimator for the stationary Gaussian process, but these differences are small relative to the differences between the estimates of mutual information for different contrast modalities and different photon counts.

## S4 Additional decoder experiments

### Estimating encoder uncertainty for LED array microscope

**A low information task** Unlike the deconvolution decoder (**Fig. 3b**), a more specialized task, an object classification decoder (**Fig. S18**), fails to show a monotonic relationship between information and decoder performance. For a given level of information, although there is a positive relationship with mutual information and decoder performance, the performance still varies among encoders.

We hypothesize this result is because classification utilizes only a small subset of the total information, the subset which is relevant to discriminating between classes. Most measured information corresponds to within-class variation, which is irrelevant to this discrimination between classes. Thus the specific useful features vary by encoder, explaining performance differences at equal information. In contrast, deconvolution is a more general, complicated task, for which within-class variation is necessary for accurate image reconstruction. Therefore more of the measured information is relevant to the deconvolution decoder.

A 10-class object classification problem such as this can have no more than  $\log_2 10 \approx 3.32$  bits of information relevant to it, while the  $32 \times 32$  sized images with 0.3 bits per pixel has  $\approx 307$  total bits.

For specialized tasks, future work could condition the mutual information estimator on specific dataset properties, such as object class, to estimate the task-specific mutual infor-

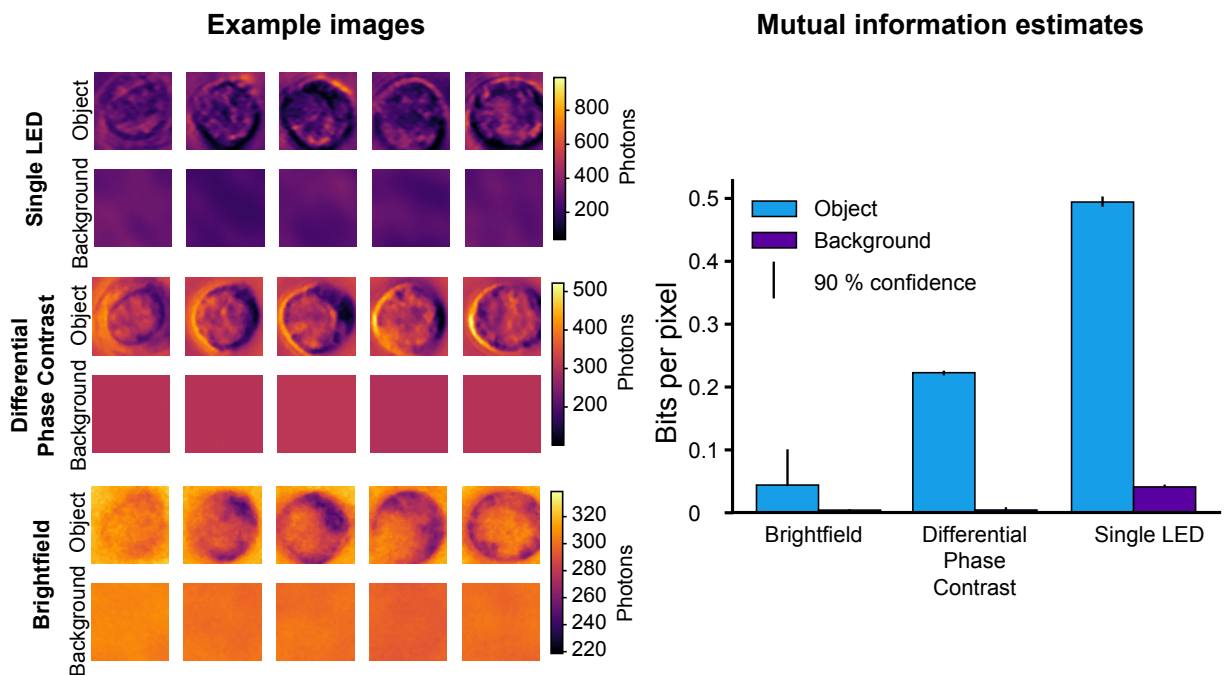


Figure S17: **The effect of encoder uncertainty on information estimates.** By computing mutual information estimates on empty image patches with no objects in them, the information about the system present in the measurements can be estimated. This can be seen by comparing Single LED, Differential Phase Contrast, and Brightfield illumination patterns on an LED array microscope, and estimating the mutual information between noiseless image and noisy measurement with and without an object. Encoders that capture more information about the object also capture more information about the system.

mation instead of the overall mutual information.

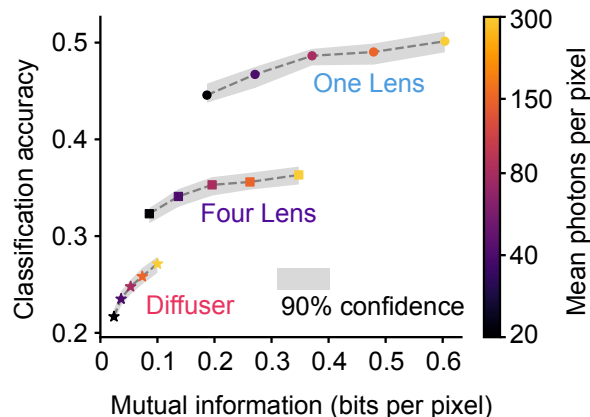


Figure S18: **Object classification vs. mutual information.** For a simple task such as 10-class object classification, the monotonic relationship between information and task performance does not hold (i.e. different encoders can achieve very different accuracy even with the same amount of information). Compare to **Figure 3b**, which uses the same measurements but a much more complicated, general task.

## S5 Other design strategies

Two related approaches for designing encoders arise from the estimation theoretic [83] methods that utilize the Cramér-Rao lower bound [84, 85] and compressed sensing theory [86].

Both approaches take a deductive approach: they make assumptions about objects, encoders, and decoders, and prove performance guarantees and theoretical limits of performance under those assumptions. This restricts their scope, tying guarantees to specific object classes, image formation models, and decoders.

Even when the assumptions are thought to match reality, this is often difficult or impossible to verify, precluding guaranteed applicability of theoretical results. Furthermore, the theoretical results often focus on guarantees in best or worst case scenarios for a single object, and do not always provide useful guidance in practical, average case situations.

Our framework can also be used deductively, making specific assumptions about objects and encoders, and deriving closed form expressions for information, as we did in the 2-point resolution example (**Sec. 1.1.1**).

In addition our framework has the unique advantage that it can also be applied inductively, drawing conclusions about the system from data. The information content can be estimated empirically from data to elucidate patterns in the constraints on information capture, without requiring an explicit model of the full imaging system or a specific decoder. The only model we have relied on in our results is a basic analytic noise model. However, even this noise distribution could be learned directly from data rather than imposing an assumed functional form.

By analyzing empirical data directly, our framework facilitates comparing across modalities, discerning subtle trends and tradeoffs hidden from theory, and illuminating complex interdependencies between encoder physics, objects, and decoding potential. Thereby, harnessing the flexibility of data-driven inference positions information estimation to broadly demystify and enhance imaging systems.

Detailed comparisons and connections between our approach and estimation theoretic and compressed sensing-based design are discussed in **Sections S6** and **S7**.

## S6 Comparison to design using Cramér-Rao lower bound

One approach to designing encoders utilizes a concept from estimation theory called the Cramér-Rao lower bound [83], which defines the minimal decoding mean squared error achievable for a given encoder and noise model. This facilitates comparing and optimizing encoders by selecting ones with the lowest possible error.

**Comparison with information encoding framework** While estimation theory and our information encoding framework share the goal of uncertainty reduction (**Sec. S6.4**), our framework has key advantages in generalizability.

Theoretical results in simplified scenarios suggest that the estimation theoretic approach and the information encoding formalism share the goal of reducing uncertainty in the presence of noise. However, our framework is far more generalizable owing to some key differences:

- It can be applied inductively from data, implicitly capturing all system intricacies without needing to model them.
- It does not require an explicit parameterized system model parameterized in terms of the task. For example, localizing a point emitter requires modeling the full imaging process as a function of position. Many tasks lack tractable models.
- It only assumes a noise model (which can even be measured empirically). By making fewer assumptions, it reduces the risk of misspecification.
- Existing approaches use the Cramér-Rao lower bound for unbiased decoders, which are rarely optimal. Generalizations to biased decoders may be possible but may lack practicality or advantage (**Sec. S6.3**). Our framework does not require restricting to specific decoder types.

In essence, information encoding trades off assumptions and model specificity to gain flexibility, inductive applicability directly from data, and realistic characterization of uncertainty reduction. This expands usefulness beyond a limited set of modeled scenarios.

### S6.1 Background

A large body of research has examined the design of imaging systems using the Cramér-Rao lower bound. A prominent example centers on designing better point spread functions

for the localization of single point emitters in fluorescence [87, 84, 88, 89, 90, 85, 91] or phase [92] microscopy. It has also been used to estimate system characteristics such as wavefront sensing [93].

This bound gives the minimum mean squared error of an unbiased estimate of a deterministic (non-random) parameter. Mathematically, let  $X$  be a random variable with distribution  $p(x; \theta)$ , where  $\theta$  is a deterministic parameter. In the context of imaging systems,  $X$  typically represents a noisy intensity measurement under an assumed noise model (e.g. Poisson noise), and  $\theta$  is a parameter describing the object to be estimated. In practice this parameter is often a vector (e.g. a vector containing the XYZ position of a single point emitter), but for simplicity here we focus on the case of a scalar parameter unless otherwise noted.

Let  $\hat{\theta}(X)$  be an unbiased estimator of  $\theta$ : Using a noisy measurement  $X$ , it makes a deterministic prediction of the true value  $\theta$ , which is correct in expectation. The Cramér-Rao Inequality states that for any unbiased estimator  $\hat{\theta}(X)$ , the mean squared error of the estimate must be greater than or equal to the inverse of the Fisher information:

$$\mathbb{E} [(\hat{\theta}(X) - \theta)^2] \geq \frac{1}{I_F(\theta)} \quad (43)$$

where  $I_F(\theta)$  is the Fisher information of  $\theta$ , defined as:

$$I_F(\theta) = E [(\nabla_{\theta} \log p(x; \theta))^2]$$

For many common distributions, the Fisher information can be understood as akin the inverse of the distribution’s variance. Intuitively, this bound states that the more noisy (higher variance) observed data is, the more difficult it will be to correctly estimate the true value of  $\theta$ .

**Important note:** Fisher information is a distinct concept from Shannon’s mutual information/entropy. As with other parts of this work, we use the word “information” to refer to Shannon’s definition of information, and Fisher information, when used, is explicitly identified. These two quantities arise from separate fields—estimation theory and information theory—which were separately developed (though there are known theoretical connections between these quantities in certain circumstances) [83].

In the context of the point localization problem in microscopy, the Cramér-Rao lower bound describes how well precisely a single point can be localized in space. By calculating, comparing, and optimizing the Cramér-Rao lower bound for different physical encoding systems (e.g. those with different point spread functions), decoding performance can be improved, yielding better imaging systems.

## S6.2 Cramér-Rao lower bound-based design and its limitations

The approach of designing physical systems based on the Cramér-Rao lower bound has inherent limitations that prevent its application outside of a narrow set of applications in which the decoding problem is limited to estimation of one or a few parameters. Furthermore, even when it can be applied, it requires developing a complete mathematical model of the physics of image formation with respect to the parameter of interest. These limitations have thus far prevented its application outside a narrow range of problems, which include

estimation of the position or mass of a single particle [87, 84, 88, 89, 90, 85, 94], or estimating a single optical aberration such as defocus [93]. Below, we discuss these limitations in more detail.

### S6.2.1 The difficulties of creating parametric models

Creating parametric models is essential for calculating the Cramér-Rao lower bound, but it becomes challenging when dealing with high-dimensional objects due to the difficulty of parameterizing objects in a way that captures important aspects of decoders, while also retaining computational tractability.

The computation of the Cramér-Rao lower bound requires calculation of Fisher Information, which in turn requires a parametric model of the data distribution, denoted as  $p(x; \theta)$ . This parametric model stipulates the probability of a specific outcome  $x$ , given a certain parameter  $\theta$ .

In certain scenarios,  $p(x; \theta)$  can be analytically defined. For example, in the point localization problem,  $\theta$  denotes a 3-dimensional vector that marks the XYZ location of a point emitter (the bold type indicates it is a vector of parameters), and  $x$  denotes the intensity of a specific pixel. Given known equations for the system’s noise characteristics and image formation mechanism,  $p(x; \theta)$  can be precisely defined. This can be used to compute Fisher Information and the Cramér-Rao lower bound for a single pixel, and the process can be repeated over each pixel  $x$  to get an averaged bound.

However, creating a straightforward equation-based model for imaging most types of objects is usually very challenging due to the difficulty and increasing complexity of adding additional parameters. Most objects being imaged lack the simplicity of a single point emitter, which can be fully described by its XYZ location. One potential way to circumvent this issue is a more general purpose parameterization of the object in which it is represented by a discrete array of pixel values [92]. However, unbiased estimators are rarely used on high-dimensional estimation problems like this. Furthermore, the Cramér-Rao lower bound is in terms of mean squared error, which, when applied to an array of pixels, generally does not effectively capture semantically meaningful information about objects [95].

**Generalizing from the simple case** In light of the the difficulties of extending this approach to objects with high-dimensional parameterizations, another possibility is to design imaging systems on simple classes of objects with the hope that they will generalize to other classes of objects. Taking such an approach requires making additional assumptions with unknown effects on results. Our experiments in minimal 1-Dimensional simulations show that the object-dependence of imaging systems can be readily demonstrated (**Sec. S1.2**), which may in part explain why empirical solutions to particle localization problems deviate from theoretical predictions [91].

### S6.2.2 Unbiased estimators are usually suboptimal

In addition to the practical difficulties of formulating complex parametric models and computing corresponding Cramér-Rao lower bounds, there remains the limitation that the (standard) Cramér-Rao lower bound quantifies the minimum mean squared error only of unbiased

estimators. While constraining an estimator to be unbiased is arguably a reasonable choice for simple, low-dimensional parameters like the location of a single point in 3D space, most estimators used in practice are in fact biased [96, 97] and state-of-the-art methods for solving image processing tasks almost exclusively use biased estimators to achieve high performance.

The bias-variance tradeoff [98] provides a useful perspective: biased estimators, while possessing higher bias, can have lower variance, thereby potentially reducing overall error. Thus, with bias, estimators with better error than the standard Cramér-Rao lower bound can be achieved. A classic illustration of this principle is the James-Stein estimator [99], which improves the estimation of multiple parameters simultaneously by shrinking individual estimates towards a common mean. It is based on the counterintuitive principle that, under certain conditions, an estimator that partially pools the data towards a central value can produce overall estimates that are closer to the true values than those obtained by estimating each parameter independently, especially when dealing with small sample sizes or high-dimensional data. It results in lower average error than the unbiased sample mean approach for Gaussian random variables when the number of dimensions is  $\geq 3$ .

Furthermore, the advantages of biased estimators are clear on empirical problems, particularly high-dimensional ones. State of the art methods on image-to-image estimation problems like denoising and deconvolution are usually achieved using deep neural networks [9] or with iterative optimization procedures that use regularization to bias the estimates towards certain classes of solutions.

Since computational imaging relies heavily on biased estimators for most image processing tasks, designing systems focused solely on minimizing the error of unbiased estimators, or assessing empirical performance based on this criterion, can provide only a narrow range of guarantees, and it is unclear if the conclusions reached by these guarantees can be generalized to a broader range of applications. This raises the question of what additional theoretic tools can be used to address this more general case.

### S6.3 The challenges of generalizing estimation-theoretic design

This section explores alternative approaches to estimation theory, focusing on the use of biased estimators and Bayesian Cramér-Rao lower bounds to address the limitations of the Cramér-Rao lower bound.

**The biased Cramér-Rao lower bound** Though the (standard) Cramér-Rao lower bound only pertains to unbiased estimators, there are variants and related inequalities that can be applied more broadly.

The first is the biased version of the Cramér-Rao lower bound:

$$\mathbb{E} \left[ (\hat{\theta}(X) - \theta)^2 \right] \geq \frac{(1 + \nabla_{\theta} b(\theta))^2}{I_F(\theta)} + b(\theta)^2$$

Where  $b(\theta)$  is the bias of the estimator as a function of  $\theta$ :

$$b(\theta) = \mathbb{E} \left[ \hat{\theta} \right] - \theta$$

While this form may appear promising, it is in practice challenging for similar reasons to those described in section S6.2.1. Computing the gradient of the expectation of the estimator in high dimensions is a challenging statistical problem in its own right, and this process would need to be repeated for each value of  $\theta$ , necessitating another high-dimensional integration. Furthermore, this bound is not universal—it changes depending on the bias of the estimator in question. This makes it more difficult to determine the best performance of an ideal theoretical estimator, and thus more difficult to determine how close a real estimator come to achieving that performance.

**The Bayesian Cramér-Rao lower bound (van Trees inequality)** One way of addressing the limitations of the (standard) Cramér-Rao lower bound for unbiased estimators and its biased estimator variant can be found by generalizing the estimation problem to consider not just a single value of the parameter  $\theta$ , but instead consider it to also be random (the upper case  $\Theta$  is used to denote the corresponding random variable).

Like the standard Cramér-Rao lower bound, the van Trees inequality (also known as the Bayesian Cramér-Rao lower bound) [100, 96] provides a lower bound on the squared error that can be achieved in a parameter estimation problem. Mathematically:

$$\mathbb{E} \left[ (\hat{\theta}(X) - \Theta)^2 \right] \geq \frac{1}{\mathbb{E} [I_F(\Theta)] + J(\Theta)} \quad (44)$$

Compared to the standard Cramér-Rao lower bound (equation 43), this inequality makes two important changes. First, the Fisher information of a particular parameter value  $\theta$  has been replaced with a probability-weighted average over all possible values of  $\theta$ . Second, there is an additional term  $J(\Theta)$ , defined as:

$$J(\Theta) = \mathbb{E} [(\nabla p(\Theta))^2] \quad (45)$$

where  $p(\cdot)$  is the probability of a particular value of  $\Theta$ . This can be approximately understood as quantifying how concentrated the distribution of the random variable  $\Theta$  is. The more concentrated the distribution of the parameter  $\Theta$  is, the more precisely it can be estimated from noisy measurements. Biasing estimates towards more probable values of  $\Theta$  enables estimation error to be lowered on average.

This inequality formalizes an important intuition: The theoretical limit of the average error with which a parameter of interest can be estimated (such as some property of an object being imaged) is dependent upon the distribution of that parameter. Changing the distribution of the parameter can change the theoretical limits of performance, as well as the the form of optimal estimators.

## S6.4 Connections between estimation and information theory

Originally, information theoretic quantities like entropy and mutual information were developed for noise-affected message transmission. However, these tools have significant theoretical links to estimations of the precision of noise-corrupted random variables. Though these connections are mostly known only for simpler analytical cases such as Gaussian random

variables, they nonetheless provide insights into the relationships between these fields [83]. Here we highlight some of these connections.

An important insight is that where these connections are recognized, designing imaging systems using either estimation or information measures tends to have similar objectives. However, estimation measures have inherent limitations in their applicability, as previously discussed. In contrast, information theory tools don't share these restrictions, positioning them as potentially universal tools for designing physical imaging systems across a variety of applications. Several known inequalities capture the known relationships between these findings and goals of information and estimation theory.

Much of estimation theory centers on limits defined in terms of mean squared error of signals. While mean squared error has many appealing properties, its shortcomings, particularly in the context of quantifying the perceptual and semantic quality of images are readily apparent [95]. This has, for example, motivated work on alternative ways of quantifying error [101, 102].

**Efroimovich inequality** In contrast, rate distortion theory, a branch of information theory, can be used to understand the fundamental limits and behavior of a wide variety of loss functions. The connection from the lower bounds used in estimation theory and information theory can be readily seen in the Efroimovich inequality [103], which generalizes the van Trees inequality (Equation 44) from providing a bound on only mean squared error to providing a bound on a more general way of quantifying uncertainty, the entropy of a parameter  $\theta$  given a noisy measurement  $X$ :

$$\frac{1}{2\pi e} e^{2h(\Theta|X)} \geq \frac{1}{\mathbb{E}[I_F(\Theta)] + J(\Theta)}$$

Here,  $h(\Theta | X)$  is the differential entropy of a parameter given data  $X$ . This inequality can be used to derive bounds on loss functions other than mean squared error in terms of information theoretic quantities [97, 104].

**I-MMSE formula** Another known relationship with particular relevance to this work is known as the I-MMSE formula (short for Information - minimum mean squared error), which states that [105, 83]:

$$I(X; Y) = I(X; \sqrt{s}X + N) = \frac{1}{2} \int_0^s \text{mmse}(X | \gamma X + N) d\gamma$$

In this equation,  $X$  is a signal of interest, and  $Y = \sqrt{s}X + N$  is a noisy measurement of that signal, created by adding independent Gaussian noise  $N$  to the original signal such that the resultant signal-to-noise ratio is  $\sqrt{s}$ .  $\text{mmse}(\cdot)$  is the minimum mean squared error of estimating  $X$  given  $Y$  (i.e. the Bayesian Cramér-Rao lower bound shown in equation 44). From this formula, the mutual information  $I(X; Y)$  is equal to the minimum mean squared error of the optimal estimator, averaged over all achievable signal-to-noise ratios.

This formula shows that mutual information quantifies the same operational idea as the (Bayesian) Cramér-Rao lower bound in the case of additive Gaussian noise, which strongly suggests that the quantities may serve similar purposes under more general noise models.

This relationship can be visualized in the signal coordinate representation, which provides further intuition as to why these quantities are closely related. **Figure S19** shows the distributions of noisy measurements for 6 different signals with a measurement system that imparts additive Gaussian noise. Since mutual information is operationally defined as the number of signals that can be reliably distinguished in the presence of noise, decreasing the maximum signal-to-noise ratio lowers the mutual information. Simultaneously from the estimation theory perspective, it impedes the ability to estimate the original signal from a noisy measurement of it, because it increases the ambiguity as to which input signal gave rise to the measurement.

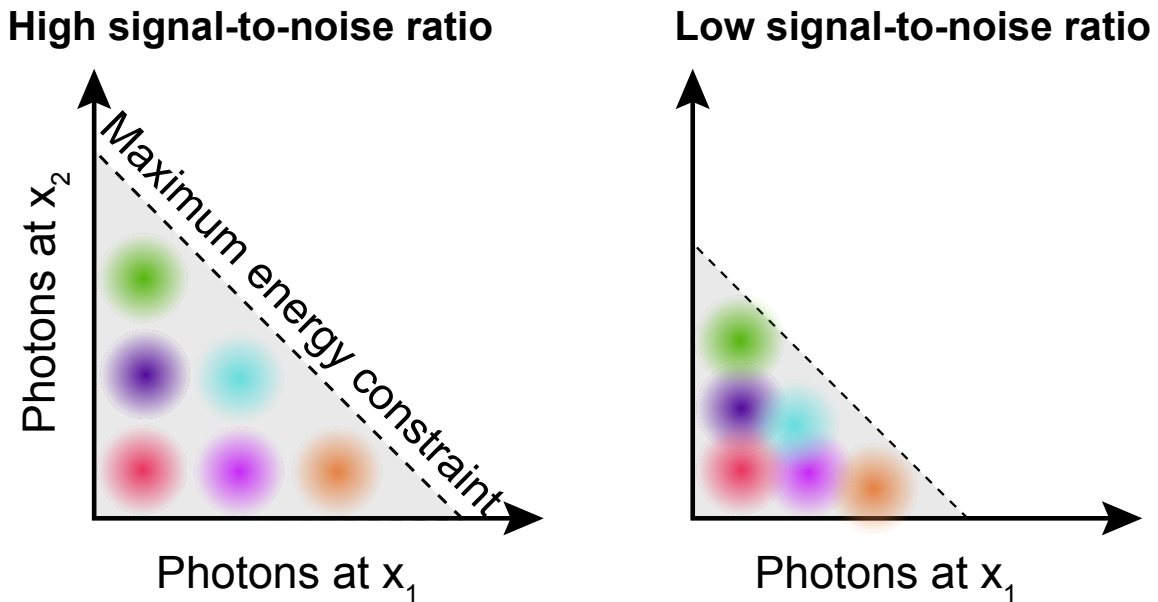


Figure S19: **Visualizing the connection between information and estimation.** Shown are noisy measurements of 6 distinct signals with high and low signal-to-noise ratios. With less noise, the signals remain more distinguishable, increasing mutual information. Simultaneously, lower noise reduces uncertainty in inferring the true signal, improving estimability.

This theoretical connection, combined with the developments in the present work that enable estimation of mutual information across many types of imaging systems provides a means of generalizing the successes of estimation-theoretic design criteria to a wide variety of imaging systems, without the requirements for detailed, system-specific mathematical modeling.

## S7 Comparison to compressed sensing

### A brief overview of compressed sensing

Traditionally, signal acquisition systems such as imaging systems were built upon the Nyquist sampling theorem, which states that to ensure perfect signal reconstruction, the sampling frequency should be twice the maximum frequency present in the signal. In contrast, compressed sensing theory demonstrates that under certain assumptions, signals can in fact be measured and reconstructed from fewer samples than the Nyquist theorem requires. It guarantees perfect recovery of the signal when no noise is present and “robust” performance in the presence of additive Gaussian noise, which means that the error in the signal reconstruction is within a multiplicative constant of the noise level.

The findings of compressed sensing are contingent upon specific assumptions about the signal, the measurement system, and the reconstruction algorithm. In its original formulation, these are:

- **Sparsity of the signal:** The signal, when depicted in a suitable basis (i.e., identifying a linear combination of vectors that equals the signal), must have coefficients for the basis vectors that are predominantly zero.
- **Incoherence:** The measurements of the signal should *not* be sparse. The degree of incoherence between the measurement matrix and the sparsity basis gauges the level to which this requirement is met.
- **Noise:** The measurement noise must follow a Gaussian distribution and should be independent of the signal.
- **Reconstruction algorithm:** The algorithm used to estimate the original signal from the noisy measurements should belong to a subset of optimization algorithms with verifiable guarantees.

When the specific assumptions of compressed sensing are met, and no additional knowledge about the signal exists, the physical sensing mechanism and reconstruction algorithms provided by compressed sensing approach the fundamental limits of reconstruction error [106]. However, accessing additional information about the signal beyond just the measurements can significantly enhance reconstruction performance. For example, even simple constraints like nonnegativity provide further structure, enabling improved recovery compared to relying solely on compressed sensing assumptions. More broadly, any knowledge narrowing down probable signals, whether linear sparsity, probability distributions, or other patterns, can help integration with fewer samples or decreased error. Both theoretically and experimentally, a hybrid approach tailored to exploit problem-specific knowledge in conjunction with models offers tangible performance gains over either in isolation.

For example, if the signal doesn’t strictly reside in a low-dimensional linear subspace, but instead can be synthesized by passing a low dimensional vector through a nonlinear generative model, theoretical and empirical performance of traditional compressed sensing can be improved by a factor of 10 or more [107] [108] [109].

An even more general framework for describing signal acquisition can be achieved by formulating probabilistic models of the signals being measured, or the objects from which those signals originated.<sup>6</sup> These models can describe various types of object or signal redundancy, including the special case of signal sparsity. In addition to the traditional focus of compressed sensing on signal reconstruction error, probabilistic models can be used to define the average error when estimating the original signal, or executing any subsequent tasks [111, 112, 110, 113, 113, 114, 115, 6]. This approach demonstrates that significantly better performance can be achieved, both in theory and experiment, for various classes of signals.

## Methods

**Stationary Gaussian Process model** Stationary Gaussian process models were fit to image distributions using sub-image crops, typically around  $30 \times 30$  pixels in size. The mean of the stationary Gaussian process was estimated using the average number of photons over all image patches. The estimated covariance matrix was initialized using the covariance matrix of vectorized image patches, which was then averaged along diagonals and block diagonals to enforce a doubly Toeplitz structure. To ensure positive definiteness of the covariance matrix, any eigenvalues below a floor (typically  $10^{-3}$ ) were set to the floor value. It was not always possible to achieve a positive definite matrix with the correct doubly Toeplitz structure using this method.

To refine the covariance estimate, an iterative optimization procedure was used with the negative log likelihood of a training dataset of images given the current mean and covariance matrix as a loss function. Proximal stochastic gradient descent was used to optimize the eigenvalues of the covariance matrix, keeping the eigenvectors and mean vector fixed. At each step, a proximal operator was applied which maintains positive definiteness by having the eigenvalues projected to be at least the floor value after each update, and a new eigendecomposition was computed. Since the loss function was highly sensitive to the parameters, gradients were clipped to be  $\leq 1$  to prevent the optimization procedure from diverging.

New images were sampled by having samples drawn from the multivariate Gaussian distribution defined by the learned stationary mean vector and covariance matrix. For samples larger than the patch size on which the model was trained (and the corresponding covariance matrix), ancestral sampling was used, in which additional pixels were generated conditional on previous pixels' values.

**PixelCNN model** The images were modeled using a PixelCNN model adapted from prior work. The model has vertical and horizontal masked convolution layers arranged in a stack.

---

<sup>6</sup>There is a subtle distinction between objects and signals. Signals are generally assumed to have finite bandwidth, which means they can be represented by a finite set of real numbers. However, this is not true of the objects themselves, which cannot in general be represented by a finite number of samples [2]. Thus, the complexity of modeling and object increases with the detail of the model. As a result, it has been shown in [110] the fundamental limits of measurement and estimation depend on the growth rate of object uncertainty with increasingly finer discretizations of space.

This allows modeling the conditional distribution of each pixel given the previous pixels in raster scan order.

We modified the original categorical output distribution to instead use a Gaussian mixture density [80] at each pixel. The Gaussian means were initialized randomly uniformly between the training image minimum and maximum values. The standard deviations were initialized to the softplus output of a dense layer, clipped to be between 1 and the training set standard deviation.

During training, small uniform noise was added to the discrete-valued images to account for modeling them with a continuous distribution. The noise prevents the likelihoods from going to infinity and overfitting to the exact training values.

The model was trained via maximum likelihood on crops from the images using the Adam optimizer. Additional regularization comes from dilated convolutions in the stack. Hyperparameters included a learning rate of 0.01 and training for 200 epochs with early stopping based on the validation set likelihood.

The trained model can then generate samples by ancestral sampling, where pixels are generated auto-regressively in raster scan order using the conditional distribution from the model. This same conditional distribution provides the likelihood for evaluation images.

**Synthetic experimental noise** Experimental data was simulated to have been collected with fewer photons by adding simulated photon shot noise. However, since the experimental data already contains some shot noise, it is necessary to determine how noisy the images already are, and then only add additional noise as needed.

To simulate a lower photon count, each pixel with photon count  $p$  was multiplied by a fraction  $f$  to reduce the photon count to  $fp$ . Assuming the dominant source of noise in the original image is photon shot noise, the variance of the noise in the original image is approximately  $p$ , and the variance in the reduced photon count image is approximately  $f^2p$ . The desired variance of the reduced photon count image is equal to its mean,  $fp$ . Since the sum of two independent Gaussian random variables with variances  $a$  and  $b$  is a Gaussian random variable with variance  $a + b$ , we can add noise to the reduced photon count image to achieve the desired variance. Additional zero-mean Gaussian noise was added with variance  $fp - f^2p$ . The standard deviation of the added noise was then  $\sqrt{fp(1 - f)}$ .

**Information estimation** The mutual information between the noisy measurements  $\mathbf{Y}$  and clean images  $\mathbf{X}$  was estimated as a difference of entropies. The conditional entropy  $H(\mathbf{Y}|\mathbf{X})$  was estimated using the clean images, when available. For Poisson noise, a Gaussian approximation to the Poisson distribution was used. For Gaussian noise, the conditional entropy depends only on the noise standard deviation.

To estimate the marginal entropy  $H(\mathbf{Y})$ , a probabilistic model was trained on patches from the noisy measurements. Either a stationary Gaussian process fit or a PixelCNN model was used. These models were optimized via maximum likelihood on a training subset of images. On a held-out test set,  $H(\mathbf{Y})$  was estimated by numerically evaluating the negative log-likelihood per pixel under the trained model. For the Gaussian process, the analytic differential entropy was also computed.

The mutual information was then estimated as  $I(\mathbf{Y}; \mathbf{X}) = H(\mathbf{Y}) - H(\mathbf{Y}|\mathbf{X})$ . Variants

were also explored, including having the PixelCNN conditioned on auxiliary information to quantify the task-relevant mutual information.

Bootstrapping provided confidence intervals on the information estimates. Additional details like model architecture, optimization procedures, and evaluation metrics are given elsewhere.

**Patching strategies** Due to constraints on memory, compute power, and available data, it was not always feasible to estimate information based on full images. Consequently, we employed various patching strategies to sub-select data to feed it into our parameterized model of the true data distribution.

The most straightforward approach was random patching. For this method, we defined the number of patches per image and the patch size. Patches were then randomly selected from locations in each image across the entire dataset. These randomly sampled patches were used to train the parameterized distribution model. Random patching worked well when the object distribution was stationary (consistent across the image), and the point spread function (PSF) had relatively small spatial extent. However, a key limitation was that random patching overrepresented pixels in the center of images, as there were more valid patches that could contain those central pixels.

An alternative fixed patching method aimed to compensate for non-stationary image distributions. Similar to random patching, we extracted a fixed number of patches per image, in this case a single patch, but crucially, the patch location was kept constant across all images. This ensured that patches were drawn from corresponding regions, potentially capturing positional biases in the data and possibly accounting for non-stationary image distributions.

As another method to better account for spatially varying information within images due to a non-stationary distribution, we explored uniform patching. Here, the patch size was defined, and then patches were sampled from a uniform grid laid over each image, with grid square sizes equal to the patch size. Uniform sampling across the image plane allowed the patching process to capture non-stationary distributions more effectively than random selection.

For both random and uniform patching, an optional padding step could be applied. Padding involved extending the images by replicating border pixels or using the average/-median pixel value. With padding, each original image pixel had the same number of valid patches it could belong to, preventing potential undersampling of edge regions.

Finally, we investigated random mask patching, crucial for systems with PSFs exhibiting large spatial extents. A patch size was specified, but instead of taking contiguous rectangular patches, we randomly selected a mask containing the desired number of disconnected pixels. Sampling each image at the mask locations captured long-range dependencies between pixels that a compact local patch may miss.

The choice of patching strategy was guided by the inherent properties of the imaging system and object distributions. By judiciously sub-selecting data in this manner, we can estimate information quantities that would otherwise be computationally prohibitive with full images.

**Cell protein expression decoder** To predict protein expression from images of single leukocytes under LED array illumination, each image was fed into a neural network decoder that predicted the levels of 8 marker proteins: CD3, CD19, CD56, CD123, HLA-DR, CD14, CD16, and CD45. A DenseNet121 convolutional neural network pretrained on ImageNet was used as the first part the architecture. Since ImageNet has 3 different channels, but the images we used have only a single channel, the first conv layer weights are averaged over the RGB channels.

The output of this network feeds into a global average pooling layer followed by eight fully-connected networks with two hidden layers each, with one specific to each target protein. The outputs of these networks were the parameters of a Gaussian mixture density [80], enabling the direct evaluation of the negative log likelihood of each target datum.

A composite loss function sums the negative log likelihood loss for each marker output. Missing target values are masked out. The Adam optimizer is used with a learning rate of  $5e-5$ . Networks are trained with early stopping, with training ceasing after loss on a validation has not decreased for 20 epochs. Each epoch consisted of 4000 steps with batches of 16 images.

**LED array experiments** Images of single cells under Brightfield, Differential Phase Contrast, and Single LED illumination were normalized to equal photon counts (see 1). Full images were used to train the convolutional neural network described above, and performance was quantified by calculating negative log likelihood on a held out set of test data.

To compute mutual information,  $40 \times 40$  pixel patches were cropped out uniformly throughout the image and mutual information was estimated using the PixelCNN estimator. Estimates were computed for 11 experimental replicates at each illumination condition and photon count. The minimum value over these replicates was taken as the final estimate, since the estimator provides an upper bound. The 11 estimates of protein prediction performance were then resampled 1000 times to estimate a confidence interval around the median estimate (i.e. a bootstrap procedure).

**Lensless imaging experiments** The CIFAR10 dataset was used for the lensless imaging experiments. This dataset consists of 60,000 total images across 10 classes. To convert CIFAR10 image pixel values to a synthetic photon count, the dataset was scaled to have mean value equivalent to the desired photons per pixel. Measurements were generated using convolution with each system point spread function (PSF). Images from the dataset were randomly selected and 9 images tiled in a  $3 \times 3$  grid before convolution (valid mode, no zero padding) with each system PSF. This tiling was implemented to prevent intensity falloff due to zero padding on convolution at the edges, ensuring that image content was brought in uniformly at every point in the field of view, forming a spatially consistent texture. After convolution, Poisson noise was added to the encoded measurements. CIFAR10 images are only  $32 \times 32$  pixels, so patches equivalent to the image size were used for mutual information estimation. Patches were randomly sampled over the  $65 \times 65$  region corresponding to the valid convolution, and 10,000 patches were used for estimation. The same mutual information estimates were also achieved with smaller patch sizes and fewer patches. The conditional entropy was estimated using clean images for this data. Mutual information estimates are

done across all photon counts and replicated 5 times each, from which the minimum value is used in all graphs. There is minimal variation across the replicates, typically less than 0.01 bits per pixel.

For the deconvolution task, each image in the CIFAR10 dataset is convolved with an encoder. Then, Wiener deconvolution with an automatically tuned regularization parameter is used to reconstruct the original image from the convolved measurement. However, deconvolution is an ill-posed process. Random tiling is not used here, as it does not allow reasonable quality reconstructions that resemble the original images. Successful reconstructions require a bounded region of image content. The mean value of the Mean Squared Error (MSE) across the dataset is plotted, with 90% error bars corresponding to the MSE across the 60,000 images in the dataset.

In addition to the deconvolution task in the main paper, we study object classification using the same encoders. A simple CNN architecture, sufficiently powerful for regular CIFAR10 image classification is used. This consists of two convolutional layers (64 and 128 filters respectively with kernel size 5), each followed by a MaxPool, and two densely-connected layers, the first with 128 nodes and a ReLU activation, and the second with 10 layers and a Softmax activation for classification into the 10 classes. The random tiling process used in mutual information estimation is used for this task as well. The label for classification is based on the center image in the  $3 \times 3$  grid, for which maximum image content is present in the measurement. Classification is repeated 10 times for each photon count and encoder combination, from which the 90% confidence interval is generated.

**Fourier DiffuserScope** Fourier DiffuserScope is a single-shot 3D Fourier lightfield microscope that uses random micro lenses (RMLs) to encode 3D information on a 2D sensor [53]. In this work, we combined the forward model of Fourier DiffuserScope with a differentiable reconstruction network, ISTA-Net [116]. Together, the optical encoder and software decoder constitute a computational imaging system that we optimized using end-to-end (E2E) design, learning the positions and focal lengths of the RMLs as well as the parameters of the reconstruction network.

Measurements were simulated by passing ground truth 3D volumes through the optical forward model. The optical encoder was modeled as a sum of lateral 2D convolutions of each object slice with its corresponding slice of the 3D point spread function (PSF). The simulated measurements were then fed into the ISTA-Net. The ISTA-Net consists of 10 unrolled iterations, each comprising a gradient step and a proximal step. The proximal step utilizes a learned sparsifying transform to map the measurement into a sparse domain, where soft thresholding is performed, and a learned inverse transform maps back to the reconstruction space.

A 3D fluorescent imaging lung dataset was used for optimizing the full pipeline. The lung volume was cropped into 3000 patches of size  $11 \times 100 \times 100$  for training. We trained the pipeline to convergence while saving checkpoints throughout the training process. After training completion, we loaded checkpoints of the initial model, an intermediate step, and the converged model. The parameters of the optical encoder were then frozen, and the reconstruction network was trained until convergence. We repeated this final training procedure 10 times to reduce the chance of being caught in a local minimum when training

the reconstruction network.

The average normalized mean squared error (NMSE) was calculated for each of the 10 models on a test set of 300 patches cropped from the original lung volume. We report the median value for NMSE across the 10 models and calculate a 90 percent confidence interval based on the standard deviation over the 10 models.

Additionally, we calculated mutual information for each checkpoint. For this, we fit 10 PixelCNN models. We simulated 3000 measurements using the training set and estimated mutual information using the PixelCNN estimator. The PixelCNN network was trained on  $16 \times 16$  patches sampled via the random mask patching method described previously. Random mask patching allows for the capture of long range dependencies between measurement pixels as Fourier DiffuserScope has a PSF with large spatial extent. We report the minimal value across the 10 models as the estimates are upper bounds on the true mutual information between the noisy and noiseless measurements.

**Information Driven Encoder Analysis Learning (IDEAL)** In addition to the end-to-end (E2E) optimization approach described above, we optimized the random micro lenses (RMLs) of Fourier DiffuserScope in a different manner, using our proposed Information Driven Encoder Analysis Learning (IDEAL) method. This allowed us to make comparisons between the two optimization strategies.

For the IDEAL approach, we utilized the same training set of 3000 3D volumes. The volumes were fed through the Fourier DiffuserScope forward model to produce noiseless measurements. Gaussian-approximated shot noise was then added to these noiseless measurements to simulate noisy measurements, replicating the effects of experimental noise.

The mutual information between the noiseless and noisy measurements was calculated using the analytic Gaussian approximation described previously. Briefly, at each step, a batch of noisy measurements was vectorized and their covariance matrix was computed. The log eigenvalues of this covariance matrix were then used to estimate  $H(\mathbf{Y})$ . We used a batch of 512 measurement patches of size  $16 \times 16$ . These patches were selected using the random mask patching strategy, where a random mask with the same number of pixels as the patch size was generated, and the corresponding pixels were sampled from the measurements. The random mask used for patching was updated at each optimization step.

In contrast to the E2E approach, where the entire pipeline was optimized jointly, the negative mutual information between the noiseless and noisy measurements served as the loss function for optimizing only the RML configurations in the IDEAL method. By maximizing this mutual information, we aimed to learn RML designs that preserved the maximum amount of information from the 3D object, enabling accurate reconstruction from the 2D sensor measurements.

Again, we saved checkpoints at initialization, an intermediate step, and after final optimization of the RML configurations using the IDEAL method. To evaluate the performance at each of these checkpoints, we calculated the NMSE by initializing an ISTA-Net reconstruction network and training it to convergence on the measurements simulated with the RML configurations from the respective checkpoint. This ISTA-Net training procedure was repeated 10 times to reduce the chance of being caught in a local minimum.

The NMSE was calculated for each of the 10 trained ISTA-Net models on a test set of 300

patches cropped from the original lung volume. We report the median value for NMSE across the 10 models and calculate a 90 percent confidence interval based on the standard deviation over the 10 models, following the same approach as the previous end-to-end experiment.

Additionally, we calculated mutual information for each checkpoint in a similar manner to the end-to-end experiment. We fit 10 PixelCNN models to the simulated measurements using the training set. The PixelCNN was used as it provides a better fit to the data distribution compared to stationary Gaussian approximation, enabling a tighter upper bound on the mutual information estimation. The minimal value across these 10 PixelCNN models was reported as an upper bound on the true mutual information between the noiseless and noisy measurements. Again, the PixelCNN was trained on  $16 \times 16$  patches sampled with the random mask approach.

**1D simulations** We studied a simplified 1D system consisting of objects encoded with bandlimited, positive, infinitely periodic point spread functions. Kernels were parameterized by the amplitude, real, and imaginary components of their discrete Fourier transform, because this gave more stable results when optimizing them.

Encoded signals were integrated at fixed intervals to simulate “pixels”. Information estimates were then performed on these discretized signals by reshaping them into images and using the PixelCNN estimator.

Encoder optimization relied on stochastic gradient ascent on the Gaussian-approximated mutual information between integrated signals and simulated noisy measurements. Gaussian noise was added independently to each pixel.

Experiments characterized the object-dependence of encoder ranges by attempting to match various target signals from fixed object types. We also quantified tradeoffs between information capacity and key parameters like signal-to-noise ratio, bandwidth, and sampling density for different object distributions. Finally, we estimated the information loss due to constraints on encodable signal distributions relative to the optimal unconstrained case.

## References

- [1] Claude E Shannon. “A mathematical theory of communication”. In: *The Bell System Technical Journal* 5.1 (Jan. 1, 1948). ISBN: 0252725484, p. 3. ISSN: 15591662. DOI: 10.1145/584091.584093. arXiv: [chao-dyn/9411012](https://arxiv.org/abs/chao-dyn/9411012). URL: <http://portal.acm.org/citation.cfm?doid=584091.584093>.
- [2] P.B. Fellgett and E.H. Linfoot. “On the assessment of optical images”. In: *Philosophical Transactions of the Royal Society of London. Series A, Mathematical and Physical Sciences* 247.931 (Feb. 17, 1955). Publisher: Yale University Press, pp. 369–407. ISSN: 0080-4614. DOI: 10.1098/rsta.1955.0001. URL: <https://www.jstor.org/stable/10.2307/j.ctt211qv60.7>.
- [3] I. J. Cox and C. J. R. Sheppard. “Information capacity and resolution in an optical system”. In: *Journal of the Optical Society of America A* 3.8 (Aug. 1, 1986), p. 1152. ISSN: 1084-7529. DOI: 10.1364/JOSAA.3.001152. URL: <https://www.osapublishing.org/abstract.cfm?URI=josaa-3-8-1152>.

- [4] Mark A. Neifeld. “Information, resolution, and space–bandwidth product”. In: *Optics Letters* 23.18 (1998), p. 1477. ISSN: 0146-9592. DOI: 10.1364/ol.23.001477.
- [5] Christoph Wagner and Gerd Häusler. “Information theoretical optimization for optical range sensors”. In: *Applied Optics* 42.27 (Sept. 20, 2003), p. 5418. ISSN: 0003-6935, 1539-4522. DOI: 10.1364/AO.42.005418. URL: <https://opg.optica.org/abstract.cfm?URI=ao-42-27-5418> (visited on 02/17/2024).
- [6] Yihong Wu and Sergio Verdú. *Optimal Phase Transitions in Compressed Sensing*. July 10, 2012. arXiv: 1111.6822[cs,math,stat]. URL: <http://arxiv.org/abs/1111.6822> (visited on 07/13/2023).
- [7] Florian Willomitzer. *Single-Shot 3D Sensing Close to Physical Limits and Information Limits*. Springer Theses. Cham: Springer International Publishing, 2019. ISBN: 978-3-030-10903-5. DOI: 10.1007/978-3-030-10904-2. URL: <http://link.springer.com/10.1007/978-3-030-10904-2> (visited on 02/17/2024).
- [8] Shaofan Yuan et al. “Geometric deep optical sensing”. In: *Science* 379.6637 (Mar. 17, 2023). Publisher: American Association for the Advancement of Science, eade1220. DOI: 10.1126/science.ade1220. URL: <https://www.science.org/doi/10.1126/science.ade1220> (visited on 04/20/2023).
- [9] Yann Lecun, Yoshua Bengio, and Geoffrey Hinton. “Deep learning”. In: *Nature* 521.7553 (2015). ISBN: 3135786504, pp. 436–444. ISSN: 14764687. DOI: 10.1038/nature14539. arXiv: 1312.6184v5. URL: <http://www.scopus.com/inward/record.url?eid=2-s2.0-84930630277&partnerID=40&md5=befeefa64ddca265c713cf81f4e2fc54>.
- [10] Ayush Bhandari, Achuta Kadambi, and Ramesh Raskar. *Computational imaging*. Cambridge, Massachusetts: The MIT Press, 2022. 447 pp. ISBN: 978-0-262-04647-3.
- [11] Gordon Wetzstein et al. “Inference in artificial intelligence with deep optics and photonics”. In: *Nature* 588.7836 (2020), pp. 39–47. ISSN: 14764687. DOI: 10.1038/s41586-020-2973-6.
- [12] W. Lukosz. “Optical Systems with Resolving Powers Exceeding the Classical Limit\*”. In: *Journal of the Optical Society of America* 56.11 (Nov. 1, 1966), p. 1463. ISSN: 0030-3941. DOI: 10.1364/josa.56.001463. URL: <https://www.osapublishing.org/abstract.cfm?URI=josa-56-11-1463>.
- [13] Adolf W. Lohmann et al. “Space–bandwidth product of optical signals and systems”. In: *Journal of the Optical Society of America A* 13.3 (Mar. 1, 1996), p. 470. ISSN: 1084-7529, 1520-8532. DOI: 10.1364/JOSAA.13.000470. URL: <https://opg.optica.org/abstract.cfm?URI=josaa-13-3-470> (visited on 11/29/2023).
- [14] David J. Brady and Nathan Hagen. “Multiscale lens design”. In: *Optics Express* 17.13 (June 22, 2009). Publisher: Optica Publishing Group, pp. 10659–10674. ISSN: 1094-4087. DOI: 10.1364/OE.17.010659. URL: <https://opg.optica.org/oe/abstract.cfm?uri=oe-17-13-10659> (visited on 11/21/2023).

- [15] Jongchan Park et al. “Review of bio-optical imaging systems with a high space-bandwidth product”. In: *Advanced Photonics* 3.4 (June 26, 2021), pp. 369–407. ISSN: 2577-5421. DOI: 10.1117/1.AP.3.4.044001. URL: <https://royalsocietypublishing.org/doi/10.1098/rsta.1955.0001>.
- [16] G. Toraldo di Francia. “Resolving Power and Information”. In: *Journal of the Optical Society of America* 45.7 (July 1, 1955), p. 497. ISSN: 0030-3941. DOI: 10.1364/JOSA.45.000497. URL: <https://www.osapublishing.org/abstract.cfm?URI=josa-46-1-72>.
- [17] Rafael Piestun and David A. B. Miller. “Electromagnetic degrees of freedom of an optical system”. In: *Journal of the Optical Society of America A* 17.5 (May 1, 2000), p. 892. ISSN: 1084-7529, 1520-8532. DOI: 10.1364/JOSAA.17.000892. URL: <https://opg.optica.org/abstract.cfm?URI=josaa-17-5-892> (visited on 04/09/2024).
- [18] Joseph W. Goodman. *Introduction to Fourier optics*. 3rd ed. OCLC: ocm56632414. Englewood, Colo: Roberts & Co, 2005. 491 pp. ISBN: 978-0-9747077-2-3.
- [19] C.E. Shannon. “Communication in the Presence of Noise”. In: *Proceedings of the IRE* 37.1 (Jan. 1949). Conference Name: Proceedings of the IRE, pp. 10–21. ISSN: 2162-6634. DOI: 10.1109/JRPROC.1949.232969.
- [20] Vincent Sitzmann et al. “End-to-end optimization of optics and image processing for achromatic extended depth of field and super-resolution imaging”. In: *ACM Transactions on Graphics* 37.4 (Aug. 31, 2018), pp. 1–13. ISSN: 0730-0301, 1557-7368. DOI: 10.1145/3197517.3201333. URL: <https://dl.acm.org/doi/10.1145/3197517.3201333> (visited on 03/25/2024).
- [21] Qilin Sun et al. “Learning Rank-1 Diffractive Optics for Single-Shot High Dynamic Range Imaging”. In: *2020 IEEE/CVF Conference on Computer Vision and Pattern Recognition (CVPR)*. 2020 IEEE/CVF Conference on Computer Vision and Pattern Recognition (CVPR). Seattle, WA, USA: IEEE, June 2020, pp. 1383–1393. ISBN: 978-1-72817-168-5. DOI: 10.1109/CVPR42600.2020.00146. URL: <https://ieeexplore.ieee.org/document/9157825/> (visited on 03/25/2024).
- [22] Christopher A. Metzler et al. “Deep Optics for Single-Shot High-Dynamic-Range Imaging”. In: *2020 IEEE/CVF Conference on Computer Vision and Pattern Recognition (CVPR)*. 2020 IEEE/CVF Conference on Computer Vision and Pattern Recognition (CVPR). Seattle, WA, USA: IEEE, June 2020, pp. 1372–1382. ISBN: 978-1-72817-168-5. DOI: 10.1109/CVPR42600.2020.00145. URL: <https://ieeexplore.ieee.org/document/9156877/> (visited on 03/25/2024).
- [23] Qilin Sun et al. “End-to-end complex lens design with differentiate ray tracing”. In: *ACM Transactions on Graphics* 40.4 (Aug. 31, 2021), pp. 1–13. ISSN: 0730-0301, 1557-7368. DOI: 10.1145/3450626.3459674. URL: <https://dl.acm.org/doi/10.1145/3450626.3459674> (visited on 03/25/2024).
- [24] Ethan Tseng et al. “Neural nano-optics for high-quality thin lens imaging”. In: *Nature Communications* 12.1 (Nov. 29, 2021), p. 6493. ISSN: 2041-1723. DOI: 10.1038/s41467-021-26443-0. URL: <https://www.nature.com/articles/s41467-021-26443-0> (visited on 03/25/2024).

- [25] Ethan Tseng et al. “Differentiable Compound Optics and Processing Pipeline Optimization for End-to-end Camera Design”. In: *ACM Transactions on Graphics* 40.2 (Apr. 30, 2021), pp. 1–19. ISSN: 0730-0301, 1557-7368. DOI: 10.1145/3446791. URL: <https://dl.acm.org/doi/10.1145/3446791> (visited on 03/25/2024).
- [26] Diptodip Deb et al. *FourierNets enable the design of highly non-local optical encoders for computational imaging*. Nov. 2, 2022. arXiv: 2104.10611[cs, eess]. URL: <http://arxiv.org/abs/2104.10611> (visited on 03/25/2024).
- [27] Vasco Ronchi. “Resolving Power of Calculated and Detected Images”. In: *Journal of the Optical Society of America* 51.4 (Apr. 1, 1961), pp. 458–460. ISSN: 0030-3941. DOI: 10.1364/JOSA.51.0458\_1. URL: [https://www.osapublishing.org/abstract.cfm?URI=josa-51-4-458\\_1](https://www.osapublishing.org/abstract.cfm?URI=josa-51-4-458_1).
- [28] Joseph W. Goodman. *Statistical optics*. Second edition. Wiley series in pure and applied optics. Hoboken, New Jersey: John Wiley & Sons Inc, 2015. 1 p. ISBN: 978-1-119-00945-0.
- [29] J. L. Harris. “Resolving Power and Decision Theory”. In: *Journal of the Optical Society of America* 54.5 (May 1, 1964), p. 606. ISSN: 0030-3941. DOI: 10.1364/JOSA.54.000606. URL: <https://opg.optica.org/abstract.cfm?URI=josa-54-5-606> (visited on 05/19/2024).
- [30] R. Heintzmann and V. Sarafis. “Two point resolution in incoherent imaging”. In: *Optik* 112.3 (2001), pp. 114–118. ISSN: 00304026. DOI: 10.1078/0030-4026-00022. URL: <https://linkinghub.elsevier.com/retrieve/pii/S0030402604700212> (visited on 04/26/2024).
- [31] A. J. den Dekker and A. van den Bos. “Resolution: a survey”. In: *Journal of the Optical Society of America A* 14.3 (Mar. 1, 1997), p. 547. ISSN: 1084-7529. DOI: 10.1364/JOSAA.14.000547. URL: <https://www.osapublishing.org/abstract.cfm?URI=josaa-14-3-547>.
- [32] Alexander Kraskov, Harald Stögbauer, and Peter Grassberger. “Estimating mutual information”. In: *Physical Review E* 69.6 (June 23, 2004). Publisher: American Physical Society, p. 066138. DOI: 10.1103/PhysRevE.69.066138. URL: <https://link.aps.org/doi/10.1103/PhysRevE.69.066138> (visited on 05/08/2023).
- [33] Georges A. Darbellay and Igor Vajda. “Estimation of the information by an adaptive partitioning of the observation space”. In: *IEEE Transactions on Information Theory* 45.4 (1999), pp. 1315–1321. ISSN: 00189448. DOI: 10.1109/18.761290.
- [34] Brian C. Ross. “Mutual information between discrete and continuous data sets”. In: *PLoS ONE* 9.2 (2014). ISSN: 19326203. DOI: 10.1371/journal.pone.0087357.
- [35] David McAllester and Karl Stratos. “Formal Limitations on the Measurement of Mutual Information”. In: (2018). Publisher: arXiv Version Number: 4. DOI: 10.48550/ARXIV.1811.04251. URL: <https://arxiv.org/abs/1811.04251> (visited on 12/05/2023).

- [36] Ben Poole et al. *On Variational Bounds of Mutual Information*. May 16, 2019. DOI: 10.48550/arXiv.1905.06922. arXiv: 1905.06922[cs,stat]. URL: <http://arxiv.org/abs/1905.06922> (visited on 12/05/2023).
- [37] David J C MacKay. *Information Theory, Inference, and Learning Algorithms David J.C. MacKay*. ISSN: 01621459. Cambridge University Press, 2003. ISBN: 978-0-521-64298-9. DOI: 10.5555/971143.
- [38] Aaron van den Oord, Nal Kalchbrenner, and Koray Kavukcuoglu. “Pixel Recurrent Neural Networks”. In: 48 (2016). ISBN: 9781510829008. ISSN: 0269-7491. DOI: 10.1111/ede.12058. arXiv: 1601.06759. URL: <http://arxiv.org/abs/1601.06759>.
- [39] Aäron van den Oord et al. “Conditional Image Generation with PixelCNN Decoders”. In: *arXiv* (2016). ISBN: 9781510829008, pp. 4790–4798. ISSN: 10495258. arXiv: 1606.05328. URL: <https://papers.nips.cc/paper/6527-conditional-image-generation-with-pixelcnn-decoders>.
- [40] Tim Salimans et al. “Pixel CNN++: Improving the Pixel CNN With Discretized Logistic Mixture Likelihood”. In: *Iclr* (2017), pp. 1–10. arXiv: 1701.05517. URL: <https://openreview.net/forum?id=BJrFC6ceg%0Ahttps://arxiv.org/abs/1701.05517>.
- [41] Guoan Zheng, Christopher Kolner, and Changhuei Yang. “Microscopy refocusing and dark-field imaging by using a simple LED array”. In: *Optics Letters* 36.20 (2011). ISBN: 0090-8258 (Print)\r0090-8258 (Linking), p. 3987. ISSN: 0146-9592. DOI: 10.1364/OL.36.003987. URL: <https://www.osapublishing.org/abstract.cfm?URI=ol-36-20-3987>.
- [42] Zachary F. Phillips, Regina Eckert, and Laura Waller. “Quasi-Dome: A Self-Calibrated High-NA LED Illuminator for Fourier Ptychography”. In: *Imaging and Applied Optics 2017 (3D, AIO, COSI, IS, MATH, pcAOP)*. Vol. IW4E.5. 2017. DOI: 10.1364/isa.2017.iw4e.5.
- [43] Henry Pinkard et al. *The Berkeley Single Cell Computational Microscopy (BSCCM) Dataset*. Feb. 9, 2024. arXiv: 2402.06191[cs,q-bio]. URL: <http://arxiv.org/abs/2402.06191> (visited on 02/12/2024).
- [44] Sandra Van Aert, Dirk Van Dyck, and Arnold J. den Dekker. “Resolution of coherent and incoherent imaging systems reconsidered - Classical criteria and a statistical alternative”. In: *Optics Express* 14.9 (2006), p. 3830. ISSN: 1094-4087. DOI: 10.1364/oe.14.003830.
- [45] Shalin B. Mehta and Colin J. R. Sheppard. “Equivalent of the point spread function for partially coherent imaging”. In: *Optica* 2.8 (2015), p. 736. ISSN: 2334-2536. DOI: 10.1364/optica.2.000736.
- [46] Roarke Horstmeyer et al. “Standardizing the resolution claims for coherent microscopy”. In: *Nature Photonics* 10.2 (2016). Publisher: Nature Publishing Group, pp. 68–71. ISSN: 1749-4885. DOI: 10.1038/nphoton.2015.279. URL: <http://www.nature.com/doifinder/10.1038/nphoton.2015.279>.

- [47] Vivek Boominathan et al. “Recent advances in lensless imaging”. In: *Optica* 9.1 (Jan. 20, 2022). Publisher: Optica Publishing Group, pp. 1–16. ISSN: 2334-2536. DOI: 10.1364/OPTICA.431361. URL: <https://opg.optica.org/optica/abstract.cfm?uri=optica-9-1-1> (visited on 02/06/2024).
- [48] Leyla Kabuli, Gina Wu, and Laura Waller. “High-Quality Lensless Imaging with a Random Multi-Focal Lenslet Phase Mask”. In: *Optica Imaging Congress (3D, COSI, DH, FLatOptics, IS, pcAOP)*. Computational Optical Sensing and Imaging. Boston, Massachusetts: Optica Publishing Group, 2023, CW3B.2. ISBN: 978-1-957171-28-9. DOI: 10.1364/COSI.2023.CW3B.2. URL: <https://opg.optica.org/abstract.cfm?URI=COSI-2023-CW3B.2> (visited on 02/06/2024).
- [49] Nick Antipa et al. “DiffuserCam: Lensless Single-exposure 3D Imaging”. In: (2017), pp. 1–9. arXiv: 1710.02134. URL: <http://arxiv.org/abs/1710.02134>.
- [50] Alex Krizhevsky. “Learning Multiple Layers of Features from Tiny Images”. PhD thesis.
- [51] François Orieux, Jean-François Giovannelli, and Thomas Rodet. “Bayesian estimation of regularization and point spread function parameters for Wiener–Hunt deconvolution”. In: *Journal of the Optical Society of America A* 27.7 (July 1, 2010), p. 1593. ISSN: 1084-7529, 1520-8532. DOI: 10.1364/JOSAA.27.001593. URL: <https://opg.optica.org/abstract.cfm?URI=josaa-27-7-1593> (visited on 02/06/2024).
- [52] Changliang Guo et al. “Fourier light-field microscopy”. In: *Optics Express* 27.18 (Sept. 2, 2019), p. 25573. ISSN: 1094-4087. DOI: 10.1364/OE.27.025573. URL: <https://opg.optica.org/abstract.cfm?URI=oe-27-18-25573> (visited on 03/25/2024).
- [53] Fanglin Linda Liu et al. “Fourier DiffuserScope: single-shot 3D Fourier light field microscopy with a diffuser”. In: *Optics Express* 28.20 (Sept. 28, 2020). Publisher: Optica Publishing Group, pp. 28969–28986. ISSN: 1094-4087. DOI: 10.1364/OE.400876. URL: <https://opg.optica.org/oe/abstract.cfm?uri=oe-28-20-28969> (visited on 02/08/2024).
- [54] Y. Bengio, P. Simard, and P. Frasconi. “Learning long-term dependencies with gradient descent is difficult”. In: *IEEE Transactions on Neural Networks* 5.2 (Mar. 1994). Conference Name: IEEE Transactions on Neural Networks, pp. 157–166. ISSN: 1941-0093. DOI: 10.1109/72.279181. URL: <https://ieeexplore.ieee.org/abstract/document/279181> (visited on 03/26/2024).
- [55] Seol-Hyun Noh. “Performance Comparison of CNN Models Using Gradient Flow Analysis”. In: *Informatics* 8.3 (Aug. 13, 2021), p. 53. ISSN: 2227-9709. DOI: 10.3390/informatics8030053. URL: <https://www.mdpi.com/2227-9709/8/3/53> (visited on 03/26/2024).
- [56] Xinge Yang et al. *Image Quality Is Not All You Want: Task-Driven Lens Design for Image Classification*. May 26, 2023. arXiv: 2305.17185[physics]. URL: <http://arxiv.org/abs/2305.17185> (visited on 05/20/2024).
- [57] Xi Chen et al. “Variational Lossy Autoencoder”. In: (2016), pp. 1–17. arXiv: 1611.02731. URL: <http://arxiv.org/abs/1611.02731>.

- [58] Alhussein Fawzi et al. “Image inpainting through neural networks hallucinations”. In: *2016 IEEE 12th Image, Video, and Multidimensional Signal Processing Workshop (IVMSP)*. 2016 IEEE 12th Image, Video, and Multidimensional Signal Processing Workshop (IVMSP). Bordeaux, France: IEEE, July 2016, pp. 1–5. ISBN: 978-1-5090-1929-8. DOI: 10.1109/IVMSPW.2016.7528221. URL: <http://ieeexplore.ieee.org/document/7528221/> (visited on 02/14/2024).
- [59] Thomas M Cover and Joy A. Thomas. *Elements of Information Theory*. Series Title: Wiley Series in Telecommunications. New York, USA: Wiley, Sept. 16, 2005. ISBN: 978-0-471-24195-9. DOI: 10.1002/047174882X. URL: <http://doi.wiley.com/10.1002/0471200611>.
- [60] Henry Pinkard and Laura Waller. *A visual introduction to information theory*. June 15, 2022. arXiv: 2206.07867[cs,math]. URL: <http://arxiv.org/abs/2206.07867> (visited on 09/19/2022).
- [61] Massimo Franceschetti. *Wave Theory of Information*. 1st ed. Cambridge University Press, Nov. 30, 2017. ISBN: 978-1-107-13633-4. DOI: 10.1017/9781139136334. URL: <https://www.cambridge.org/core/product/identifier/9781139136334/type/book> (visited on 08/15/2023).
- [62] Benigno Uria et al. “Neural autoregressive distribution estimation”. In: *Journal of Machine Learning Research* 17 (2016), pp. 1–37. ISSN: 15337928. arXiv: 1605.02226.
- [63] Mathieu Germain et al. “MADE: Masked Autoencoder for Distribution Estimation”. In: 37 (2015). ISBN: 1502.03509. ISSN: 1098-0121. DOI: 10.1103/PhysRevB.91.195316. arXiv: 1502.03509. URL: <http://arxiv.org/abs/1502.03509>.
- [64] H. Nyquist. “Certain Topics in Telegraph Transmission Theory”. In: *Transactions of the American Institute of Electrical Engineers* 47.2 (Apr. 1928). Conference Name: Transactions of the American Institute of Electrical Engineers, pp. 617–644. ISSN: 2330-9431. DOI: 10.1109/T-AIEE.1928.5055024. URL: <https://ieeexplore.ieee.org/document/5055024> (visited on 02/03/2024).
- [65] Kevin Smith et al. “CIDRE: An illumination-correction method for optical microscopy”. In: *Nature Methods* 12.5 (2015), pp. 404–406. ISSN: 15487105. DOI: 10.1038/nmeth.3323.
- [66] Tingying Peng et al. “A BaSiC tool for background and shading correction of optical microscopy images”. In: *Nature Communications* 8 (2017). Publisher: Nature Publishing Group, pp. 1–7. ISSN: 20411723. DOI: 10.1038/ncomms14836. URL: <http://dx.doi.org/10.1038/ncomms14836>.
- [67] J. Beirlant et al. “Nonparametric entropy estimation. An overview”. In: 1997. URL: <https://www.semanticscholar.org/paper/Nonparametric-entropy-estimation.-An-overview-Beirlant-Dudewicz/14ba9dccf06355d1c6478b843ccb8f56d7374409> (visited on 06/23/2023).
- [68] Lyudmyla F. Kozachenko and Nikolai N. Leonenko. “Sample estimate of the entropy of a random vector”. In: *Problemy Peredachi Informatsii* 23.2 (1987). Publisher: Russian Academy of Sciences, Branch of Informatics, Computer Equipment and . . . , pp. 9–16.

- [69] Damiano Lombardi and Sanjay Pant. “A non-parametric k-nearest neighbour entropy estimator”. In: *Physical Review E* 93.1 (Jan. 21, 2016), p. 013310. ISSN: 2470-0045, 2470-0053. DOI: 10.1103/PhysRevE.93.013310. arXiv: 1506.06501[cs,math]. URL: <http://arxiv.org/abs/1506.06501> (visited on 06/23/2023).
- [70] Jiantao Jiao, Weihao Gao, and Yanjun Han. *The Nearest Neighbor Information Estimator is Adaptively Near Minimax Rate-Optimal*. Sept. 12, 2018. DOI: 10.48550/arXiv.1711.08824. arXiv: 1711.08824[cs,math,stat]. URL: <http://arxiv.org/abs/1711.08824> (visited on 03/22/2023).
- [71] Kristina Monakhova et al. “Dancing under the stars: video denoising in starlight”. In: *2022 IEEE/CVF Conference on Computer Vision and Pattern Recognition (CVPR)*. 2022 IEEE/CVF Conference on Computer Vision and Pattern Recognition (CVPR). New Orleans, LA, USA: IEEE, June 2022, pp. 16220–16230. ISBN: 978-1-66546-946-3. DOI: 10.1109/CVPR52688.2022.01576. URL: <https://ieeexplore.ieee.org/document/9879972/> (visited on 01/27/2024).
- [72] Alexander Krull, Tomas Vicar, and Florian Jug. “Probabilistic Noise2Void: Unsupervised Content-Aware Denoising”. In: 2 (February 2019), pp. 1–9. DOI: 10.3389/fcomp.2020.00005. arXiv: 1906.00651. URL: <http://arxiv.org/abs/1906.00651>.
- [73] Ashish Vaswani et al. “Attention Is All You Need”. In: (Nips 2017). ISBN: 9781577357384. ISSN: 0140-525X. DOI: 10.1017/S0140525X16001837. arXiv: 1706.03762. URL: <http://arxiv.org/abs/1706.03762>.
- [74] Ivan Kobyzev, Simon J. D. Prince, and Marcus A. Brubaker. “Normalizing Flows: An Introduction and Review of Current Methods”. In: *IEEE Transactions on Pattern Analysis and Machine Intelligence* 43.11 (Nov. 1, 2021), pp. 3964–3979. ISSN: 0162-8828, 2160-9292, 1939-3539. DOI: 10.1109/TPAMI.2020.2992934. arXiv: 1908.09257[cs,stat]. URL: <http://arxiv.org/abs/1908.09257> (visited on 12/06/2023).
- [75] Jascha Sohl-Dickstein et al. *Deep Unsupervised Learning using Nonequilibrium Thermodynamics*. Nov. 18, 2015. arXiv: 1503.03585[cond-mat,q-bio,stat]. URL: <http://arxiv.org/abs/1503.03585> (visited on 12/06/2023).
- [76] Yang Song and Diederik P. Kingma. “How to Train Your Energy-Based Models”. In: (2021), pp. 1–22. arXiv: 2101.03288. URL: <http://arxiv.org/abs/2101.03288>.
- [77] Lucas Theis, Aäron van den Oord, and Matthias Bethge. *A note on the evaluation of generative models*. Apr. 24, 2016. DOI: 10.48550/arXiv.1511.01844. arXiv: 1511.01844[cs,stat]. URL: <http://arxiv.org/abs/1511.01844> (visited on 10/12/2023).
- [78] Diederik P Kingma et al. “Variational Diffusion Models”. In: ().
- [79] Matthew D. Hoffman et al. “Stochastic variational inference”. In: *Journal of Machine Learning Research* 14.2 (2013), pp. 1303–1347. ISSN: 15324435. arXiv: 1206.7051.
- [80] Christopher M. Bishop. “Mixture Density Networks”. In: (1994).

- [81] Kurt Hornik, Maxwell Stinchcombe, and Halbert White. “Multilayer feedforward networks are universal approximators”. In: *Neural Networks* 2.5 (Jan. 1989), pp. 359–366. ISSN: 08936080. DOI: 10.1016/0893-6080(89)90020-8. URL: <https://linkinghub.elsevier.com/retrieve/pii/0893608089900208>.
- [82] Yann LeCun et al. “Gradient-based learning applied to document recognition”. In: *Proceedings of the IEEE* 86.11 (1998), pp. 2278–2323. ISSN: 00189219. DOI: 10.1109/5.726791.
- [83] Dongning Guo. “The Interplay Between Information and Estimation Measures”. In: *Foundations and Trends® in Signal Processing* 6.4 (2013), pp. 243–429. ISSN: 1932-8346, 1932-8354. DOI: 10.1561/20000000018. URL: <http://nowpublishers.com/articles/foundations-and-trends-in-signal-processing/SIG-018> (visited on 10/27/2022).
- [84] Sri Rama Prasanna Pavani and Rafael Piestun. “High-efficiency rotating point spread functions”. In: *Optics Express* 16.5 (Mar. 3, 2008), p. 3484. ISSN: 1094-4087. DOI: 10.1364/OE.16.003484. URL: <https://opg.optica.org/abstract.cfm?URI=oe-16-5-3484>.
- [85] Jerry Chao, E. Sally Ward, and Raimund J. Ober. “Fisher information theory for parameter estimation in single molecule microscopy: tutorial”. In: *JOSA A* 33.7 (July 1, 2016). Publisher: Optica Publishing Group, B36–B57. ISSN: 1520-8532. DOI: 10.1364/JOSAA.33.000B36. URL: <https://opg.optica.org/josaa/abstract.cfm?uri=josaa-33-7-B36> (visited on 06/23/2023).
- [86] E.J. Candes and M.B. Wakin. “An Introduction To Compressive Sampling”. In: *IEEE Signal Processing Magazine* 25.2 (2008), pp. 21–30. ISSN: 1053-5888. DOI: 10.1109/MSP.2007.914731. arXiv: 1307.1360v1.
- [87] Sri Rama Prasanna Pavani and Rafael Piestun. “Three dimensional tracking of fluorescent microparticles using a photon-limited double-helix response system”. In: *Optics Express* 16.26 (Dec. 22, 2008). Publisher: Optica Publishing Group, pp. 22048–22057. ISSN: 1094-4087. DOI: 10.1364/OE.16.022048. URL: <https://opg.optica.org/oe/abstract.cfm?uri=oe-16-26-22048> (visited on 06/15/2023).
- [88] Yoav Shechtman et al. “Optimal point spread function design for 3D imaging”. In: *Physical Review Letters* 113.3 (Sept. 26, 2014). Publisher: American Physical Society. ISSN: 10797114. DOI: 10.1103/PhysRevLett.113.133902.
- [89] Ginni Grover, Sri Rama Prasanna Pavani, and Rafael Piestun. “Performance limits on three-dimensional particle localization in photon-limited microscopy”. In: *Optics Letters* 35.19 (Oct. 1, 2010), p. 3306. ISSN: 0146-9592. DOI: 10.1364/OL.35.003306. URL: <https://opg.optica.org/abstract.cfm?URI=ol-35-19-3306>.
- [90] Sean Quirin, Sri Rama Prasanna Pavani, and Rafael Piestun. “Optimal 3D single-molecule localization for superresolution microscopy with aberrations and engineered point spread functions”. In: *Proceedings of the National Academy of Sciences* 109.3 (Jan. 17, 2012), pp. 675–679. ISSN: 0027-8424. DOI: 10.1073/pnas.1109011108. URL: <https://pnas.org/doi/full/10.1073/pnas.1109011108>.

- [91] Elias Nehme et al. “DeepSTORM3D: dense 3D localization microscopy and PSF design by deep learning”. In: *Nature Methods* 17.7 (July 2020). Number: 7 Publisher: Nature Publishing Group, pp. 734–740. ISSN: 1548-7105. DOI: 10.1038/s41592-020-0853-5. URL: <https://www.nature.com/articles/s41592-020-0853-5> (visited on 09/02/2022).
- [92] Dorian Bouchet et al. “Fundamental Bounds on the Precision of Classical Phase Microscopes”. In: *Physical Review Applied* 15.2 (Feb. 19, 2021), p. 024047. ISSN: 2331-7019. DOI: 10.1103/PhysRevApplied.15.024047. URL: <https://link.aps.org/doi/10.1103/PhysRevApplied.15.024047> (visited on 09/02/2022).
- [93] David J. Lee, Michael C. Roggemann, and Byron M. Welsh. “Cramér–Rao analysis of phase-diverse wave-front sensing”. In: *Journal of the Optical Society of America A* 16.5 (May 1, 1999), p. 1005. ISSN: 1084-7529, 1520-8532. DOI: 10.1364/JOSAA.16.001005. URL: <https://opg.optica.org/abstract.cfm?URI=josaa-16-5-1005> (visited on 02/04/2024).
- [94] Jonathan Dong et al. “Fundamental bounds on the precision of iSCAT, COBRI and dark-field microscopy for 3D localization and mass photometry”. In: *Journal of Physics D: Applied Physics* 54.39 (Sept. 30, 2021), p. 394002. ISSN: 0022-3727, 1361-6463. DOI: 10.1088/1361-6463/ac0f22. URL: <https://iopscience.iop.org/article/10.1088/1361-6463/ac0f22> (visited on 02/04/2024).
- [95] Zhou Wang and A.C. Bovik. “Mean squared error: Love it or leave it? A new look at Signal Fidelity Measures”. In: *IEEE Signal Processing Magazine* 26.1 (Jan. 2009), pp. 98–117. ISSN: 1053-5888. DOI: 10.1109/MSP.2008.930649. URL: <http://ieeexplore.ieee.org/document/4775883/> (visited on 07/23/2023).
- [96] Richard D. Gill and Boris Y. Levit. “Applications of the van Trees Inequality: A Bayesian Cramér-Rao Bound”. In: *Bernoulli* 1.1 (Mar. 1995), p. 59. ISSN: 13507265. DOI: 10.2307/3318681. URL: <https://www.jstor.org/stable/3318681?origin=crossref> (visited on 07/24/2023).
- [97] Efe Aras et al. *A Family of Bayesian Cramer-Rao Bounds, and Consequences for Log-Concave Priors*. Feb. 22, 2019. arXiv: 1902.08582[cs, math]. URL: <http://arxiv.org/abs/1902.08582> (visited on 11/08/2022).
- [98] Trevor Hastie, Robert Tibshirani, and Jerome Friedman. *The Elements of Statistical Learning*. Springer Series in Statistics. New York, NY: Springer New York, 2009. ISBN: 978-0-387-84858-7. DOI: 10.1007/978-0-387-84858-7. URL: <http://link.springer.com/10.1007/978-0-387-84858-7> (visited on 02/04/2024).
- [99] W. James and Charles Stein. “Estimation with Quadratic Loss”. In: *Breakthroughs in Statistics*. Ed. by Samuel Kotz and Norman L. Johnson. Series Title: Springer Series in Statistics. New York, NY: Springer New York, 1992, pp. 443–460. ISBN: 978-0-387-94037-3. DOI: 10.1007/978-1-4612-0919-5\_30. URL: [http://link.springer.com/10.1007/978-1-4612-0919-5\\_30](http://link.springer.com/10.1007/978-1-4612-0919-5_30) (visited on 07/23/2023).
- [100] Harry L. Van Trees. *Detection, estimation, and modulation theory*. New York: Wiley, 2001. 1 p. ISBN: 978-0-471-09517-0.

- [101] Z. Wang et al. “Image Quality Assessment: From Error Visibility to Structural Similarity”. In: *IEEE Transactions on Image Processing* 13.4 (Apr. 2004), pp. 600–612. ISSN: 1057-7149. DOI: 10.1109/TIP.2003.819861. URL: <http://ieeexplore.ieee.org/document/1284395/> (visited on 07/25/2023).
- [102] Richard Zhang et al. *The Unreasonable Effectiveness of Deep Features as a Perceptual Metric*. Apr. 10, 2018. arXiv: 1801.03924[cs]. URL: <http://arxiv.org/abs/1801.03924> (visited on 07/25/2023).
- [103] S Yu Efroimovich. “Information contained in a sequence of observations”. In: *Problems in Information Transmission* 15 (1980), pp. 24–39.
- [104] Kuan-Yun Lee. “New information inequalities with applications to statistics”. PhD thesis. University of California, Berkeley, 2022.
- [105] D. Guo, S. Shamai, and S. Verdú. “Mutual Information and Minimum Mean-Square Error in Gaussian Channels”. In: *IEEE Transactions on Information Theory* 51.4 (Apr. 2005), pp. 1261–1282. ISSN: 0018-9448. DOI: 10.1109/TIT.2005.844072. URL: <http://ieeexplore.ieee.org/document/1412024/> (visited on 09/04/2022).
- [106] Emmanuel J. Candès and Mark A. Davenport. *How well can we estimate a sparse vector?* Mar. 1, 2013. arXiv: 1104.5246[cs,math,stat]. URL: <http://arxiv.org/abs/1104.5246> (visited on 07/13/2023).
- [107] Ashish Bora et al. *Compressed Sensing using Generative Models*. Mar. 9, 2017. arXiv: 1703.03208[cs,math,stat]. URL: <http://arxiv.org/abs/1703.03208> (visited on 07/03/2023).
- [108] Xiaohan Wei, Zhuoran Yang, and Zhaoran Wang. “On the statistical rate of nonlinear recovery in generative models with heavy-tailed data”. In: ().
- [109] Dustin G. Mixon and Soledad Villar. *SUNLayer: Stable denoising with generative networks*. Mar. 25, 2018. arXiv: 1803.09319[cs,stat]. URL: <http://arxiv.org/abs/1803.09319> (visited on 07/19/2023).
- [110] Yihong Wu and Sergio Verdú. “Rényi Information Dimension: Fundamental Limits of Almost Lossless Analog Compression”. In: *IEEE Transactions on Information Theory* 56.8 (Aug. 2010), pp. 3721–3748. ISSN: 0018-9448, 1557-9654. DOI: 10.1109/TIT.2010.2050803. URL: <http://ieeexplore.ieee.org/document/5508633/> (visited on 03/23/2023).
- [111] Richard G. Baraniuk et al. *Model-Based Compressive Sensing*. Dec. 9, 2009. DOI: 10.1109/TIT.2010.2040894. arXiv: 0808.3572[cs,math]. URL: <http://arxiv.org/abs/0808.3572> (visited on 07/04/2023).
- [112] Martin J. Wainwright. *Information-theoretic limits on sparsity recovery in the high-dimensional and noisy setting*. Feb. 20, 2007. arXiv: math/0702301. URL: <http://arxiv.org/abs/math/0702301> (visited on 07/04/2023).
- [113] David L. Donoho, Adel Javanmard, and Andrea Montanari. *Information-Theoretically Optimal Compressed Sensing via Spatial Coupling and Approximate Message Passing*. Jan. 18, 2013. arXiv: 1112.0708[cond-mat,stat]. URL: <http://arxiv.org/abs/1112.0708> (visited on 03/22/2023).

- [114] Galen Reeves and Michael Gastpar. *The Sampling Rate-Distortion Tradeoff for Sparsity Pattern Recovery in Compressed Sensing*. June 25, 2012. arXiv: 1006.3128[cs, math]. URL: <http://arxiv.org/abs/1006.3128> (visited on 07/14/2023).
- [115] Galen Reeves and Michael Gastpar. *Approximate Sparsity Pattern Recovery: Information-Theoretic Lower Bounds*. Feb. 4, 2013. arXiv: 1002.4458[cs, math]. URL: <http://arxiv.org/abs/1002.4458> (visited on 07/14/2023).
- [116] Jian Zhang and Bernard Ghanem. *ISTA-Net: Interpretable Optimization-Inspired Deep Network for Image Compressive Sensing*. June 18, 2018. arXiv: 1706.07929[cs]. URL: <http://arxiv.org/abs/1706.07929> (visited on 03/25/2024).